

DISSERTATION

MECHANISM-ENABLED POPULATION BALANCES

AND

THE EFFECTS OF ANISOTROPIES IN THE COMPLEX GINZBURG-LANDAU EQUATION

Submitted by

Derek Handwerk

Department of Mathematics

In partial fulfillment of the requirements

For the Degree of Doctor of Philosophy

Colorado State University

Fort Collins, Colorado

Fall 2019

Doctoral Committee:

Advisor: Patrick Shipman

Gerhard Dangelmayr

Iuliana Oprea

Richard Finke

Copyright by Derek Handwerk 2019

All Rights Reserved

ABSTRACT

MECHANISM-ENABLED POPULATION BALANCES

AND

THE EFFECTS OF ANISOTROPIES IN THE COMPLEX GINZBURG-LANDAU EQUATION

This paper considers two problems. The first is a chemical modeling problem which makes use of ordinary differential equations to discover a minimum mechanism capable of matching experimental data in various metal nanoparticle nucleation and growth systems. This research has led to the concept of mechanism-enabled population balance modeling (ME-PBM). This is defined as the use of experimentally established nucleation mechanisms of particle formation to create more rigorous population balance models. ME-PBM achieves the goal of connecting reliable experimental mechanisms with the understanding and control of particle-size distributions. The ME-PBM approach uncovered a new and important 3-step mechanism that provides the best fits to experimentally measured particle-size distributions (PSDs). The three steps of this mechanism are slow, continuous nucleation and two surface growth steps. The importance of the two growth steps is that large particles are allowed to grow more slowly than small particles. This finding of large grow more slowly than small is a paradigm-shift away from the notion of needing nucleation to stop, such as in LaMer burst nucleation, in order to achieve narrow PSDs.

The second is a study of the effects of anisotropy on the dynamics of spatially extended systems through the use of the anisotropic Ginzburg-Landau equation (ACGLE) and its associated phase diffusion equations. The anisotropy leads to different types of solutions not seen in the isotropic equation, due to the ability of waves to simultaneously be stable and unstable, including transient spiral defects together with phase chaotic ripples. We create a phase diagram for initial conditions representing both the longwave $k = 0$ case, and for wavevectors near the circle $|k| = \mu$ using the average L^2 energy.

ACKNOWLEDGEMENTS

I would like to thank my parents for their unending support and encouragement, without whom I would not exist. I would like to thank those teachers and mentors who believed in me, namely James Keener, Lance Miller, and Renzo Cavalieri, without whom I would not have attended graduate school. I would like to thank my committee member and collaborator Rick Finke for his enthusiasm for science, without whom this work would not exist. I would like to thank my fellow graduate students Sophie Bragdon, Catalina Camacho, Abby Duncan, Jessica Gehrtz, Karleigh Pine, Sam Pine, Ben Sencindiver, and many others for their help throughout graduate school and their continued friendship, without whom graduate school would have been a lonely place. I would like to thank my advisor Patrick Shipman whose exuberance for math is both intoxicating and contagious, without whom the toils of becoming a doctor would have surely been much less enjoyable. I would like to thank the rest of my committee for their insights and problems on which to work. Finally, I would like to thank my wife Alyssa for her love. I would not have succeeded without her.

DEDICATION

Dedicated to my granddad.

TABLE OF CONTENTS

ABSTRACT	ii
ACKNOWLEDGEMENTS	iii
DEDICATION	iv
LIST OF TABLES	vii
LIST OF FIGURES	viii
Chapter 1	Mechanism-Enabled Population Balance Modeling 1
1.1	Chemical Background and Motivation 1
1.1.1	Classical Nucleation Theory (CNT) and LaMer Burst Nucleation 3
1.1.2	Continuous Nucleation and the Finke-Watsky Mechanism 4
1.2	Population Balance Modeling Background 5
1.2.1	Solution Methods for the PBE 11
1.3	Mechanism-Enabled Population Balance Modeling 11
1.4	Mechanisms, Model Derivations, and Simulations 13
1.4.1	Two-Step Mechanism 15
1.4.2	Four-Step Mechanism 25
1.4.3	Three-Step Mechanism 36
1.4.4	Two-Step Alternative Termolecular Nucleation 39
1.4.5	Four-Step Alternative Termolecular Nucleation 42
1.4.6	Three-Step Alternative Termolecular Nucleation 47
1.4.7	Five-Step Mechanism 58
1.5	Comparison of Results 58
1.6	Comparison of Growth and Nucleation Rates 59
1.7	Open Flow Reactor Simulations 60
1.8	Extension to Larger Systems via Binning 62
1.9	On the Growth Kernel 65
1.10	Experimental Methods 68
1.10.1	The Pattern Search Algorithm 69
1.10.2	The Objective Function for Pattern Search 70
1.11	Summary and Conclusions 72
Chapter 2	Anisotropies in Spatially Extended Systems 76
2.1	Background and Introduction 76
2.1.1	Methods 79
2.1.2	The Complex Ginzburg-Landau Equation (Isotropic) 86
2.2	Anisotropic Complex Ginzburg-Landau 96
2.2.1	Linear Stability Analysis 98
2.2.2	Weakly Nonlinear Analysis for long-wave instability 102
2.2.3	ACGLE Phase Diagram 109
2.3	Summary and Conclusions 119

Bibliography 122

LIST OF TABLES

1.1	Particle size vs. diameter	33
1.2	Nucleation and growth on-off table	74
1.3	Mechanism rates and BFVs	75

LIST OF FIGURES

1.1	TEM histogram data time series	2
1.2	Burst nucleation	4
1.3	Number of particles showing continuous nucleation	5
1.4	TEM images of iridium(0) clusters from [71]	9
1.5	Cartoon illustration of nucleation, growth, and agglomeration	12
1.6	Plot of conversion between number of atoms and diameter	13
1.7	Cartoon illustration of particle interaction step interpretation	17
1.8	Two-step first-order nucleation fit to CHCRR	19
1.9	Two-step second-order nucleation fit to CHCRR	20
1.10	Two-step third-order nucleation fit to CHCRR	21
1.11	Two-step fourth-order nucleation fit to CHCRR	22
1.12	Two-step third-order nucleation fit to histogram	24
1.13	Four-step third-order nucleation fit to CHCRR	33
1.14	Four-step third-order nucleation fit to histogram	34
1.15	A second four-step third-order nucleation fit to CHCRR	35
1.16	Three-step third-order nucleation fit to CHCRR	40
1.17	Three-step third-order nucleation fit to histogram	41
1.18	Two-step alternative nucleation fit to CHCRR	43
1.19	Two-step alternative nucleation fit to histogram	44
1.20	Four-step alternative nucleation fit to CHCRR	48
1.21	Four-step alternative nucleation fit to histogram	49
1.22	Three-step alternative nucleation fit to CHCRR	51
1.23	Three-step alternative nucleation fit to histogram	52
1.24	Three-step alternative nucleation fit to histogram with complete polling	53
1.25	Three-step alternative nucleation fit to K_{diss} with complete polling	55
1.26	3_β -step fit to histogram with complete polling	56
1.27	3_β -step fit to histogram with complete polling	57
1.28	Comparison of final histograms and CHCRR curves for various tested mechanism CHCRR fits	59
1.29	Comparison of final histograms and CHCRR curves for various tested mechanism his- togram fits	60
1.30	Nucleation and growth rate for the 3-step mechanism	61
1.31	Open flow reactor simulation	62
1.32	Method of domain binning	66
1.33	Growth kernels	67
1.34	MATLAB histfit curve on TEM data.	69
1.35	Standard vs. complete polling	70
1.36	Pattern search polling and search process	71
2.1	Basic stripe, square, and hexagon patterns	77
2.2	Sand ripples	78

2.3	Linear growth rate classification from [13]	81
2.4	Examples of linear instability types	82
2.5	Transcritical bifurcation	83
2.6	Amplitude modulation	84
2.7	CGLE phase diagram from Chaté and Manneville	89
2.8	Example solutions of the CGLE	94
2.9	Magnitude and phase of a hole and shock-wall solution to CGLE	95
2.10	Phase and defect solutions to the CGLE	95
2.11	Transient vortex glass like solution to CGLE	96
2.12	Phase and defect solutions to the ACGLE	97
2.13	Hole and shock-wall solution comparison between CGLE and ACGLE.	98
2.14	Traveling waves	99
2.15	ACGLE linear stability region	102
2.16	Comparison of ACGLE and Phase Equation	105
2.17	Comparison of ACGLE and Phase Equation	105
2.18	Rost and Krug phase ripples	107
2.19	Rost and Krug cancellation modes	107
2.20	(α_2, β) parameter space for stability in the y -direction in the codimension-one bifurcation.	108
2.21	Dispersion relations of Equation (2.57) for fixed $\alpha_2 = \mu = 1$ and varying β with $\kappa = -1$ for codimension-one phase equation.	108
2.22	Codimension two phase equation solution examples	110
2.23	Comparison of ACGLE and Codimension Two Phase Equation	110
2.24	Noise-around-one A average energy	113
2.25	Noise-around one ∇A average energy	114
2.26	Noise-around-one A average energy	115
2.27	Noise-around one ∇A average energy	116
2.28	Noise-around-one $\beta = 1.1$ slice	117
2.29	Noise-around-zero $\beta = 0.6$ slice.	118
2.30	Time series of anisotropic spiral defects to phase chaos transition	119
2.31	Stability boundary verification for noise-around-one IC	120

Chapter 1

Mechanism-Enabled Population Balance Modeling

This chapter begins with background material and motivation for the problem of determining a minimal chemical mechanism to model the nucleation and growth of iridium nanoparticles. The current ideology and approaches are given. The concept of mechanism-enabled population balance modeling (ME-PBM) is introduced and used to test a dozen potential mechanisms. The mechanisms are fit to cyclohexene hydrogenation catalytic reporter reaction (CHCRR) kinetic data and to transmission electron microscopy (TEM) size histograms. The winning mechanism is a newly discovered 3-step mechanism which accurately recreates experimental PSDs with continuous nucleation. Some applications and an extension to the model are given.

A majority of the work in this chapter comes directly from the published paper [24] and the soon to be submitted paper [25]. This work was supported at Colorado State University revised by the U.S. Department of Energy (DOE), Office of Science, Office of Basic Energy Sciences, Division of Chemical Sciences, Geosciences & Biosciences, Catalysis Program, via DOE grant SE-FG402-02ER15453 under PI Richard Finke.

1.1 Chemical Background and Motivation

The process under which iridium nanoparticles increase in size remains unclear. Classically, nucleation and growth have been used to describe nanoparticle formation. Nucleation is the process by which a given number of small precursor molecules bind together to form a nucleus. This nucleus then acts as a seed for growth, whereby it attracts other precursor molecules and increases in size.

To date nucleation has usually been handled by classical nucleation theory (CNT). LaMer [35] extended CNT to the study of colloids where it is coupled with either coalescence of particles or Ostwald ripening for the growth step. This has been seen as the standard model for nucleation and growth of colloids for over 60 years. However, classical LaMer theory fails to capture both

the induction period and sigmoidal decrease of precursor, as well as the particle-size distributions [51,66,73].

Knowledge of nucleation and growth mechanisms is desirable since the physical properties and applications of particles typically depend strongly on their sizes. The evolving time series of particle-size distributions (PSDs) are difficult to obtain experimentally, but contain all of the kinetic information about how the particles are formed. As such, having a time series of PSDs for a given system is critical to test the validity of any proposed model of that system. Figure 1.1 shows a time series for a well-studied, prototype $\text{Ir}(0)_n$ nanoparticle formation system [41,42,71]. These evolving measurements of particle sizes allow us to test various mechanisms via what we will call mechanism-enabled population balance modeling (ME-PBM). Mechanism here means a collection of pseudoelementary steps, such as continuous nucleation ($A \rightarrow B$), autocatalytic growth ($A + B \rightarrow 2B$), or agglomeration ($B + B \rightarrow C$). Our objective is to test as many mechanisms as possible in a disproof-based manner to obtain a minimal mechanism capable of reproducing the experimental PSDs.

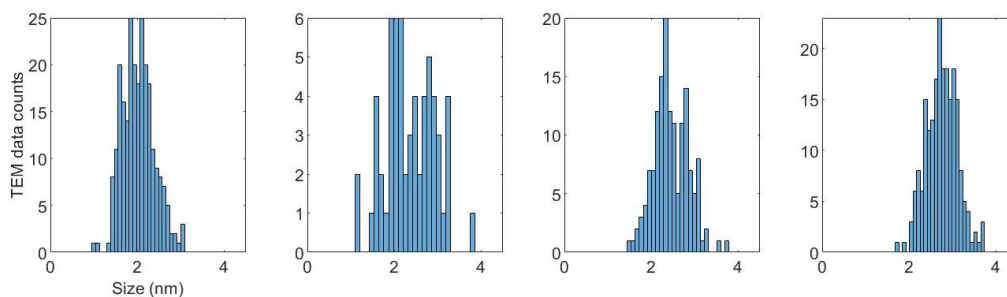


Figure 1.1: Time series of histogram particle counts from TEM images at times 0.918, 1.170, 2.336, and 4.838 hours. Finding a minimal mechanism that recreates this experimental data is our goal.

Historically, cyclohexene hydrogenation catalytic reporter reaction (CHCRR) kinetic data has been used to fit and test the validity of proposed mechanisms. This reporter reaction follows the kinetics of nanoparticle formation in real-time, albeit indirectly. The reporter reaction method relies on there being an excess of cyclohexene and H_2 compared to precursor and on the cyclohexene hydrogenation rate being fast compared to that of nucleation and growth. Usually only the first half

or less of the CHCRR curve is used for fits since the initial zero-order dependence on cyclohexene breaks down as particle formation continues.

In addition to fitting to the TEM data, we also fit to this CHCRR data. This involves fitting the actual precursor concentration from simulations to the entire measured CHCRR data. This is perhaps not ideal, since it is not known exactly where the CHCRR curve becomes separated from precursor concentration, but it is reasonable given the available data. The breakdown in CHCRR accuracy as particle formation proceeds should be remembered when comparing simulated precursor time-series concentrations to the measured CHCRR values. Some amount of precursor should remain when cyclohexene is depleted, and the results from our histogram fits may predict the deviation of the precursor from reporter reaction in the second half of the reaction.

1.1.1 Classical Nucleation Theory (CNT) and LaMer Burst Nucleation

Nucleation is the foothold by which a phase transition proceeds. CNT gives a prediction for the rate of nucleation which is seen as the dominating process that determines the speed of the phase transition. The rate of nucleation as predicted by CNT is partially determined by the relationship between the interfacial free energy and the bulk free energy. For homogeneous nucleation, where the particle is assumed to be a sphere, the interfacial free energy is proportional to r^2 and the bulk free energy is proportional to r^3 . The difference of these two energies gives the free energy barrier which is used in the predicted rate of nucleation. For heterogeneous nucleation the particle is partially in contact with a surface which decreases the interfacial free energy and therefore the free energy barrier. This causes an increase in the rate of nucleation.

LaMer and Dinegar [35] applied CNT to the study of colloids to account for the formation of monodispersed hydrosols. Their idea is that there are three phases to nanoparticle formation: (I) a build-up of precursor; (II) nucleation; (III) growth by diffusion. First (I) the precursors accumulate until they become supersaturated. Once supersaturated they (II) rapidly nucleate which lowers the supersaturation which makes the rate of nucleation zero. The particles then (III) grow. Nucleation and growth are treated as separate, independent steps. Nucleation is rapid and transient.

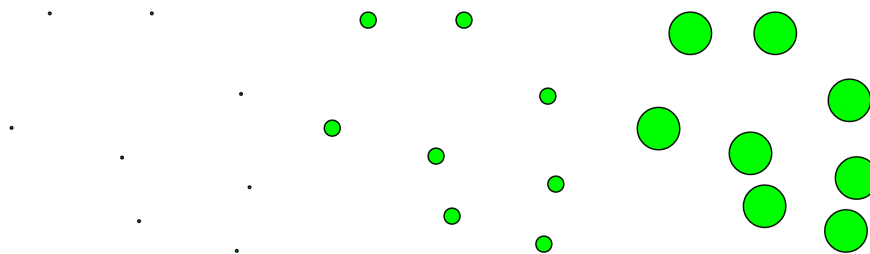


Figure 1.2: LaMer-type burst nucleation proposes a monodispersed population by having all particles nucleate essentially at once and then grow at the same rate.

Evidence for the lack of applicability of burst nucleation has been gathered in a review of the nearly 2000 citations of LaMer’s 1950s paper [73]. This paper found that only 10% (191 papers) of the citations have any in depth discussion of the LaMer model and a mere 3.3% (65 papers) claim that the model applies to their system. Remarkably, this review shows that the only time the differential equation corresponding to the LaMer model has been used to fit nucleation and growth kinetics data is in the original 1950 LaMer paper [73].

1.1.2 Continuous Nucleation and the Finke-Watzky Mechanism

The Finke-Watzky (FW) mechanism [71] was the first new mechanism for particle growth in over 45 years at the time of its publication. It consists of a slow, continuous nucleation step, and a fast, autocatalytic growth step. It is given by the pseudoelementary steps (see [21, 48] or chapter 6 of [46] for some classic pseudoelementary mechanisms)



where A denotes the precursor and B denotes all other size particles. The slow, continuous nucleation of the FW mechanism stands in stark contrast to the often cited work by LaMer of burst nucleation. It appears that the LaMer model of burst nucleation is incorrect [73] and the FW model of continuous nucleation offers an alternative route to nanoparticle formation. The 2-step mechanism in Mechanism (1.1) is able to follow the induction period and sigmoidal shape of a reporter reaction approximation of the precursor concentration, which the LaMer model cannot do. How-

ever, the FW 2-step model is not able to match the first few moments (mass, mean, variance, etc.) of the size distributions [50]. The FW mechanism gives better results than the LaMer model but its flaws means that it doesn't tell all of the story and needs to be either extended or improved. We present here a new 3-step mechanism based on the 2-step that includes slow, continuous nucleation that is able to qualitatively match experimentally collected TEM size distribution data, demonstrated in Figure 1.3.

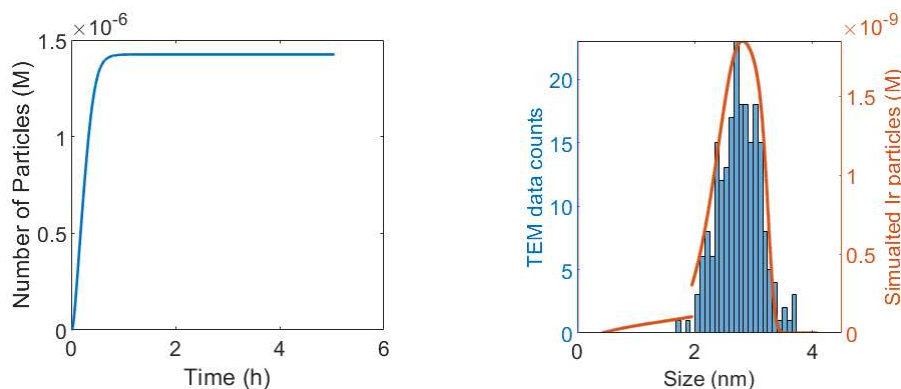


Figure 1.3: Total number of particles (left) and size distribution at 4.838 hours (right) produced by the new 3-step mechanism with alternative termolecular nucleation (1.30). The number of particles continues to increase throughout the simulation demonstrating that narrow, near-monodispersed size distributions are possible in spite of continuous nucleation. Here "particle" does not include monomers.

1.2 Population Balance Modeling Background

The population balance equation (PBE) [29, 52, 62] is the *de facto* way to model the nucleation and growth of particles. The equation has been in use for over 50 years and together with its various solution methods is capable of modeling and predicting growth processes across nature. It is used across engineering, biology, physics, chemistry and medicine to model such phenomena as crystal formation, nanoparticles, cell division and proliferation, aerosols, and chemotherapy [52, 54, 63]. It is useful whenever there is some conserved population and is sophisticated enough to handle multiple internal particle coordinates such as size, temperature, and volume as well as the external

coordinates of where particles are located spatially. The PBE is statistical and probabilistic using distributions, moments, and averages over bins.

The general form of the PBE is

$$\begin{cases} \partial_t f + \nabla_x \cdot \dot{\mathbf{X}} f + \nabla_r \cdot \dot{\mathbf{R}} f = h \\ f(\mathbf{x}, \mathbf{r}, 0) = N_0 g(\mathbf{r}) \delta(\mathbf{x} - \mathbf{x}_0), \end{cases} \quad (1.2)$$

with appropriate boundary conditions [52]. This formulation allows for the modeling of scenarios by means of the internal coordinates $\mathbf{x} \in \mathbb{R}^n$ and external coordinates $\mathbf{r} \in \mathbb{R}^3$ which together make up the particle state space (\mathbf{x}, \mathbf{r}) . The internal coordinates are any characteristic of the particles that need to be measured such as density, mass, volume, temperature, or size. The external coordinates give where a particle is in physical space. The continuous phase, *i.e.* what the particles are suspended in, may also be modeled via the continuous phase vector $\mathbf{Y}(\mathbf{r}, t)$. The dotted, capital letters $\dot{\mathbf{X}}(\mathbf{x}, \mathbf{r}, \mathbf{Y}, t)$ and $\dot{\mathbf{R}}(\mathbf{x}, \mathbf{r}, \mathbf{Y}, t)$ are, in typical dynamical systems notation, the velocities of the internal and external coordinates. Equation (1.2) can be derived via a conservation law, *aka* number balance, and Reynolds transport theorem to bring the derivative inside the integral [52].

In many instances the external coordinates \mathbf{r} and continuous phase vector \mathbf{Y} can be ignored simplifying the equation. For example, the spatially uniform PBE for nucleation and growth with particle volume as the only internal coordinate and no external coordinate dependence is given by

$$\frac{\partial n(\nu, t)}{\partial t} + \frac{\partial}{\partial \nu} [G(\nu, t)n(\nu, t)] = \dot{N}(t)\delta(\nu - \nu_c), \quad (1.3)$$

where $n(\nu, t)$ is the number of particles, $G(\nu, t)$ is the growth rate, $\dot{N}(t)$ is the nucleation rate, and ν_c is the assumed critical nucleus size. This is an advection equation with a point source term that represents nucleation and where the wave travels in the internal coordinate of number of particles instead of in physical space. In this set up, the precursor entities that undergo nucleation are not considered particles. Instead, the smallest particle is the critical, or effective, size given by ν_c .

We give a derivation of the one-dimensional PBE, a short history of the PBE, and an overview of methods to solve it.

Derivation of the Spatially Uniform PBE with One Internal Coordinate

The PBE (1.3) can be derived from the integral form of the balance law

$$\frac{d}{dt} \int_{\nu_1}^{\nu_2} n(\nu, t) d\nu = \phi(n(\nu_1, t)) - \phi(n(\nu_2, t)) + \int_{\nu_1}^{\nu_2} \sigma(\nu, t) d\nu, \quad (1.4)$$

which says that the change in time of the number of particles in the range of volumes $\nu_1 \leq \nu \leq \nu_2$ is equal to the incoming flux on the left boundary $\phi(n(\nu_1, t))$ plus the incoming flux on the right boundary $\phi(n(\nu_2, t))$ plus the total source over the region, $\int_{\nu_1}^{\nu_2} \sigma(\nu, t) d\nu$. Note that we will say positive flux is to the right and negative flux is to the left. So, both ϕ terms in Equation (1.4) are into the cell.

We can rewrite equation 1.4 using the fundamental theorem of calculus to get

$$\frac{d}{dt} \int_{\nu_1}^{\nu_2} n(\nu, t) d\nu = - \int_{\nu_1}^{\nu_2} \frac{\partial}{\partial \nu} \phi(n(\nu, t)) d\nu + \int_{\nu_1}^{\nu_2} \sigma(\nu, t) d\nu. \quad (1.5)$$

Now we can bring the time derivative inside the integral and move everything to one side to get

$$\int_{\nu_1}^{\nu_2} \left(\frac{\partial}{\partial t} n(\nu, t) + \frac{\partial}{\partial \nu} \phi(n(\nu, t)) - \sigma(\nu, t) \right) d\nu = 0. \quad (1.6)$$

The integral over an arbitrary region equals zero. Hence, the integrand must be equal to zero, which yields

$$\frac{\partial}{\partial t} n(\nu, t) + \frac{\partial}{\partial \nu} \phi(n(\nu, t)) - \sigma(\nu, t) = 0, \quad (1.7)$$

then

$$\frac{\partial}{\partial t} n(\nu, t) + \frac{\partial}{\partial \nu} \phi(n(\nu, t)) = \sigma(\nu, t). \quad (1.8)$$

Replacing the flux and sources terms with $\phi(\nu, t) = G(\nu, t)n(\nu, t)$ and $\sigma(\nu, t) = \dot{N}(t)\delta(\nu - \nu_c)$ yields Equation (1.3). The growth term can be set to depend on volume, surface area, or some

other measure. For example, if growth is proportional to volume, then

$$G(\nu, t) = k_2[A]\nu.$$

The rate of nucleation of order m can be given as

$$\dot{N}(t) = \frac{A_v \nu_{Ir}}{\nu_c} k_1 [A]^m$$

, where A_v is Avogadro's number ν_{Ir} is the volume of an iridium atom, and ν_c is the so-called critical volume. As noted in [50], this is also the time derivative of the first moment of n . It should be noted that some of the steps in the above derivation of Equation (1.8) require that the functions n and ϕ are smooth enough to allow bringing the derivative inside the integral [39].

History of the PBE

There are several excellent review articles on the population balances including Ramkrishna and Mahoney [53], Sporleder *et al.* [63], and Ramkrishna and Singh [54]. The latter has particularly nice tables on the applications of PBM and further review articles. Sporleder *et al.* [63] give a nice derivation of the population balance equation and mentions that while the equation gives more detailed results than macroscopic equations it operates above the kinetic level. The models in this paper are derived on the kinetic level.

In 1916 Smoluchowski, see [61] for the original German article, or [10] for a summary in English, created a discrete model for the pure agglomeration of particles whereby two particles would coalesce if they entered each other's sphere of influence. This system which can be modeled by the mechanism



is the origin and ancestor of the PBE. If the growth kernel between two particles in this system is defined as $\Gamma_{i,j}$ and the concentration of particles N_i of size i at time t is $n_i(t)$, then the law of mass action gives the system

$$\frac{dn_i}{dt} = \frac{1}{2} \sum_{j=1}^{i-1} \Gamma_{j,i-j} n_j n_{i-j} - \sum_{j=1}^{\infty} \Gamma_{i,j} n_i n_j. \quad (1.10)$$

The initial state for Equation (1.10) consists of a concentration of similarly sized precursor particles. These particles, more often than not, then proceed to agglomerate into a particle of infinite size, called a gel, in process called gelation. Essentially, for most aggregation kernels the system does not conserve mass. Instead, there is a flux out of the system into what is known as the gel. Forming a gel can be an unrealistic final state for nanoparticles in systems which stay polydispersed or near-monodispersed as seen in experiments. For an example where nanoparticles do not form one large particle (a gel) see Figure 1.4. Instead, they form a polydispersed (or near monodispersed) range of sizes. The nanoparticles in this figure remain separated from each other and do not form a bulk metal. The surface ligands are responsible for this separation.

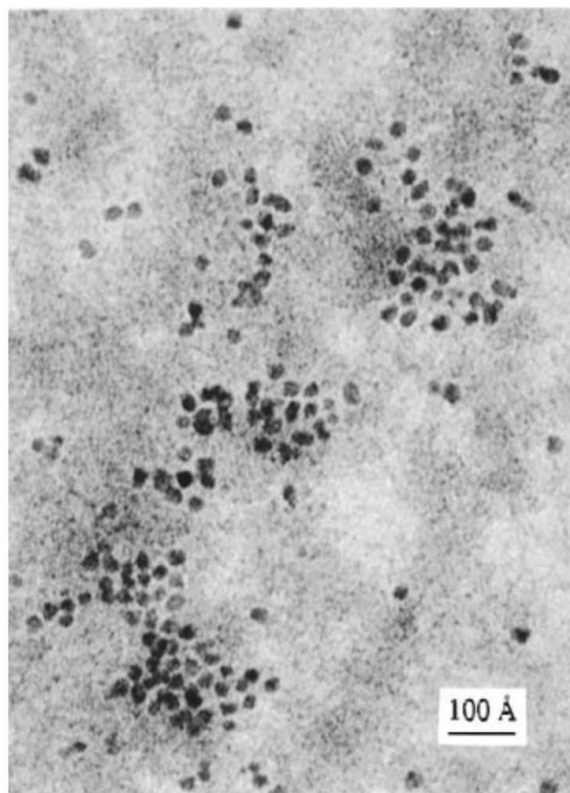


Figure 1.4: Transmission electron microscopy (TEM) image of near-monodispersed iridium(0) clusters from . Reprinted with permission from [71]. Copyright 1997 American Chemical Society.

For certain growth kernels (1.10) has exact solutions [70]. These kernels are the constant kernel $\Gamma_{i,j} = 1$, the additive kernel $\Gamma_{i,j} = (i + j)/2$, and the product kernel $\Gamma_{i,j} = ij$. For a more general kernel $\Gamma_{i,j} = \Gamma(i^\mu j^\nu + i^\nu j^\mu)$ considered in the large particle limit $i \rightarrow \infty$ or $j \rightarrow \infty$ gelation will occur whenever $\nu < 1 - \mu$.

A similar system to the Smoluchowski equations are the Becker-Döring equations from 1935 [3,4,70]. This system of equations come from the mechanism



where fragmentation is now allowed via the breakage kernel β . Note that unlike the Smoluchowski equation (1.9), the Becker-Döring equation (1.11) only involves monomer-particle interactions and not more general particle-particle interactions for which the sums are required in (1.10). Again using the law of mass action the governing system for (1.11) is

$$\frac{dn_i}{dt} = J_{i-1} - J_i \quad (1.12)$$

where the fluxes $J_i = \Gamma_i n_1 n_i - \beta_{i+1} n_{i+1}$ and $i \geq 2$ since n_1 is constant. The first flux term in (1.12) is then how much is gained from and lost to a particle one size smaller, and the second flux term is how much is lost and gained from growth to and breakage from a particle of one size larger.

In its original formulation (1.11) was modeled with a constant monomer concentration (*i.e.* an open system), but has also been modeled with constant mass (*i.e.* a closed system). The situation with constant mass is more complicated since each equation in System (1.12) becomes nonlinear in n_i . There are also versions of (1.9) and (1.11) that have more complicated, nonbinary fragmentation processes where a single breakage event can result in more than two daughter particles.

The continuous form of the Smoluchowski coagulation equation is called the general dynamic equation (GDE) and was initially used primarily by the atmospheric sciences to study topics such as aerosols and cloud formation. There is also a discrete version of the GDE [22]. In 1964 Hulburt and Katz [29], and Randolph [55] simultaneously extended the GDE to the PBE.

When the terms ODE or discrete are attached to population balance modeling they typically mean some sort of discretization of the PDE form of the PBE, such as in Bajcinca et al. [2] or Liao et al. [40]. The models presented in this paper will not follow this norm. They are derived at the discrete kinetic level and are wholly ordinary differential equations similar to (1.9) and (1.11), and not ODE approximations of a PDE.

1.2.1 Solution Methods for the PBE

The method of moments (MoM) is currently a popular solution scheme for doing population balance modeling due to its comparatively low computational cost compared to other methods. The paper by Falola *et al.* [20] gives an overview of different methods to solve population balance equations. These can be divided into direct methods and methods of moments. The method of moments works on the assumption that only the average information of the distribution is relevant. The MoM transforms the partial differential equation of the PBE into a series of ordinary differential equations for a select number of low-order moments. The information in these moments, such as number of particles, mean, *etc.*, is then used to estimate the actual particle property distribution. However, since only a few moments are used, the actual distribution cannot usually be computed. See [20] for an exception.

1.3 Mechanism-Enabled Population Balance Modeling

Instead of modeling what is a physically discrete process in a continuous manner using a PBE, and then discretizing the continuous problem to solve it, we can stay entirely in the discrete domain similar to the original Smoluchowski system. For many applications this is computationally infeasible, but is not for the formation of nanoparticles in the systems studied here. Iridium nanoparticles in particular have a maximum size of around 4 nm which is approximately only 2500 particles (see Figure 1.6). This leads to what is in some regards a large system of ODEs compared to say the Lotka-Volterra equations or an SIR model. However, a system of 2500 ODEs is easily solvable on current (circa 2019) laptop/desktop hardware and allows us to start and stay entirely

within the discrete domain without the need to resort to any continuous statistical, stochastic, or binning arguments. Once we derive the particle interactions from the mechanism we can write our ODE system for the individual particle sizes. This process can be related to using a bin size of one in the various discretization methods for the PBE. Which, again, is most often not possible in typical PBM applications due to the sheer number and sizes of interacting particles.

To determine how to model how the particles interact with each other we will use various elementary-step mechanisms. We will start with the simplest known mechanism [71] and add complexity or variety as needed with the goal of best matching the experimental size distribution data. This procedure of adding new steps and testing different versions of steps should hopefully result in a minimum mechanism to explain nanoparticle formation while simultaneously disproving other conjectured mechanisms. An increase in complexity from one mechanism to another may not be the smallest possible, for example going from our 2-step to 4-step mechanisms below. However, the general method of adding complexity and trying out the resulting, new mechanism has proven useful in that it lead to the discovery of our main result Mechanism 1.22.

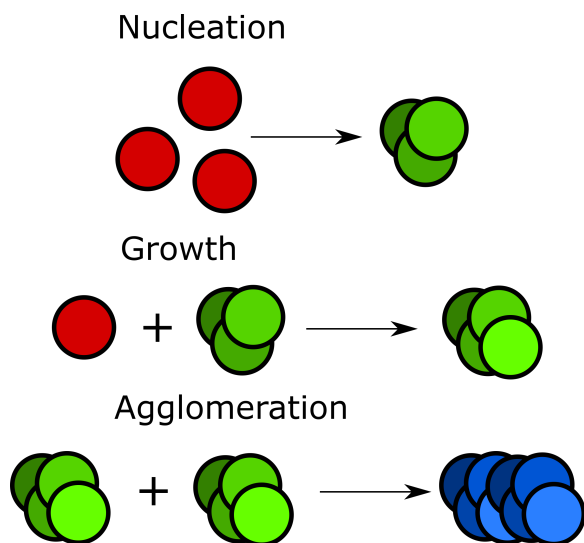


Figure 1.5: Illustration of particle interaction steps. $A \rightarrow B$, $A + B \rightarrow 2B$, and $B + B \rightarrow C$ are shown with A red, B green, and C blue.

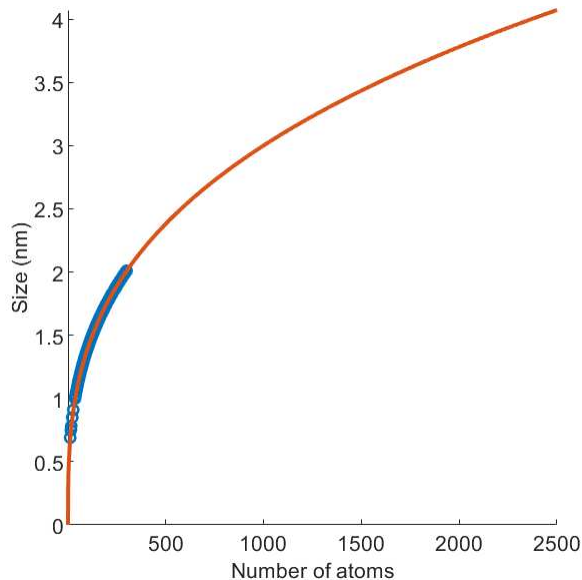


Figure 1.6: Conversion between number of atoms in a particle and diameter in nanometers. Blue circles are data. Red curve is $d(n) = 0.300082023n^{1/3}$.

The modeling done in some papers, for example [75], is mechanism-enabled, but does not include population balances. There are only a low number of species, say 3, to represent thousands of populations. The effects of such a reduction in equations benefits computation, but has a likely quite significant effect on results. The many papers in the chemical engineering literature on population balance modeling on the other hand are not mechanism-enabled. Two papers come close to the full ME-PBM approach [16, 18]. The models used [18] are similar to the standard 2-step, and the 2-step with full agglomeration using the Smolochowski equation. A critical point in this paper is that the rate constants for growth and agglomeration are constant and not at all size-dependent. In [16] they assume a standard aggregation kernel proportional $(r + R) \left(\frac{1}{r} + \frac{1}{R} \right)$ for spherical particles of radii r and R , but explicitly state and assume that this kernel is instead constant thereby missing any discovery of small particles growing at different rates than larger ones being beneficial.

1.4 Mechanisms, Model Derivations, and Simulations

To determine a minimal mechanism that accurately reproduces experimental size distributions of nanoparticles we start with the FW 2-step and then proceed to include additional steps to create

new mechanisms. These new mechanisms can then advise what the next will be, and so on. What the next more complicated mechanism is, or which next step to add is somewhat arbitrary and is influenced by instinct and experience. At times a step backwards in the simpler direction is needed after analyzing a more complicated mechanism. As will be discussed later, an explicit example of this is the formulation of the three-step mechanism from the four-step. This Ockham's razor based approach should then elucidate the simplest mechanism capable of modeling experiments.

The main mechanisms studied in this dissertation are the 2-step, 4-step, and new 3-step, each with and without alternative termolecular nucleation [49]. Evidence suggests that nucleation for the iridium system under consideration is 3rd order in Ir. This evidence and the reaction scheme for this alternative termolecular type of nucleation can be seen in [49]. The different levels of complexity between the mechanisms helped elucidate the key to reproducing suitable particle-size distributions. The key as it turns out is our main finding, which is that in order to get simulated particle-size distributions that fit the experimental size histograms *the larger particles must grow more slowly than the smaller particles*. This finding is reinforced through simulations of the various mechanisms. In [51] the author alludes to this conclusion but produces no evidence that this is the case other than verbal arguments. The paper talks about colloidal stability increasing with size, which therefore makes the "small" particles more reactive. However, a strictly surface area to volume ratio decrease in reactivity is not sufficient for a low polydispersity as seen by our simulations for the 2-step mechanism. Our simulations include a function, which we call r , that limits the reactive atoms to those on the surface. It is only when additional steps to make the "small" particles more reactive and the "large" particles less reactive do we see simulated PSDs that match experimental data with a low polydispersity. We also disagree with that paper's conclusions that nucleation models are irrelevant. We see from our simulations that having a more correct and accurate representation of nucleation improves the mechanistic fits. Furthermore, the important scientific question of whether nucleation is burst or continuous is far from irrelevant.

Simulations were carried out using MATLAB. Fits were performed using the fitting function `patternsearch` which allows for multivariate constrained fitting, unless otherwise noted. For a more detailed explanation of the methods used in the fitting process see §1.10.

1.4.1 Two-Step Mechanism

The first mechanism we will look at is the Finke-Watzky [71] 2-step. As mentioned above, this has a nucleation step and a growth step. The nucleation is slow and continuous and the growth is autocatalytic. The pseudoelementary steps for the mechanism are



Derivation of Two-Step ODE Model from the Mechanism

Before we start the derivation of the two-step, or any other, model we need to establish some notation. The following notation for particles of different sizes can be interpreted as either the concentration of a given size with dimensions of molarity $M = \text{mol/L}$ or as dimensionless numbers of atoms. Keep in mind that this will affect the dimensions of the rate constants. For our results and simulations the notation represents concentration, but here for the derivation it is easier to think of the different particle sizes just as numbers irrespective of moles or any volume.

Let the monomers in a particle of size $j \in \mathbb{N}$ be denoted by m_j with the precursor m_1 also called a . The particles comprised of j number of these monomers are denoted n_j . We have the relation $m_j = jn_j$, *i.e.* the number of monomers in particles of size j is equal to j times the number of particles. The relationship between the total number of monomers in a particle and the number that are available to bind is given by the relationship $b_j = r(j)m_j$, where b_j are the number of binding sites on a particle, and the function $r(j)$ can represent various effects such as volume or surface area dependent growth, or ligand capping. These b_j monomers are those which can actually interact with other monomers. For example, those that are on the surface of the particle and not on the interior. We will see later that the function $r(j)$ will make up part of the growth kernel $\Gamma(j)$.

Unlike the PBE, which has no direct particle-particle interactions, our model is based on atom-to-atom contact. As such, the monomers on the particle surface should be capable of binding while those on the inside remain unreactive. Therefore, a surface area model is adapted by choosing the function $r(j) = 2.677j^{.72}/j$. This is the number of surface monomers divided by the total number of monomers where the number of surface atoms is taken from Schmidt and Smirnov [57]. It should be remarked that the surface atom approximation given by Schmidt and Smirnov has more surface atoms than total atoms for particles smaller than n_{34} . Using this approximation verbatim makes the function r not directly correspond to a percentage of total atoms that are bindable, at least for small sizes. This has the effect of making smaller sized atoms more reactive than a strictly surface area dependent growth model. One could easily modify r to be piecewise with values 1 for n_j smaller than n_{34} and the Schmidt and Smirnov approximation for larger. The r function is defined as a way to modify the number or effectiveness of the binding sites, but it also essentially modifies the growth rates, as can be seen in System 1.17, and can serve not only to change between surface area or volume models, but can also be used for size-dependent growth rates or capping processes. Together with the rate constants k_1, k_2, \dots , it is the combined kernel Γ for all size-dependent process modifiers. The combination of all of these things into one function reduces the complexity of the model, but there must be careful consideration and interpretation of the chosen r and Γ , hopefully based on experimentally validated mechanisms.

Özkar and Finke [49] found nucleation to be third order for iridium, but we will use a generic nucleation order ω in our derivation. From Mechanism 1.13 we see that nucleation can be written in terms of the monomers as



Growth of the nucleus is modeled by $a + m_\omega \xrightarrow{k_2} 2m_{\omega+1} - (\omega - 1)m_\omega + (\omega - 1)m_{\omega+1}$ and in general, growth is $a + m_j \xrightarrow{k_2} 2m_{j+1} - (j - 1)m_j + (j - 1)m_{j+1}$ for a particle of size j . The left-hand side of these growth relationships indicate that a single monomer of precursor will interact with a single monomer that is part of a larger particle, as visualized in Figure 1.7. This is the primary reason for the adoption of surface area growth in this paper. Particle volume may affect growth through

energy or other means, but surely the assumption that internal atoms are not available to directly bind and interact with the precursor in this simplified atomistic viewpoint is sound. The right-hand side of the relationships are the results of the monomer-particle interaction. The first term represents the precursor monomer and the particle monomer becoming monomers of a particle of size one larger. The middle term is the loss of the rest of the original monomers, and the final term is the rest of the original monomers changing to the larger size. Combining terms, we have the logical result

$$a + jm_j \xrightarrow{k_2} (j+1)m_{j+1}, \quad (1.15)$$

which says that the addition of a precursor monomer to a particle with j monomer units will form a new particle with $j+1$ monomer units.

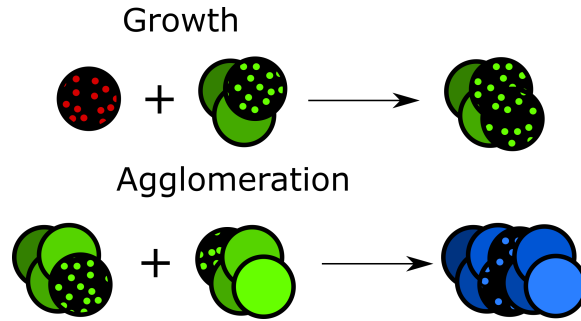


Figure 1.7: Illustration of interpretation of particle interaction steps for model derivation. The dotted atoms are those which are actually interacting. $A + B \rightarrow 2B$ has the red-dotted atom joining with the green-dotted which makes two green-dotted atoms. $B + B \rightarrow C$ has the two green-dotted atoms combining to make two blue-dotted C atoms. This coalescence also has the effect of changing the solid green atoms into solid blues.

Taking relations (1.14) and (1.15), and noting that the precursor a only attaches to binding sites, leads to the system

$$\begin{aligned} \frac{dm_1}{dt} &= -\omega k_1 m_1^\omega - k_2 m_1 \sum_{i=\omega}^{\infty} b_i \\ \frac{dm_\omega}{dt} &= \omega k_1 m_1^\omega - \omega k_2 m_1 b_\omega \\ \frac{dm_j}{dt} &= j k_2 m_1 (b_{j-1} - b_j), \quad \omega < j < \infty, \end{aligned} \quad (1.16)$$

for changes in monomers where $j \geq \omega + 1$. This system must now be converted into a system for the particles n_j using the $m_j = jn_j$ and $b_j = r(j)m_j$ substitutions described above. Using the substitutions we obtain

$$\begin{aligned}
\frac{dn_1}{dt} &= \underbrace{-\omega k_1 n_1^\omega}_{\text{loss from nucleation}} - \underbrace{k_2 n_1 \sum_{i=\omega}^{\infty} r(i) i n_i}_{\text{loss from growth}} \\
\frac{dn_\omega}{dt} &= \underbrace{k_1 n_1^\omega}_{\text{gain from nucleation}} - \underbrace{\omega k_2 n_1 r(\omega) n_\omega}_{\text{loss from growth}} \\
\frac{dn_j}{dt} &= \underbrace{k_2 n_1 ((j-1)r(j-1)n_{j-1} - jr(j)n_j)}_{\text{gain and loss from growth}}, \quad \omega < j < \infty
\end{aligned} \tag{1.17}$$

as our system for particle sizes. From here we can see that if the growth rate k_2 is taken to be a function of particle size, instead of a constant, that it would have to be distributed into the sum in the n_1 equation and the difference in the n_j equation. This would give the growth kernel $\Gamma(j) = k_2(j)r(j)$. We now have a model set of equations that has been *mechanistically-enabled* since our system of ODEs comes directly from Mechanism 1.13.

Simulations of the 2-step Model

An attempt to fit the fourth and final time TEM histogram using System (1.17) with third order nucleation $\omega = 3$ and `patternsearch` with lower bounds of `[0 0]` and upper bounds of `[Inf Inf]` resulted in values of $k_1 = 4.06^{31}$ and $k_2 = 0$. This made a BFV of approximately 226 which can now be thought of as a benchmark for the worst case scenario fit. The algorithm found that making the PSD at the final measured time identically zero almost everywhere lead to a smaller objective function value than any other possible PSD. The numerical approximation to infinity value of k_1 and the zero value of k_2 mean that the entire concentration of precursor instantly nucleates and never grows past the nucleus size. Succinctly, it didn't work.

Small strictly positive lower bounds and upper bounds were used in all following fits unless otherwise noted. The first of these can be seen in Figure 1.8 in which (1.17) with first-order nucleation was used to attempt to fit the CHCRR curve. As we can see from the figure, the resulting

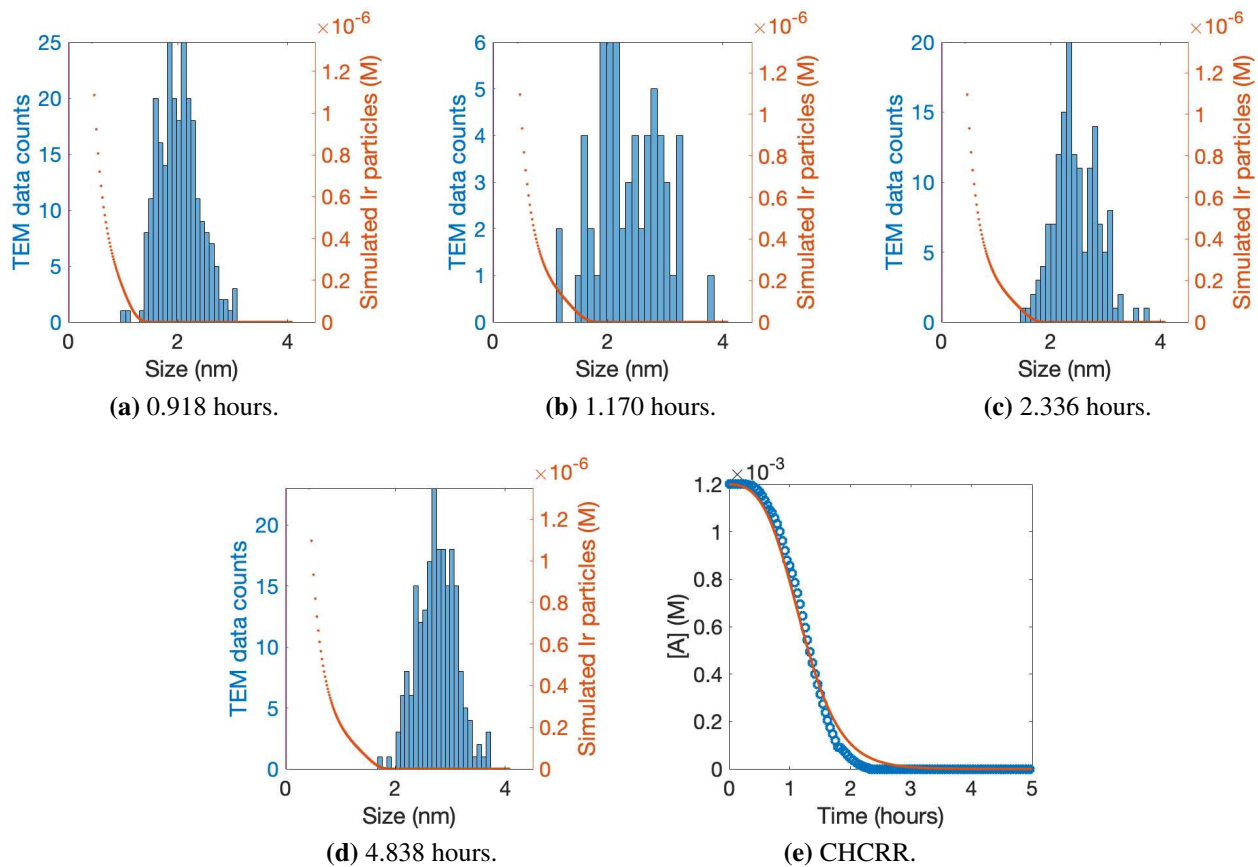


Figure 1.8: Fit to CHCRR curve using the classic FW 2-step mechanism and first-order nucleation. The rate constants produced by the fit are $k_1 = 6.70 \times 10^{-3} \text{hr}^{-1}$ and $k_2 = 2.52 \times 10^3 \text{M}^{-1} \text{hr}^{-1}$. These were used to produce the comparison of simulations (red dots) vs. the experimental TEM PSDs (blue histograms). The best function value (BFV) is 3.92×10^{-4} .

simulated CHCRR curve does a fair job of matching the experimental values. There is a slight overestimate in the lower, second elbow around the 2 hour mark. The simulated histograms in (a)-(d) show a strictly monotone decreasing PSD which is nowhere near a match to the TEM histograms.

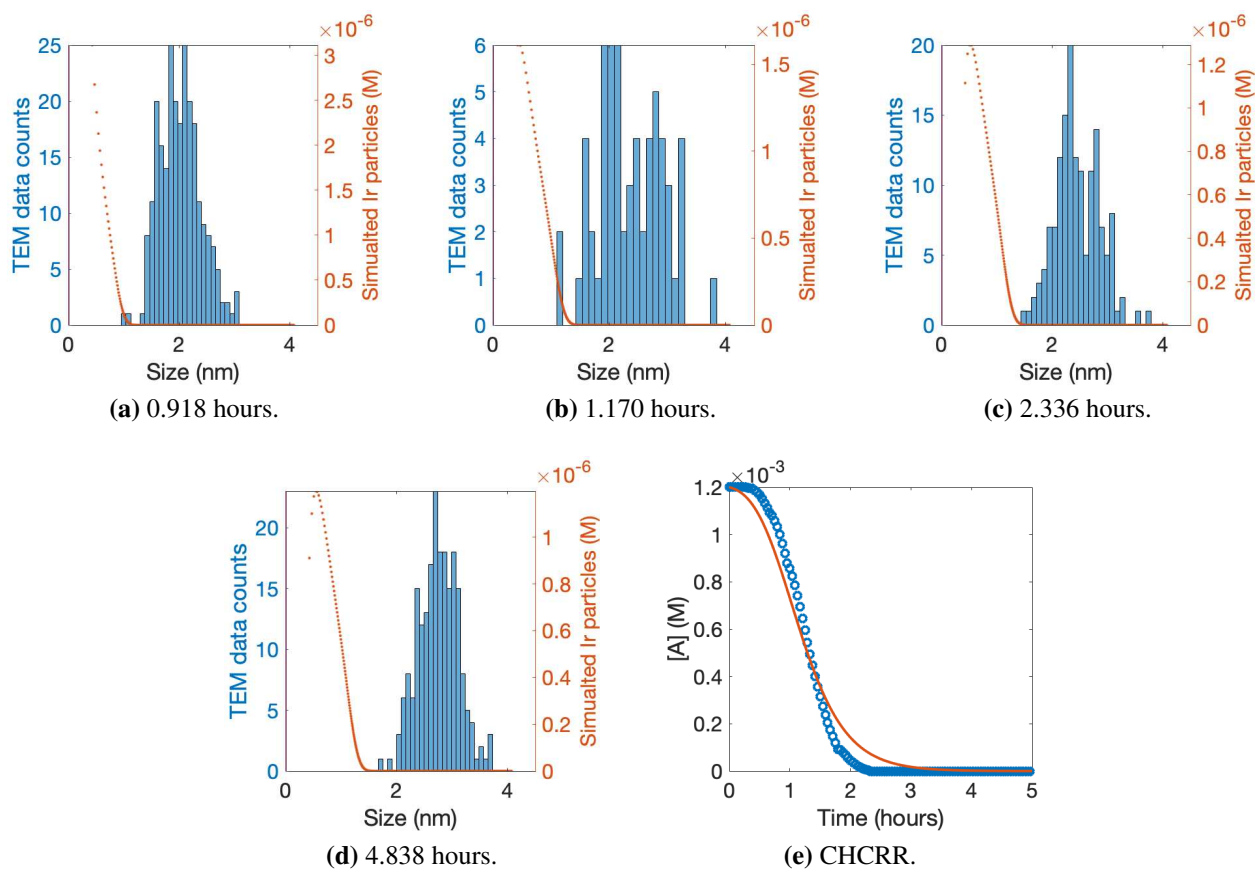


Figure 1.9: Fit to CHCRR curve using the classic FW 2-step mechanism and second-order nucleation. The rate constants produced by the fit are $k_1 = 2.30 \times 10^1 \text{M}^{-1} \text{hr}^{-1}$ and $k_2 = 1.71 \times 10^3 \text{M}^{-1} \text{hr}^{-1}$. These were used to produce the comparison of simulations (red dots) vs. the experimental TEM PSDs (blue histograms). The BFV is 6.87×10^{-4} .

For Figure 1.9 the nucleation order was increased to $\omega = 2$. This resulted in a slightly worse CHCRR curve match since the induction period is not as well fit and there is more second elbow overestimation. However, the simulated PSDs at the third and fourth times, (c) and (d) resp., are now beginning to take on the correct Gaussiansque distributions albeit with much smaller mode and variance.

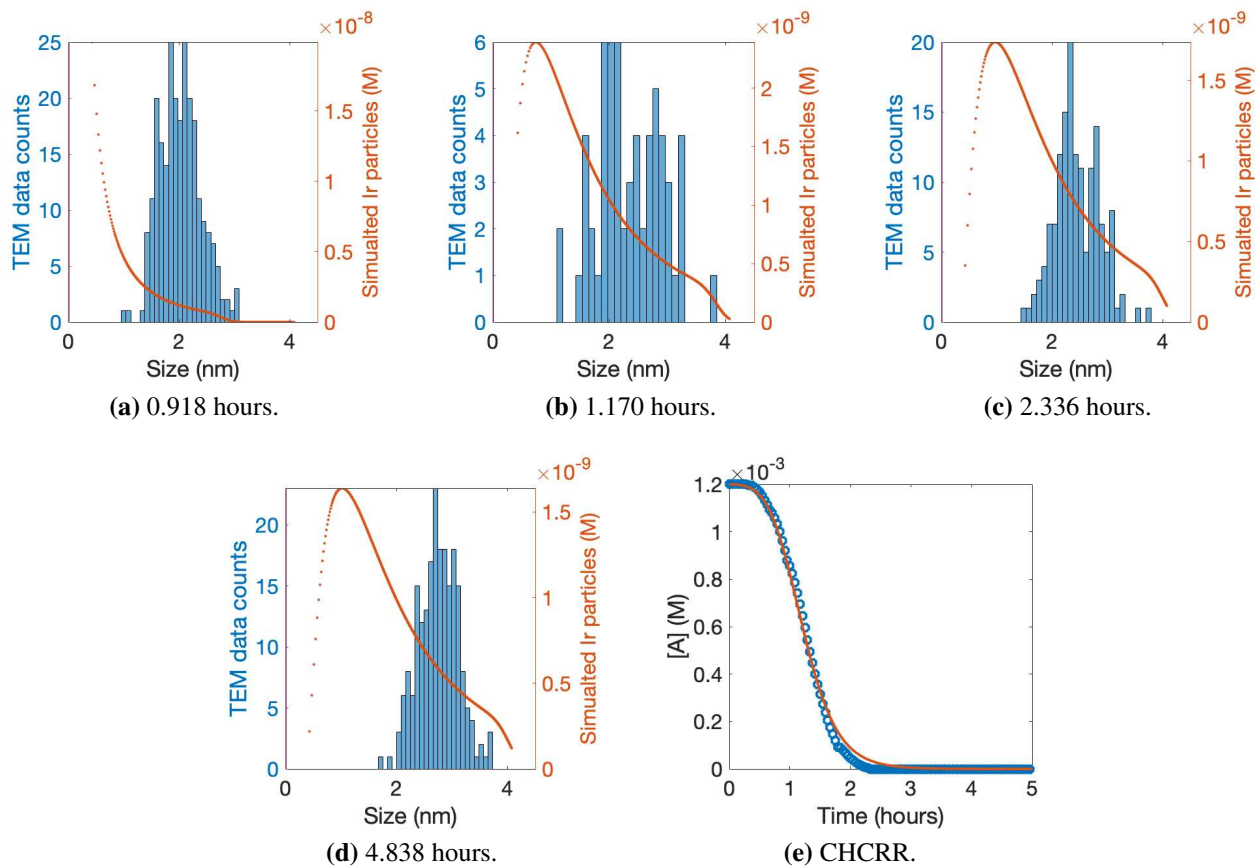


Figure 1.10: Fit to CHCRR curve using the classic FW 2-step mechanism and third-order nucleation by means of `fminsearch`. The rate constants produced by the fit are $k_1 = 9.14 \times 10^2 \text{M}^{-2} \text{hr}^{-1}$ and $k_2 = 6.70 \times 10^3 \text{M}^{-1} \text{hr}^{-1}$. These were used to produce the comparison of simulations (red dots) vs. the experimental TEM PSDs (blue histograms). The BFV is 2.48×10^{-4} .

Third-order nucleation $\omega = 3$ brings us to Figure 1.10 where we have the best fit so far to the CHCRR curve. The second through fourth PSDs now have well defined shapes that range over the TEM data. The modes are still much too small as in the second-order nucleation case, but now the variance is much too large and the simulated PSDs too wide.

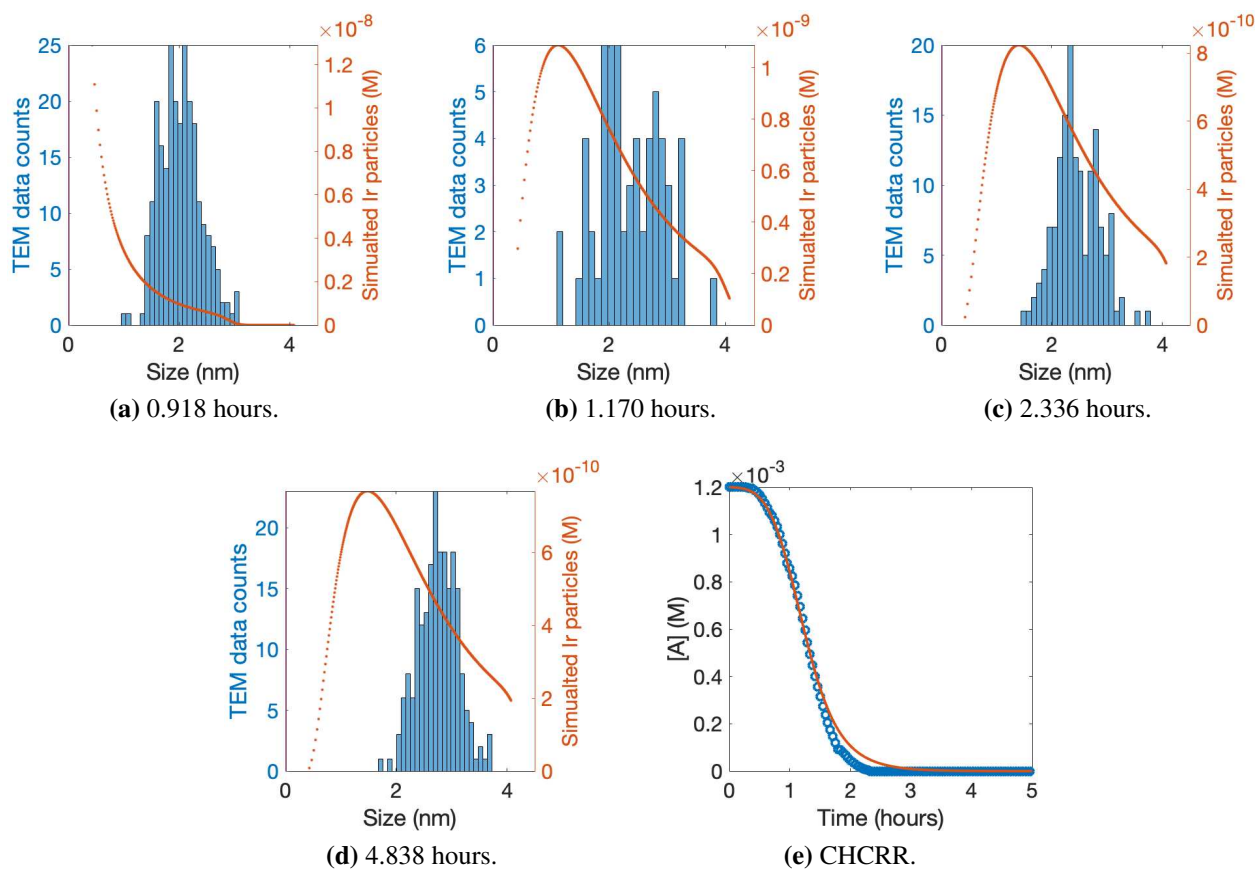


Figure 1.11: Fit to CHCRR curve using the classic FW 2-step mechanism and fourth-order nucleation. The rate constants produced by the fit are $k_1 = 8.61 \times 10^5 \text{M}^{-3} \text{hr}^{-1}$ and $k_2 = 6.93 \times 10^3 \text{M}^{-1} \text{hr}^{-1}$. These were used to produce the comparison of simulations (red dots) vs. the experimental TEM PSDs (blue histograms). The BFV is 3.04×10^{-4} .

In Figure 1.11 we again have a nice match to the CHCRR curve with a slight second elbow overestimate. The resulting PSDs are marginally improved over the third-order simulations in that the mode is slightly larger and there are more larger size particles. With these slight gains the overall fit is still poor.

The apparent trend of increasing nucleation order is that the PSDs improve by a certain extent by the mode moving rightwards, but worsen by having too many larger particles. The first two nucleation orders see none of the the particles growing fast enough and the third and fourth orders see the smaller sized particles growing too slowly whereas the larger sized particles grow too fast resulting in the too wide distributions centered too far left. In all cases the CHCRR fit remains good, although the second-order CHCRR curve is arguably not excellent. The best fit out of the four nucleation orders tested was third-order with its BFV of 2.48×10^{-4} . While none of the simulated PSDs for any nucleation order are satisfactory, the best performing 2-step mechanism in regards to the CHCRR curve is third-order nucleation; a result that is a match to experiment [49].

In addition to fitting the mechanism-enabled population balance model (1.17) to the CHCRR curve we also fit to the fourth and final TEM histogram taken at 4.838 hours which can be seen in Figure 1.12. This fit was performed with third-order nucleation. The leading edge of the PSD is improved over the CHCRR fits. Just as in the previous 2-step fits too much of the particle mass remains in small sizes. In addition, the associated CHCRR curve suffers from an induction period that is too short compared to the experimental measurements. This together with a decrease with too steep of a slope results in a poor CHCRR curve fit.

The simulations performed here for the 2-step mechanism are in agreement with [50] which says that the mechanism is able to follow the reporter reaction, but is unable to match the size distribution. We see from our simulations that regardless of the low nucleation order [49] tested that the 2-step is able to fit well to the CHCRR, but the associated PSDs that come with these fits are poor. The mechanism also fails to match the PSD even if we attempt to fit to the size distribution itself while neglecting the time evolution of precursor. Additional evidence for the mechanism's inability to fit the PSD comes from fitting with bounds of k_1 and k_2 as $[0, \infty)$. The fitting algorithm in this case could not find a suitable PSD near the correct shape and instead minimizes to the worst case scenario of a distribution which is all nucleus and zero elsewhere.

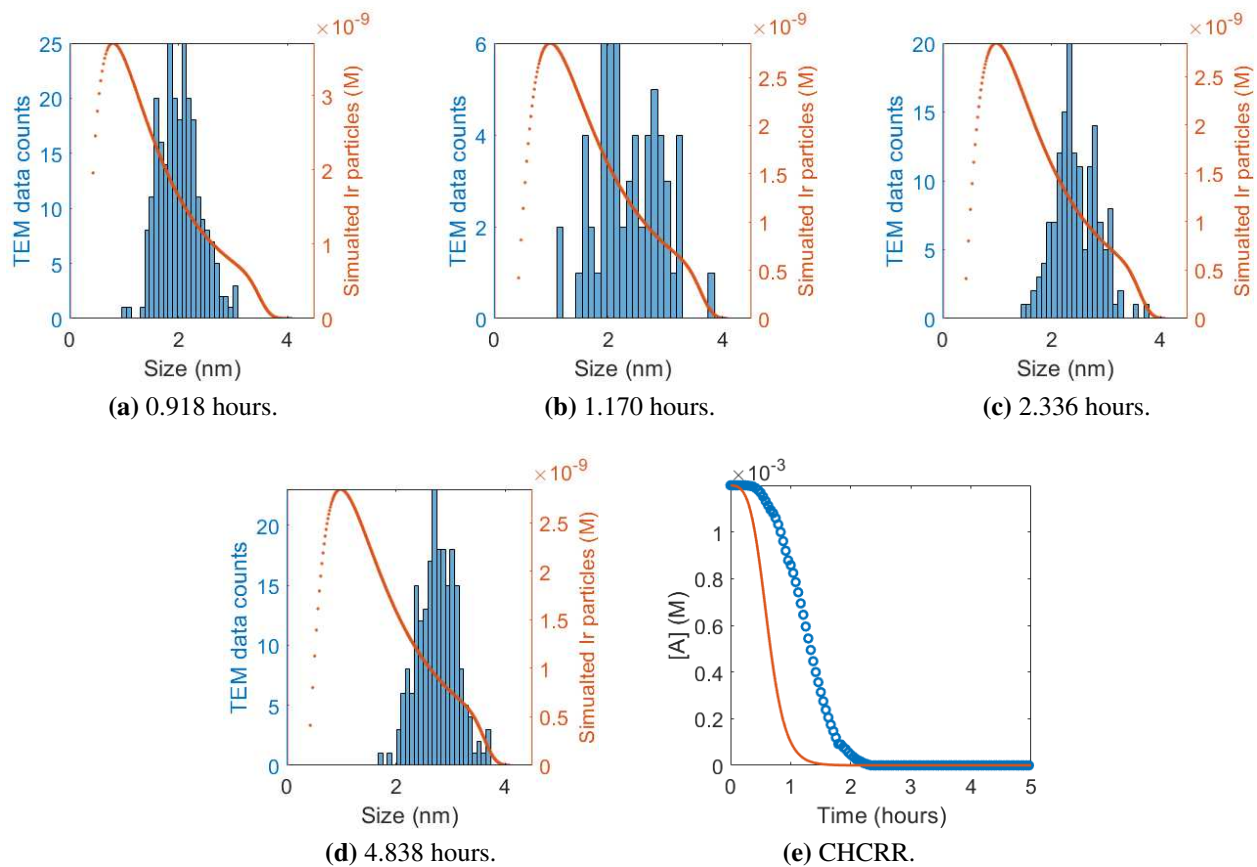


Figure 1.12: Fit to final histogram curve using the classic FW 2-step mechanism and third-order nucleation. The rate constants produced by the fit are $k_1 = 2.46 \times 10^3 \text{M}^{-2} \text{hr}^{-1}$ and $k_2 = 1.18 \times 10^4 \text{M}^{-1} \text{hr}^{-1}$. The BFV is 3.88×10^2 .

1.4.2 Four-Step Mechanism

The simulations in §1.4.1 show that the two-step mechanism is incapable of matching the experimental size distributions for various low nucleation orders. But, is it able to with a modification that keeps low-order nucleation? In keeping with a disproved-based approach, a minimal extension of the model is made in an attempt to find a minimal mechanism capable of matching the experimental distributions. Further minimal extensions to the working model will be added as necessary with the overall goal of finding a minimal mechanism which can produce accurate PSDs. This process is not guaranteed to find such a mechanism, but it will help rule out those that do not work. The first minimal extension of the two-step mechanism is the four-step mechanism [31]



The four steps of the mechanism are (i) slow, continuous nucleation, (ii) autocatalytic surface growth, (iii) bimolecular agglomeration, and (iv) secondary autocatalytic surface growth. This mechanism was the survivor of 18 disproven others based on fitting to the cyclohexene reporter reaction [31]. A notable pair of these disproven mechanisms also have four steps. The first is $A \rightarrow B$, $A + B \rightarrow 2B$, $B + B \rightarrow C$, and $B + C \rightarrow 1.5C$ which we will call the 4_β -step mechanism. The second is $A \rightarrow B$, $A + B \rightarrow 2B$, $A + C \rightarrow 1.5C$, and $B + C \rightarrow 1.5C$ which we will call the 4_γ -step mechanism. A key difference between the 4_β - and 4_γ -step mechanisms and the 4-step is in which particles agglomerate. The two previously disproven mechanisms both have the "small"- "large" autocatalytic agglomeration step of $B + C \rightarrow 1.5C$. It is worth mentioning at this point that this step will result in *larger particles growing faster* than they otherwise would if monomer addition was their only method of growth. We will see below that this is the opposite effect if one wants to achieve accurate size distributions.

Compared to the 2-step mechanism (1.13), these 4-step mechanisms introduce a third particle species C which represents "large" particle sizes. This is another aspect that emphasizes the interpretation requirement for going between mechanism and model. At this point, the distinction between "small" B particles and "large" C particles is arbitrary and needs to be made specific for creation and computation of an ODE system. The monomer addition growth process is now two separate steps, one for the "small" B particles and one for the "large" C particles. This splitting of sizes is morally the 2-step (1.13) where the constant, size-independent growth constant k_2 becomes a size-dependent step function. See the newly developed Mechanism (1.22) in the next section for further insights related to this step function type growth. In addition to the step function monomer growth steps, the 4-step mechanism (1.18) also has agglomeration in the model in the form of the $B + B$ step. Note that this is not complete or arbitrary agglomeration between all particles. This step only says that two "small" particles may interact, but that if a particle is too large it will not be allowed to agglomerate and will only increase in size from monomer growth. Only allowing the smaller particles to agglomerate keeps in line with our minimal extension and disproof approach. Again, this is in contrast to the 4_β - and 4_γ -steps which either have "small"- "small" and "small"- "large", or just "small"- "large" agglomeration respectively. Disallowing "large" particles to agglomerate is also an assumption that can be made by looking at time series TEM images of nanoparticle formation in, for example, either Ir [49, 71], or Pd [74, 75] systems. Due to the very nature of having a near-monodispersed population once the particles achieve certain a size their agglomeration would produce a particle that exceeds any measured. Using the function described in Figure 1.6 we get the following table. Looking at the histograms in Figure 1.1 we see that $2n_{500} \rightarrow n_{1000}$ or $2n_{1000} \rightarrow n_{2000}$ are plausible from the measurements. However, if $2n_{2000} \rightarrow n_{4000}$ were possible we would have particles with diameter 4.76 nm of which there are none at any time. At the second time of 1.170 hours we already see diameters just below 4nm. But this maximum measured particle diameter doesn't increase in either the third or fourth histograms. This together with the assumption that missing "large" particles is far more unlikely than missing

"small" ones while counting from TEM images leads to the conclusion that if agglomeration is happening in the system, it is not with "large" particles.

It is a straightforward process to create a model if one wants to have a single differential equation for each pseudoelementary step species. However, it is necessary to fix the ambiguity of the mechanism with regard to what B and C mean to build an atomistic-based ODE model where there will be an equation for each particle size. This is done by choosing a cutoff $M \in \mathbb{N}$ to be the largest B size so that the explicit sizes for the two species are given by $B = \{n_k \mid k \leq M\}$ and $C = \{n_k \mid k > M\}$. M is a parameter and may either be fixed or variable and fit for during the fitting process and is where the jump occurs in the step function monomer addition growth kernel comprised of the second and fourth steps of (1.18).

Considering the step function approximation of monomer growth, numerical findings indicate that a smaller k_4 is needed compared to k_2 to achieve desirable particle-size distributions giving further disproof to the 4_β -, 4_γ -step mechanisms. This revelation will be seen throughout the other tested mechanisms and leads to one of our main results. In the absence of LaMer-type burst nucleation, *larger particles must react and grow more slowly than smaller particles* to reproduce size distributions that match experiments.

Derivation of Four-Step ODE Model from the Mechanism

The derivation of the 4-step and all other following mechanisms is similar to the 2-step derivation in §1.4.1. We start with interpreting the mechanism to make the concepts of B and C well-defined by using the definitions above. This must be done to convert the mechanism into an ODE system. To see why we must use well-defined versions of the B and C particles refer to the agglomeration step in Figure 1.5. The mechanism says that two "small" particles agglomerate into one "large" particle. However, two "small particles" may actually form another "small" particle. For example, if the cutoff between "small" and "large" is say 40, two particles n_{15} will agglomerate to form an n_{30} which is still "small". We believe that our implementation is a fair interpretation of the mechanism and captures its main idea at the kinetic level.

As there is neither a $B+C$ nor a $C+C$ term in (1.18) we have that agglomeration only involves "small"- "small" particle interaction. Let the growth rate function be

$$k_g = \begin{cases} k_2 & \text{if "small"} \\ k_4 & \text{if "large"}. \end{cases}$$

With the assumption of 3rd order nucleation we have everything we need to create the ODE system for monomers which is

$$\begin{aligned} \frac{dm_1}{dt} &= -3k_1m_1^3 - m_1 \sum_{k=3}^{\infty} k_g b_k \\ \frac{dm_3}{dt} &= 3k_1m_1^3 - 3k_2m_1b_3 - 3k_3b_j \sum_{k=3}^M b_k \\ \frac{dm_{4,5}}{dt} &= jk_2m_1(b_{j-1} - b_j) - jk_3b_j \sum_{k=3}^M b_k \\ \frac{dm_j}{dt} &= jk_2m_1(b_{j-1} - b_j) - jk_3b_j \sum_{k=3}^M b_k + jk_3 \sum_{\substack{i=0 \\ \lfloor j/2 \rfloor - i \geq 3 \\ \lfloor j/2 \rfloor + i + (j \bmod 2) \leq \infty}}^{\infty} b_{\lfloor j/2 \rfloor - i} b_{\lfloor j/2 \rfloor + i + j \bmod 2}, \quad 6 \leq j \leq M \\ \frac{dm_{M+1}}{dt} &= (M+1)m_1(k_3b_M - k_4b_{M+1}) + jk_3 \sum_{\substack{i=0 \\ \lfloor (M+1)/2 \rfloor - i \geq 3 \\ \lfloor (M+1)/2 \rfloor + i + ((M+1) \bmod 2) \leq \infty}}^{\infty} b_{\lfloor (M+1)/2 \rfloor - i} b_{\lfloor (M+1)/2 \rfloor + i + (M+1) \bmod 2} \\ \frac{dm_l}{dt} &= lk_4m_1(b_{l-1} - b_l) + jk_3 \sum_{\substack{i=0 \\ \lfloor j/2 \rfloor - i \geq 3 \\ \lfloor j/2 \rfloor + i + (j \bmod 2) \leq \infty}}^{\infty} b_{\lfloor j/2 \rfloor - i} b_{\lfloor j/2 \rfloor + i + j \bmod 2}, \quad M+2 \leq l < \infty \end{aligned} \tag{1.19}$$

The first equation for the precursor monomers m_1 sees that they are lost to third-order nucleation via the first term and lost to monomer growth via the second. There are no particles of size 2 so we jump to the equation for m_3 which gains particles from nucleation and loses to both monomer growth by the second term and to agglomeration by the third summation term. The equations for $j = 3, 4, 5$ are special since the smallest particle that can be formed by agglomeration is 6 which

occurs when two nuclei combine. Thus, these have no gain from agglomeration terms. The m_j equation represents the remaining B particles of size 6 to M that can be both gained and lost via agglomeration. The m_l equation represents particles that are too large that they can be formed from agglomeration, but they can not be lost to agglomeration since there are no "small"- "large" or "large"- "large" interactions. Since 1.18 only has $B + B$ agglomeration the maximum particle that can be formed via this process is n_{2M} . To reiterate, the m_1 equation represents the precursor A , the m_3 , $m_{4,5}$ and m_j equations together represent the "small" B particles and the m_l equation represents the "large" C particles.

The sums that represent the gain from agglomeration use an index i which starts at zero and increases as usual but only as long as the two constraints are met. The first is that half the current particle size minus the index can only be as small as the nucleus while second is that can be no larger than the maximum C particle size one wishes to model (here set to ∞). For example, for $j = 21$ the first few terms of the sum are $b_{10}b_{11} + b_9b_{12} + b_8b_{13} + \dots$ which will give all the particle-particle combinations that form m_{21} without any overcounting. This agglomeration gain is essentially Smoluchowski's equation (1.9) and (1.10) and we could we could write the sums in (1.19) instead as

$$jk_3 \frac{1}{2} \sum_{i=3}^{j-3} b_i b_{j-i}$$

where the bounds have been modified to reflect the nucleus n_3 being the smallest sized particle available for agglomeration and where we have switched the roles of i and j . Again for the case $j = 21$, the terms in the sum would be $b_3b_{18} + b_4b_{17} + \dots + b_{17}b_4 + b_{18}b_3$. This notation is nicer and more compact, however if there is an odd number of terms in the sum the middle term will be unnecessarily and incorrectly be halved. For example, using (1.10) with $i = 4$ to make n_4 we have $\frac{1}{2} \sum_{j=1}^{i-1} n_j n_{i-j} = \frac{1}{2} (n_1 n_3 + n_2 n_2 + n_3 n_1) = \frac{1}{2} n_2 n_2 + n_1 n_3$. This is not a problem for the continuous formulation of Smoluchowski's equation, see for example [44, 45], since the unnecessary halving will occur on a set of measure zero. The discrete version loses this characteristic as we go from integrating over points to summing over essentially integer sized bins, which are not measure zero. Perhaps a better notation for the sum in question can be seen in [72] which uses $i + j = k$ for the

$\frac{dn_k}{dt}$ equation. In the end, one must be careful to either count everything twice and halve the result or just count everything once.

Using the same $m_k = kn_k$ and $b_k = r(k)m_k$ substitutions as in the two-step, we can transform the monomer system (1.19) into the system for particle size

$$\begin{aligned}
\frac{dn_1}{dt} &= \underbrace{-3k_1n_1^3}_{\text{loss from nucleation}} - \underbrace{n_1 \sum_{k=3}^{\infty} k_g r(k)kn_k}_{\text{loss from growth}} \\
\frac{dn_3}{dt} &= \underbrace{k_1n_1^3}_{\text{gain from nucleation}} - \underbrace{k_2n_1r(3)3n_3}_{\text{loss from growth}} - \underbrace{k_3r(3)3n_3 \sum_{k=3}^M r(k)kn_k}_{\text{loss from agglomeration}} \\
\frac{dn_{4,5}}{dt} &= \underbrace{k_2n_1(r(j-1)(j-1)n_{j-1} - r(j)jn_j)}_{\text{gain and loss from growth}} - \underbrace{k_3r(j)jn_j \sum_{i=3}^M r(i)in_i}_{\text{loss from agglomeration}} \\
\frac{dn_j}{dt} &= \underbrace{k_2n_1(r(j-1)(j-1)n_{j-1} - r(j)jn_j)}_{\text{gain and loss from growth}} - \underbrace{k_3r(j)jn_j \sum_{i=3}^M r(i)in_i}_{\text{loss from agglomeration}} \\
&\quad + \underbrace{k_3 \sum_{\substack{i=0 \\ \mu \geq 3 \\ \nu \leq M}}^{\infty} r(\mu)\mu n_\mu r(\nu)\nu n_\nu}_{\text{gain from agglomeration}}, \quad 6 \leq j \leq M \\
\frac{dn_{M+1}}{dt} &= \underbrace{n_1(k_2r(M)Mn_M - k_4r(M+1)(M+1)n_{M+1})}_{\text{gain and loss from growth}} + \underbrace{k_3 \sum_{\substack{i=0 \\ \mu \geq 3 \\ \nu \leq M}}^{\infty} r(\mu)\mu n_\mu r(\nu)\nu n_\nu}_{\text{gain from agglomeration}} \\
\frac{dn_l}{dt} &= \underbrace{k_4n_1(r(l-1)(l-1)n_{l-1} - r(l)ln_l)}_{\text{gain and loss from growth}} + \underbrace{k_3 \sum_{\substack{i=0 \\ \mu \geq 3 \\ \nu \leq M}}^{\infty} r(\mu)\mu n_\mu r(\nu)\nu n_\nu}_{\text{gain from agglomeration}}, \quad M+2 \leq l < \infty.
\end{aligned} \tag{1.20}$$

Where we make the substitutions $\mu = \lfloor j/2 \rfloor - i$ and $\nu = \lfloor j/2 \rfloor + i + (j \bmod 2)$, respectively for l , and where M is the cutoff between the "small" particles B and the "large" particles C . The "small"- "large" cutoff M also serves as the cutoff for which particles agglomerate, since the class of "large" particles does not agglomerate in this model because there are no $B + C$ or $C + C$ steps. The j sizes are both formed and consumed by the agglomeration process. The l sizes are larger than the maximum agglomeration size M and therefore cannot be consumed by agglomeration, but may potentially still be formed via it up to size $2M$. A separate equation is needed for n_{M+1} since it is formed and lost by monomer addition at different rates.

The sums representing the gains from agglomeration in (1.19) or (1.20) are most easily explained with an example. Say that we want to sum the combinations that make n_{50} . In order to avoid double counting each two number combination and dividing by two we instead only count each pair once, thus also avoiding the incorrect halving of a single term above. The μ and ν particles can be given labels such as left and right or red and blue. We start in the middle with $n_{50} = n_{25} + n_{25}$. Then the left is decreased and the right is increased to $n_{50} = n_{24} + n_{26}$, and so on until the left number μ reaches 3, or the right number ν reaches M . The sum will always stop with the $\mu \geq 3$ condition for B sized particles. For the larger C size particles the $\nu \leq M$ condition is necessary. For example, if we take a "large" C particle n_{100} with $M = 40$ we have that n_{100} cannot be formed from the combination of two "large" n_{50} 's since $50 > M$ and only B particles smaller than M are agglomerating in this model.

Simulations of the 4-step Model

Because of the results in §1.4.1 and [49] we use third-order nucleation for simulations of the 4-step model. In Figure 1.13 we see that (1.20) is able to match the CHCRR curve very well doing better than any nucleation order attempted with the 2-step mechanism. However, the associated four PSDs are quite poor. They have too much mass in the smaller sized particles like the results from the 2-step simulations. A new characteristic that is seen starting in (c) and pronounced in (d) is a second peak making the PSD bimodal, a non-obvious characteristic of the TEM measurements.

The PSDs have a discontinuity in them now due to the step function growth between the B and C species.

Results from fitting (1.20) to the final time histogram are seen in Figure 1.14. Not only are these are remarkable and substantial improvements over the 2-step histogram fits, they also do an objectively great job capturing the shape of the TEM measurement at the fourth measured time. The three earlier time PSDs, which are merely side-effects, match the overall shape of the distributions, but have modes shifted to the right compared to data. The first also has a substantial tail of the smallest particle sizes. The associated CHCRR curve seen in (e) has a considerably shorter induction time and the shape of its second elbow does not match the data. The $A + C \rightarrow 1.5C$ rate constant k_4 produced by the fit is an order of magnitude smaller than the $A + B \rightarrow 2B$ rate k_2 .

The 4-step model produces both better CHCRR fits and better histogram fits compared to the 2-step model. Not only are the histogram fits better, but they actually produce PSDs that are qualitatively similar to the measured data. The models differ by agglomeration and how monomer growth is treated. It would seem then that at least one of these is important to getting the correctly shaped PSDs.

A Second Four-Step Mechanism Tested

The 4_β -step mechanism mentioned above was also tested. The four steps in this mechanism are (i) nucleation, (ii) monomer growth of small particles, (iii) small-small agglomeration, and (iv) small-large agglomeration, producing the mechanism

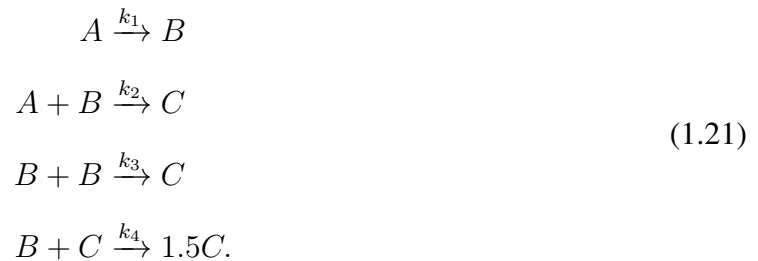


Table 1.1: Table showing the effect doubling the particle size has on diameter. There are no measured particles larger than 3.83 nm during any time. As the experiment duration increases and the nanoparticles reach a low polydispersity they stop increasing in size significantly. This means that agglomeration of "large" particles does not occur. At least, that it does not occur on the time scale of the experiments.

Particle size	Diameter $d(n)$ (nm)
n_{500}	2.38
n_{1000}	3.00
n_{2000}	3.78
n_{4000}	4.76

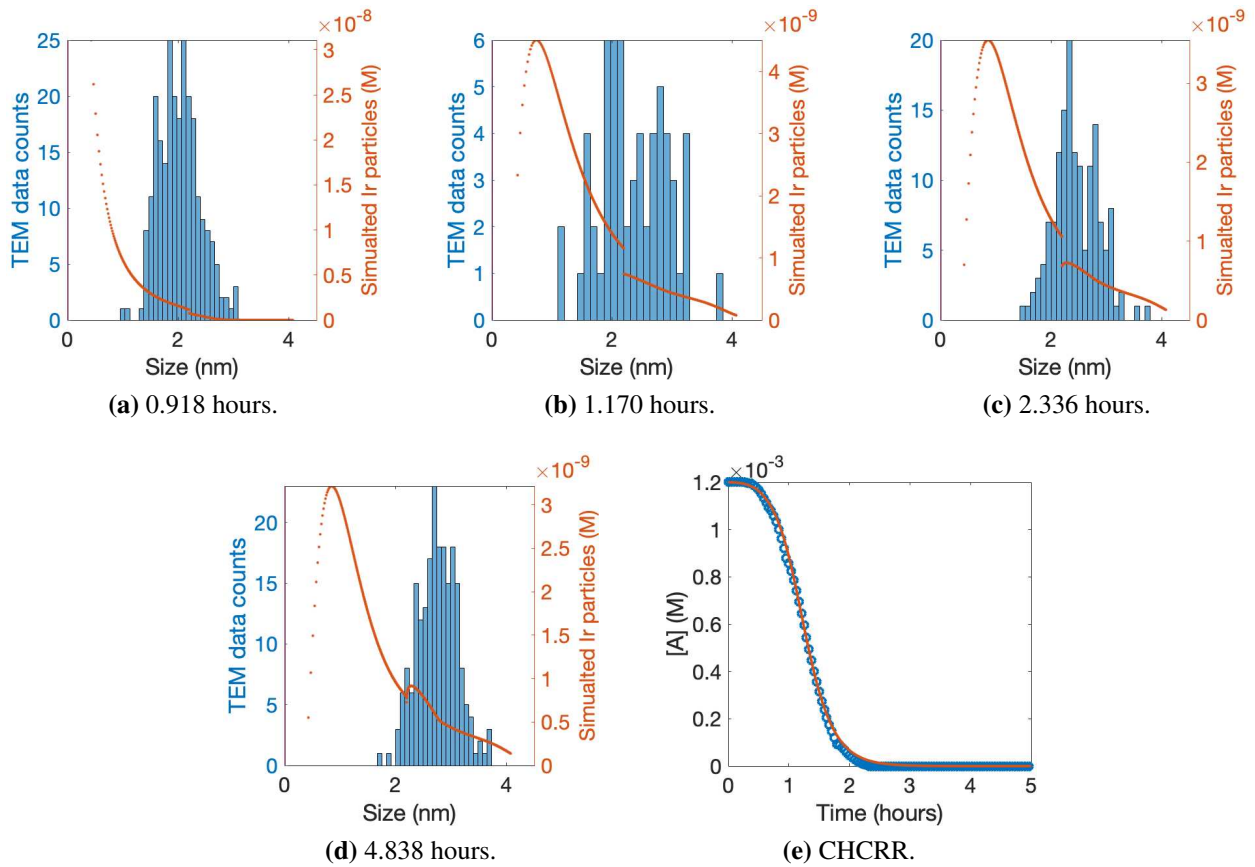


Figure 1.13: Fit to CHCRR curve using the 4-step mechanism and third-order nucleation. The rate constants produced by the fit are $k_1 = 1.06 \times 10^3 \text{M}^{-2} \text{hr}^{-1}$, $k_2 = 5.61 \times 10^3 \text{M}^{-1} \text{hr}^{-1}$, $k_3 = 5.16 \times 10^3 \text{M}^1 \text{hr}^{-1}$, $k_4 = 8.69 \times 10^3 \text{M}^{-1} \text{hr}^{-1}$ with the B vs C cutoff $M = 394$. The BFV is 1.45×10^{-4} . The jumps that now appear in red PSDs result from the step function growth separation of the B and C species.

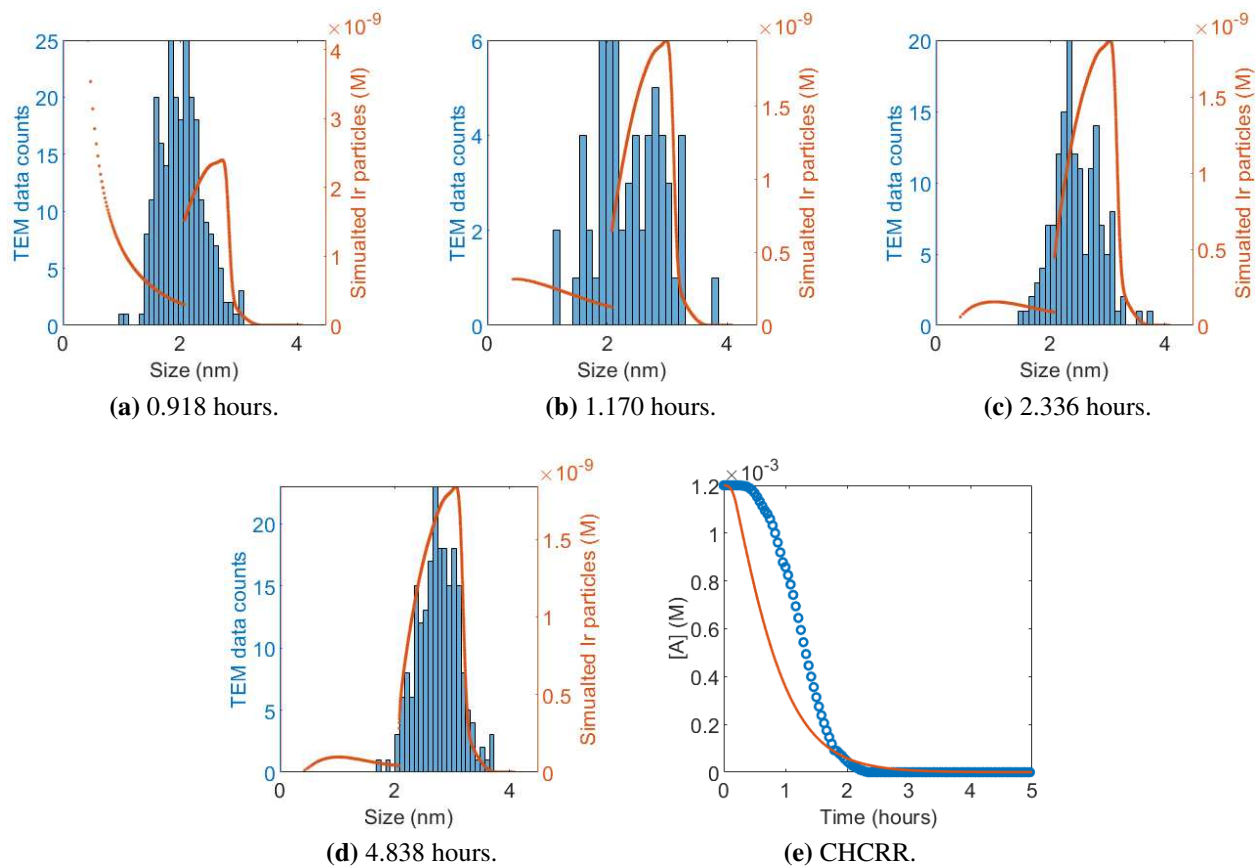


Figure 1.14: Fit to final histogram using the 4-step mechanism and third-order nucleation. The rate constants produced by the fit are $k_1 = 2.71 \times 10^3 \text{M}^{-2} \text{hr}^{-1}$, $k_2 = 2.00 \times 10^4 \text{M}^{-1} \text{hr}^{-1}$, $k_3 = 9.36 \times 10^2 \text{M}^1 \text{hr}^{-1}$, $k_4 = 3.94 \times 10^3 \text{M}^{-1} \text{hr}^{-1}$ with the B vs C cutoff $M = 331$. The BFV is 4.63×10^1 .

This mechanism is the same as the 5-step mechanism (1.33) but with the rate constant for the large particle monomer growth step $A + C \rightarrow 1.5C$ set to zero.

The CHCRR fit for the 4_β -step mechanism is seen in Figure (1.15). The fit yields poor matches to both the PSDs and CHCRR curve. Because there is no monomer growth for large particles, and because small particles are used quickly by both growth and agglomeration, this mechanism has difficulty matching the CHCRR curve. Computation time for this mechanism is significantly increased over the 2-step and first 4-step mechanism due to having agglomeration for all sizes. The increase in computation time is fine for a single simulation but makes the fitting process of repeated simulations rather long and a histogram fit was not performed.

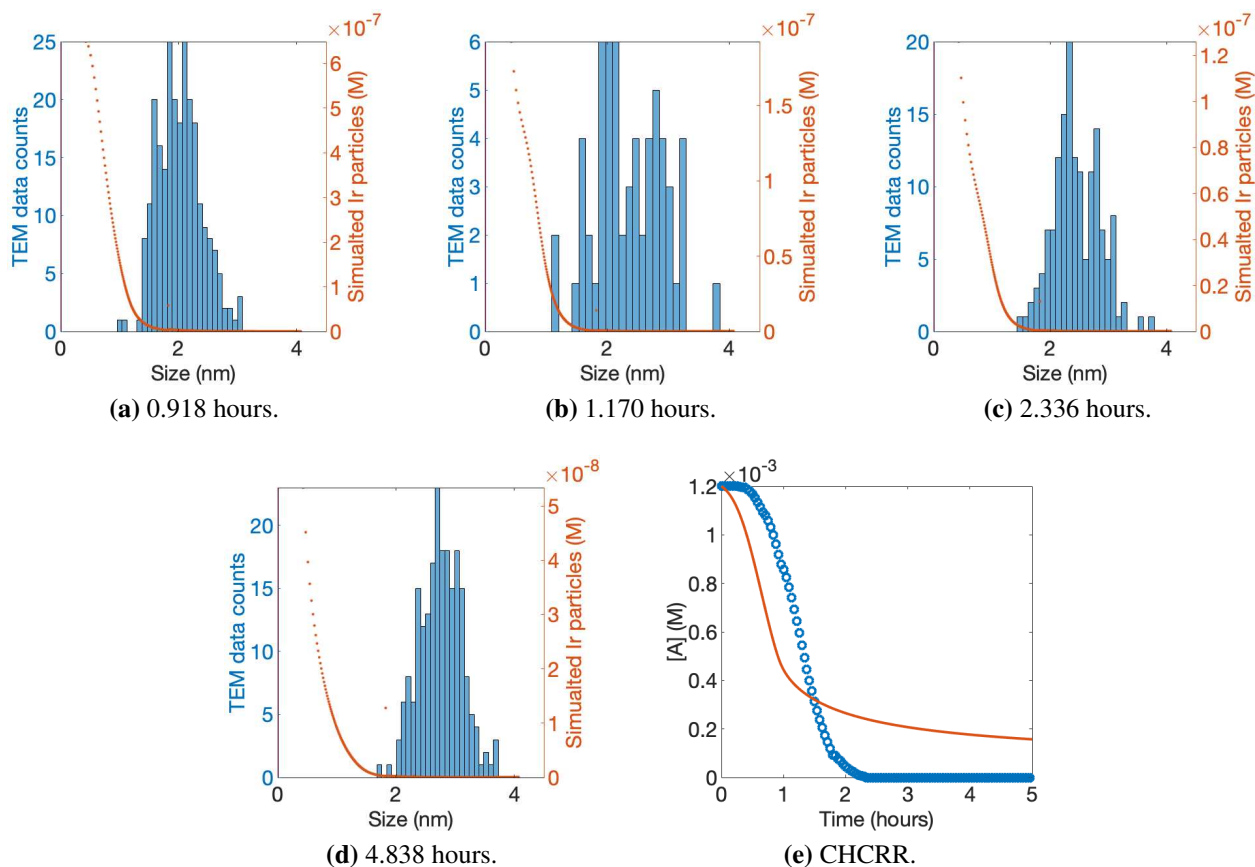


Figure 1.15: Fit to CHCRR curve using the second 4_β -step mechanism (1.21) with third-order nucleation. The rate constants produced by the fit are $k_1 = 3.34 \times 10^4 \text{M}^{-2} \text{hr}^{-1}$, $k_2 = 2.86 \times 10^3 \text{M}^{-1} \text{hr}^{-1}$, $k_3 = 1.44 \times 10^2 \text{M}^1 \text{hr}^{-1}$, $k_4 = 1.44 \times 10^2 \text{M}^{-1} \text{hr}^{-1}$ with the B vs C cutoff $M = 225$. The BFV is 2.40×10^{-3} .

1.4.3 Three-Step Mechanism

The next mechanism tested is the 3-step mechanism which was discovered as a reduction of the 4-step mechanism (1.18) in which the middle two steps of "small"-particle growth and "small"- "small" particle agglomeration are combined. The growth step is $A+B \rightarrow 2B$. The agglomeration step is $B+B=2B \rightarrow C$. The resulting combined step is then $A+B \rightarrow C$. This effectively says that agglomeration can be instead modeled just as monomer growth. The bimolecular agglomeration step, *i.e.* $n_3 + n_3 = n_6$, which can in general move more particle mass to the right faster than monomer addition, can be thought of as monomer addition, *i.e.* $((n_3 + n_1) + n_1) + n_1 = n_6$, albeit with perhaps an increased rate constant to account for the increase in number of reaction steps. The idea to add these two elementary steps together came from numerical fits where the agglomeration rate k_3 of (1.18) was trending towards zero. The resulting 3 pseudoelementary steps of the mechanism are



or rewritten as



to maintain an explicit autocatalytic second step. Mechanisms (1.22) and (1.23) will result in different model systems if the only chemical species are A , B , and C . In our ME-PBM approach the $A+B \rightarrow X$ steps are converted into $n_1 + n_i \rightarrow n_{i+1}$ where the distinction between what a B and what a C is comes not the right-hand side term n_{i+1} , so-called $2B$ or C , but from the left-hand side term n_i .

The origins of the 3-step lie within the 4-step, however is arguable more like the 2-step mechanism. Like the 2-step mechanism (1.13), the 3-step (1.22) is comprised of (i) slow, continuous nucleation $A \rightarrow B$ and (ii) fast autocatalytic growth. However, now we include in the model the idea of "small" and "large" sized particles each of which capable of different growth rates. As seen below, the 3-step mechanism is able to reasonably reproduce particle-size distributions matching those from experimental data. Since, in essence, the 3-step is identical to the 2-step mechanism (processes (i) and (ii)), which cannot produce good distributions, except that the growth kernel is a step function instead of a constant, we have further evidence that the large particles must grow slowly compared to the small particles.

Derivation of Three-Step ODE Model from the Mechanism

Like the previous derivations, the derivation of the 3-step mechanism starts with an ODE system in terms of the monomers which is transformed into a system for particle sizes. The derivation of 3-step model equations follows closely the derivation of the 2-step model. The difference is that the 3-step has separated the non-unitary sized particles into distinct species for "large" and "small" particles like what has been done for (1.18). These two species B and C grow with rate constants k_2 and k_3 . Compared to (1.16) and (1.17) this causes an extra sum term to appear in the equations for m_1 and n_1 and the last equations of (1.16) and (1.17) to be split.

The monomer system is

$$\begin{aligned}
\frac{dm_1}{dt} &= -\omega k_1 m_1^\omega - k_2 m_1 \sum_{i=\omega}^M b_i - k_3 m_1 \sum_{i=M+1}^{\infty} b_i \\
\frac{dm_\omega}{dt} &= \omega k_1 m_1^\omega - \omega k_2 m_1 b_\omega \\
\frac{dm_j}{dt} &= j k_2 m_1 (b_{j-1} - b_j), \quad \omega + 1 \leq j \leq M \\
\frac{dm_{M+1}}{dt} &= (M + 1) k_2 m_1 b_M - (M + 1) k_3 m_1 b_{M+1} \\
\frac{dm_l}{dt} &= l k_3 m_1 (b_{l-1} - b_l), \quad M + 2 \leq l < \infty
\end{aligned} \tag{1.24}$$

which in turn yields the system for particle sizes

$$\begin{aligned}
\frac{dn_1}{dt} &= \underbrace{-\omega k_1 n_1^\omega}_{\text{loss from nucleation}} - \underbrace{k_2 n_1 \sum_{i=\omega}^M ir(i)n_i - k_3 n_1 \sum_{i=M+1}^{\infty} ir(i)n_i}_{\text{loss from growth}} \\
\frac{dn_\omega}{dt} &= \underbrace{k_1 n_1^\omega}_{\text{gain from nucleation}} - \underbrace{\omega k_2 n_1 r(\omega) n_\omega}_{\text{loss from growth}} \\
\frac{dn_j}{dt} &= \underbrace{k_2 n_1 ((j-1)r(j-1)n_{j-1} - jr(j)n_j)}_{\text{gain and loss from growth}}, \quad \omega + 1 \leq j \leq M \quad (1.25) \\
\frac{dn_{M+1}}{dt} &= \underbrace{k_2 n_1 Mr(M)n_M - k_3 n_1 (M+1)r(M+1)n_{M+1}}_{\text{gain and loss from growth}} \\
\frac{dn_l}{dt} &= \underbrace{k_3 n_1 ((l-1)r(l-1)n_{l-1} - lr(l)n_l)}_{\text{gain and loss from growth}}, \quad M + 2 \leq l < \infty
\end{aligned}$$

after using the correct substitutions (see either derivation in §1.4.1 or §1.4.2). The equation for n_1 represents the precursor A . The equation for the nucleus n_ω together with the n_j equation represent "small" particles B . Finally, the n_{M+1} equation and the n_l equation represent "large" particles C . The n_j and n_l both model only monomer addition and are identical other than the first using k_2 and the second k_3 . The species for the first "large" particle n_{M+1} garners its own equation since it gains mass with rate constant k_2 but loses mass with k_3 . Similarly for the m equations.

Simulations of the 3-step Model

Fitting the 3-step mechanism (1.25) to the CHCRR curve results in Figure 1.16. Not only is (1.25) capable of fitting the CHCRR kinetics curve it produces the best match out of the mechanisms tested so far.

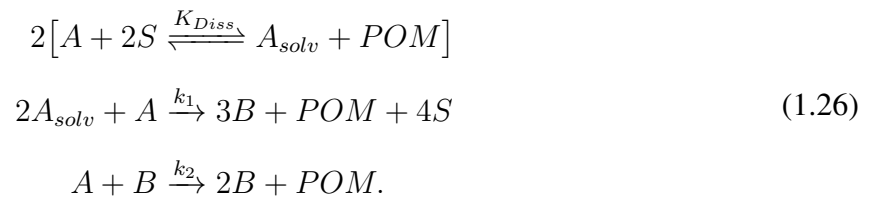
To determine the ability of (1.25) to match the TEM measurements we again fit to the fourth and final histogram. The results are seen in Figure 1.17. While the first time PSD still has a somewhat significant tail of small particles, the PSDs do a nice job of fitting at all times. The first three time PSDs would match better if they were shifted slightly to the left. Similarly to the prior histogram fits, the CHCRR curve is a poor match. It has too short of an induction time and there is a less sudden decrease in precursor resulting in a softer second elbow.

The 3-step mechanism continues the trend of being able to fit the CHCRR curve, but then making poor PSDs seen in the 2- and 4-step mechanisms. Like the 4-step, the 3-step can also match qualitatively the final PSD to the TEM data. Using the BFV as a comparison, the 3-step does a slightly better job at this. The CHCRR curve produced from the histogram fit is close to that produced by the 4-step. Both have a brief induction time and have slopes that become less negative over a longer period of time compared to the measured data. The peaks of the PSDs produced from histogram fitting by the 3-step are smoother compared to those made by the 4-step, but otherwise Figures 1.14 and 1.17 are very similar. Both mechanisms result in a step function monomer growth model and in each case the two growth parameters that come from fitting k_2 and k_4 in (1.20) or k_2 and k_3 in (1.25) see the $A + C$ rate constant being an order of magnitude smaller than the $A + B$ constant.

1.4.4 Two-Step Alternative Termolecular Nucleation

When they showed that nucleation is termolecular, Özkar and Finke [49] included a fast dissociative step wherein the precursor reacts with a solvent to produce a ligand. The ligand, POM in this case, serves to slow down nucleation.

The two-step mechanism, see Mech. 1.13, with the alternative termolecular nucleation is



A fast dissociative step with equilibrium constant $K_{diss} = k_+/k_-$ has been added and the nucleation step of $A \rightarrow B$ has been replaced with the second step above that includes solvent. The three new species involved in alternative nucleation are the ligand POM , the solvent S , and precursor with attached solvent A_{solv} . The nucleation and growth steps produce POM which then changes the balance of the dissociative step and slows nucleation. We skip the system for monomers and go right to the ODE system for the number of particles, which is

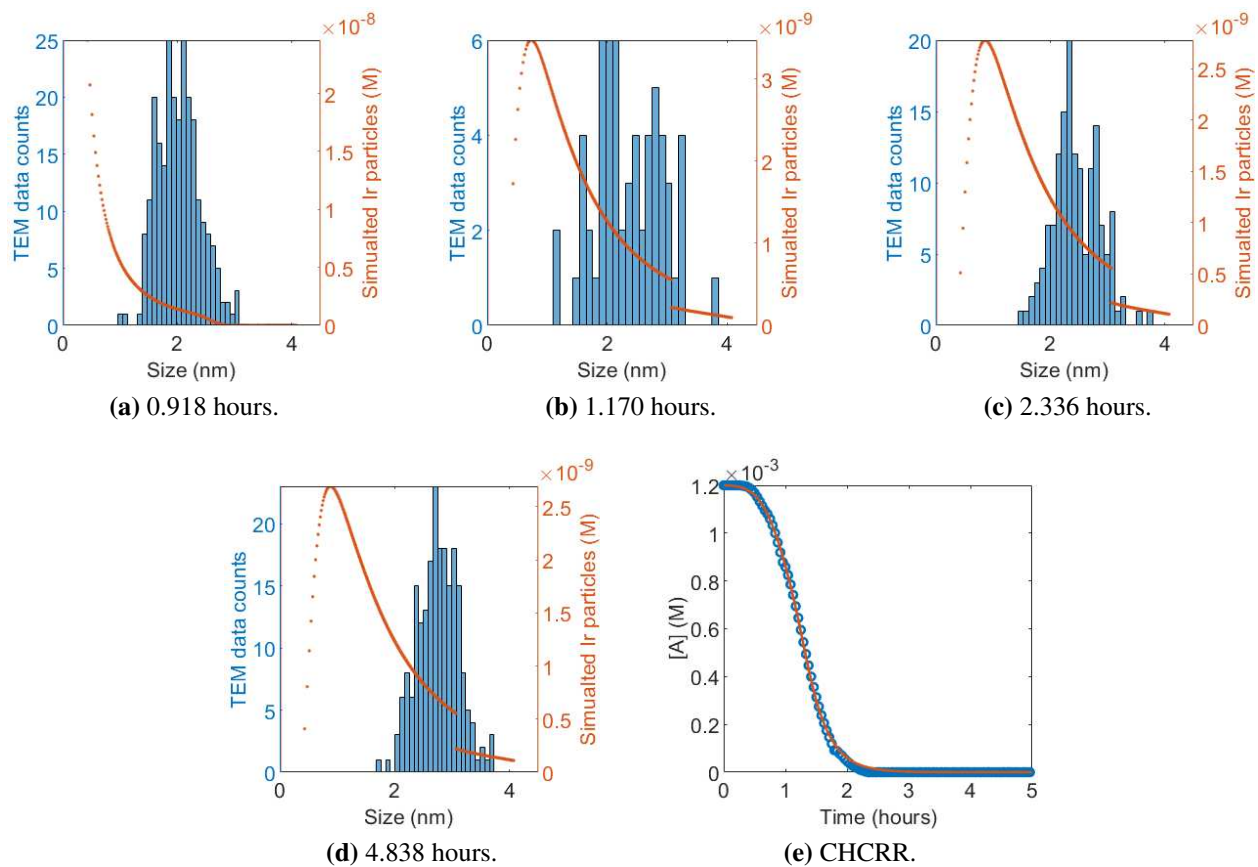


Figure 1.16: Fit to CHCRR curve using the 3-step mechanism and third-order nucleation. The rate constants produced by the fit are $k_1 = 9.78 \times 10^3 \text{M}^{-2} \text{hr}^{-1}$, $k_2 = 6.19 \times 10^3 \text{M}^{-1} \text{hr}^{-1}$, $k_3 = 1.57 \times 10^4 \text{M}^1 \text{hr}^{-1}$ with the B vs C cutoff $M = 1068$. The BFV is 1.15×10^{-4} .

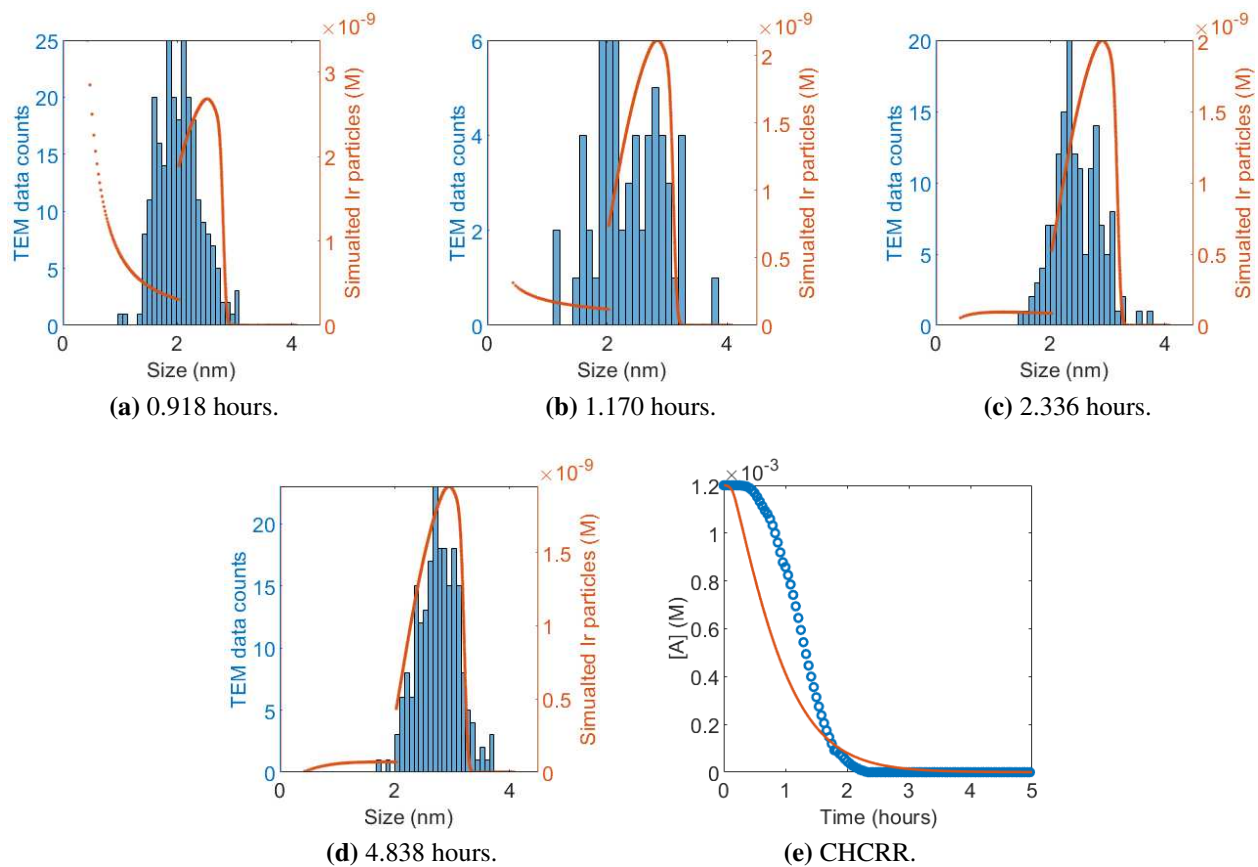


Figure 1.17: Fit to final histogram using the 3-step mechanism and third-order nucleation. The rate constants produced by the fit are $k_1 = 1.95 \times 10^3 \text{M}^{-2} \text{hr}^{-1}$, $k_2 = 2.24 \times 10^4 \text{M}^{-1} \text{hr}^{-1}$, $k_3 = 3.63 \times 10^3 \text{M}^1 \text{hr}^{-1}$ with the B vs C cutoff $M = 308$. The BFV is 4.43×10^1 .

$$\begin{aligned}
\frac{dn_1}{dt} &= \underbrace{-k_1 n_1 n_s^2}_{\text{loss from nucleation}} - \underbrace{k_2 n_1 \sum_{i=3}^{\infty} ir(i)n_i}_{\text{loss from growth}} - \underbrace{k_+ n_1 s^2 + k_- n_s p}_{\text{fast diss step}} \\
\frac{dn_s}{dt} &= \underbrace{k_+ n_1 s^2 - k_- n_s p}_{\text{fast diss step}} - \underbrace{2k_1 n_1 n_s^2}_{\text{loss from nucleation}} \\
\frac{dp}{dt} &= \underbrace{k_+ n_1 s^2 - k_- n_s p}_{\text{fast diss step}} + \underbrace{k_1 n_1 n_s^2}_{\text{gain from nucleation}} + \underbrace{k_2 n_1 \sum_{i=3}^{\infty} ir(i)n_i}_{\text{gain from growth}} \\
\frac{dn_3}{dt} &= \underbrace{k_1 n_1 n_s^2}_{\text{gain from nucleation}} - \underbrace{k_2 n_1 r(3)3n_3}_{\text{loss from growth}} \\
\frac{dn_j}{dt} &= \underbrace{k_2 n_1 (r(j-1)(j-1)n_{j-1} - r(j)jn_j)}_{\text{gain and loss from growth}}, \quad 4 \leq j < \infty
\end{aligned} \tag{1.27}$$

where the new species n_s represents the amount of A_{solv} , and p represents POM .

Simulations of 2-step Model with Alternative Nucleation

The CHCRR fit seen in Figure 1.18 shows that when the experimentally correct alternative termolecular nucleation is added to the 2-step mechanism the resulting alternative 2-step mechanism (1.26) is still capable of matching the reporter reaction. The PSDs are more accurately shaped compared to the standard termolecular nucleation of Figure 1.10, but like the standard nucleation case, the alternative nucleation PSDs have too many small particles and a variance which is too large.

Using (1.27) to fit to the final histogram gives Figure 1.19 where it seems that the mechanism is unable to produce PSDs with small enough polydispersity. CHCRR curve is also very poor. The rapid depletion of precursor seen in the simulated CHCRR curve is also apparent in the PSDs since they do not suffer from the common fault of having too many smaller particles.

1.4.5 Four-Step Alternative Termolecular Nucleation

The 4-step mechanism (1.18) with standard nucleation replaced with alternative nucleation is

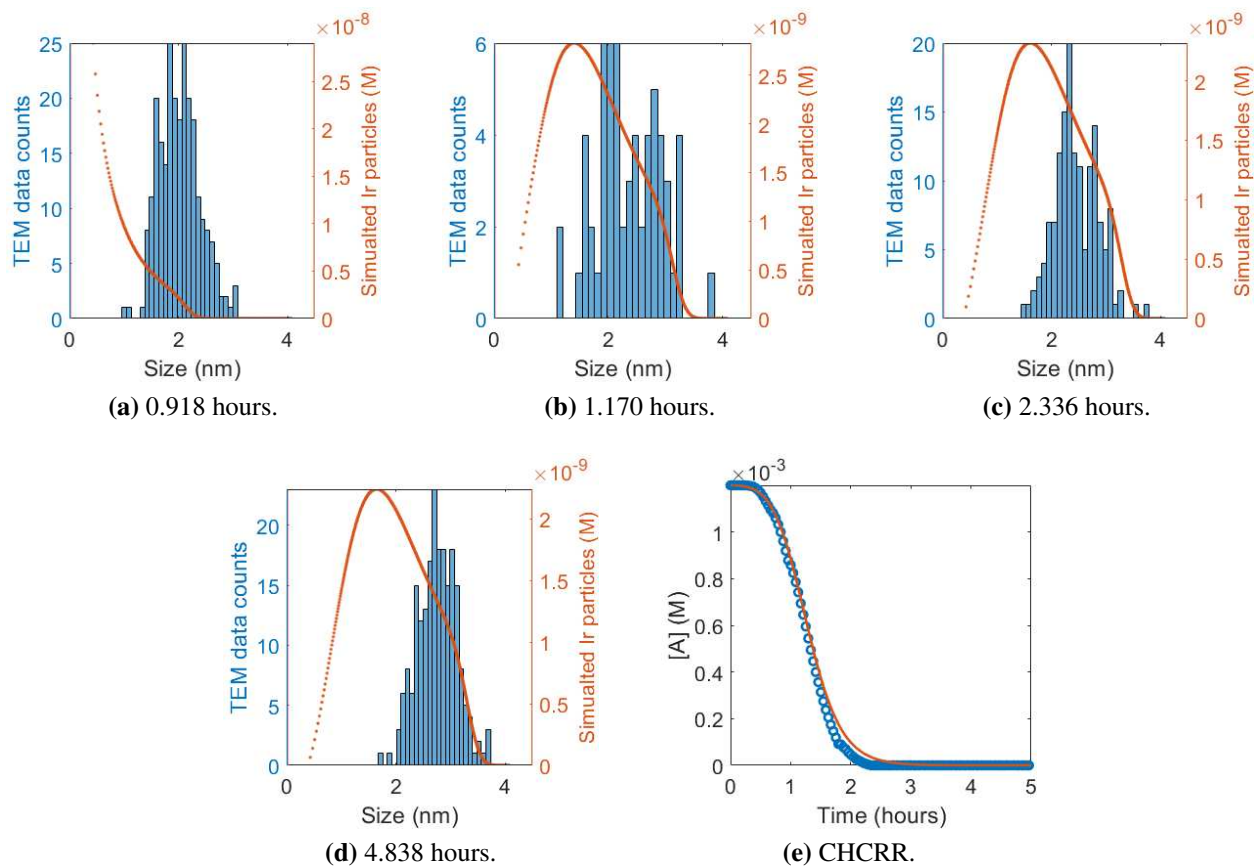


Figure 1.18: Fit to CHCRR curve using the 2-step mechanism and alternative nucleation. The rate constants produced by the fit are $k_1 = 4.80 \times 10^4 \text{M}^{-2}\text{hr}^{-1}$, $k_2 = 6.50 \times 10^3 \text{M}^{-1}\text{hr}^{-1}$. The BFV is 1.04×10^{-3} . The initial solvent amount is 11.3 M. The dissociative rate constants are $k_+ = 3.60 \times 10^{-2}$ and $k_- = 7.27 \times 10^4$.

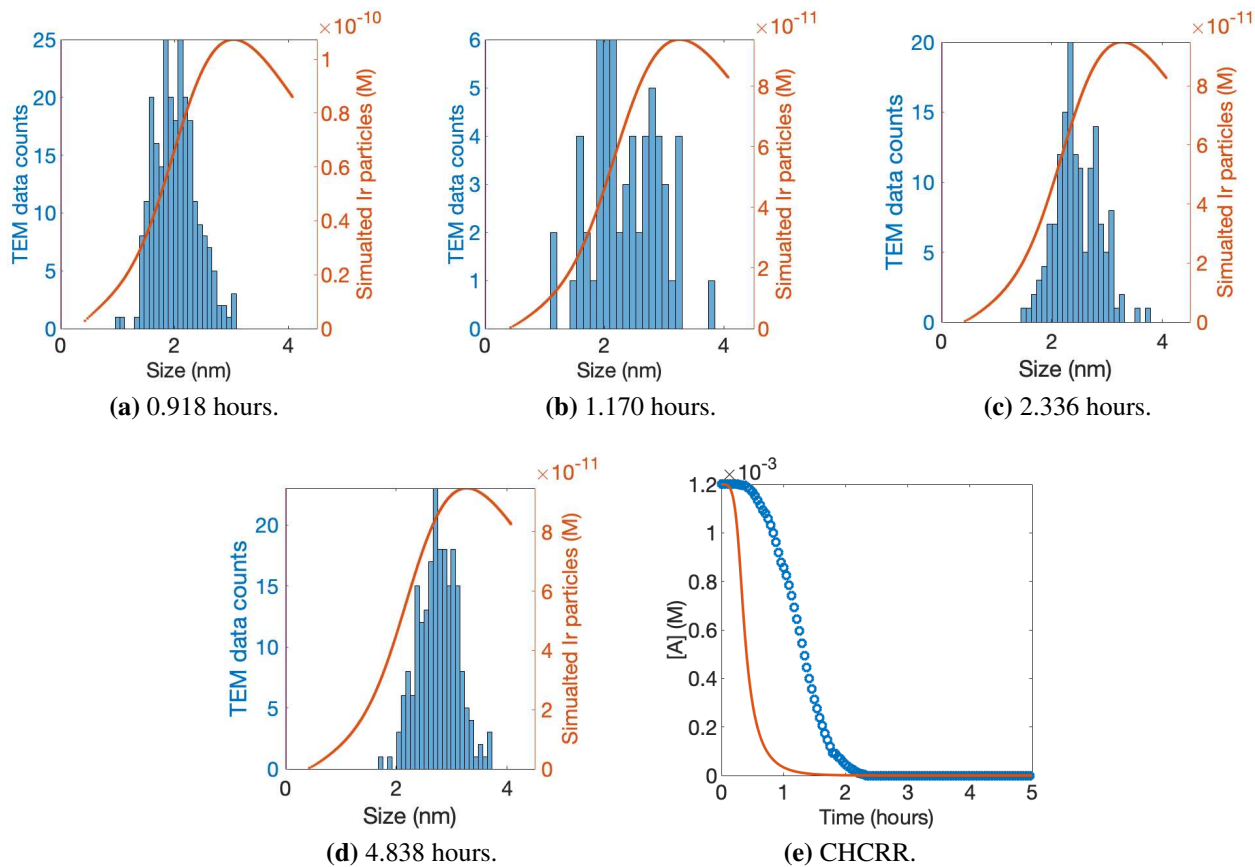
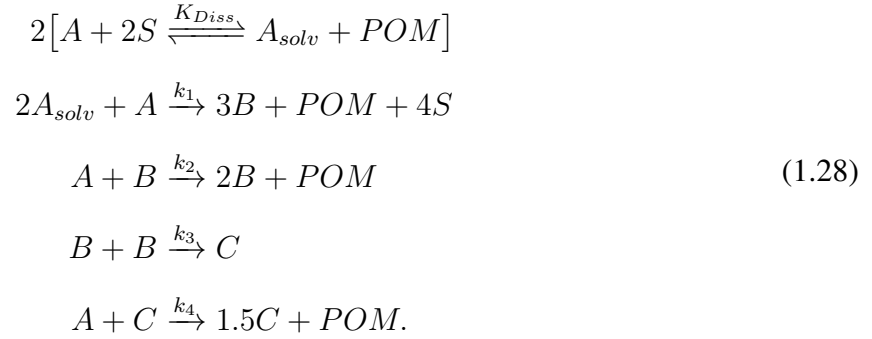


Figure 1.19: Fit to fourth histogram using the 2-step mechanism and alternative nucleation. The rate constants produced by the fit are $k_1 = 4.80 \times 10^4 \text{M}^{-2} \text{hr}^{-1}$, $k_2 = 3.99 \times 10^4 \text{M}^{-1} \text{hr}^{-1}$. The BFV is 2.53×10^2 . The initial solvent amount is 11.3 M. The dissociative rate constants are $k_+ = 3.60 \times 10^{-2}$ and $k_- = 7.27 \times 10^4$.



The *POM* ligand is created whenever the precursor *A* is involved in a step so is not present in the agglomeration step. Similarly to the standard four-step, the alt-termol four-step has the same nucleation as the two-step, has an additional small-small agglomeration step, and the growth step is split into large and small.

We again omit the derivation of the monomer model due to similarity to the previous derivations. The ODE system for the alternative 4-step mechanism in terms of particle size is

$$\begin{aligned}
\frac{dn_1}{dt} &= \underbrace{-k_1 n_1 n_s^2}_{\text{loss from nucleation}} - \underbrace{k_2 n_1 \sum_{i=3}^M ir(i)n_i}_{\text{loss from small growth}} - \underbrace{k_3 n_1 \sum_{i=M+1}^{\infty} ir(i)n_i}_{\text{loss from large growth}} - \underbrace{k_+ n_1 s^2 + k_- n_s p}_{\text{fast diss step}} \\
\frac{dn_s}{dt} &= \underbrace{k_+ n_1 s^2 - k_- n_s p}_{\text{fast diss step}} - \underbrace{2k_1 n_1 n_s^2}_{\text{loss from nucleation}} \\
\frac{dp}{dt} &= \underbrace{k_+ n_1 s^2 - k_- n_s p}_{\text{fast diss step}} + \underbrace{k_1 n_1 n_s^2}_{\text{gain from nucleation}} + \underbrace{k_2 n_1 \sum_{i=3}^M ir(i)n_i}_{\text{gain from small growth}} + \underbrace{k_3 n_1 \sum_{i=M+1}^{\infty} ir(i)n_i}_{\text{gain from large growth}} \\
\frac{dn_3}{dt} &= \underbrace{k_1 n_1 n_s^2}_{\text{gain from nucleation}} - \underbrace{k_2 n_1 r(3)3n_3}_{\text{loss from growth}} - \underbrace{k_3 r(3)3n_3 \sum_{k=3}^M r(k)kn_k}_{\text{loss from agglomeration}} \\
\frac{dn_{4,5}}{dt} &= \underbrace{k_2 n_1 (r(j-1)(j-1)n_{j-1} - r(j)jn_j)}_{\text{gain and loss from growth}} - \underbrace{k_3 r(j)jn_j \sum_{k=3}^M r(k)kn_k}_{\text{loss from agglomeration}} \\
&\quad \underbrace{k_2 n_1 (r(j-1)(j-1)n_{j-1} - r(j)jn_j)}_{\text{gain and loss from growth}} - \underbrace{k_3 r(j)jn_j \sum_{k=3}^M r(k)kn_k}_{\text{loss from agglomeration}} \\
\frac{dn_j}{dt} &= \underbrace{k_3 \sum_{\substack{i=0 \\ \mu \geq 3 \\ \nu \leq M}}^{\infty} r(\mu)\mu n_\mu r(\nu)\nu n_\nu}_{\text{gain from agglomeration}}, \quad 4 \leq j \leq M \\
\frac{dn_{M+1}}{dt} &= \underbrace{k_2 n_1 M r(M)n_M - k_3 n_1 (M+1)r(M+1)n_{M+1}}_{\text{gain and loss from growth}} + \underbrace{k_3 \sum_{\substack{i=0 \\ \mu \geq 3 \\ \nu \leq M}}^{\infty} r(\mu)\mu n_\mu r(\nu)\nu n_\nu}_{\text{gain from agglomeration}} \\
\frac{dn_l}{dt} &= \underbrace{k_3 n_1 ((l-1)r(l-1)n_{l-1} - lr(l)n_l)}_{\text{gain and loss from growth}} + \underbrace{k_3 \sum_{\substack{i=0 \\ \mu \geq 3 \\ \nu \leq M}}^{\infty} r(\mu)\mu n_\mu r(\nu)\nu n_\nu}_{\text{gain from agglomeration}}, \quad M+2 \leq l < \infty
\end{aligned} \tag{1.29}$$

where the n_1 equation is for the precursor species A , the n_s equation is for the A_{solv} species, p is for POM, the n_3 , $n_{4,5}$, and n_j equations are for "small" particles B , and finally the n_{M+1} and n_l equations are for the "large" particles C .

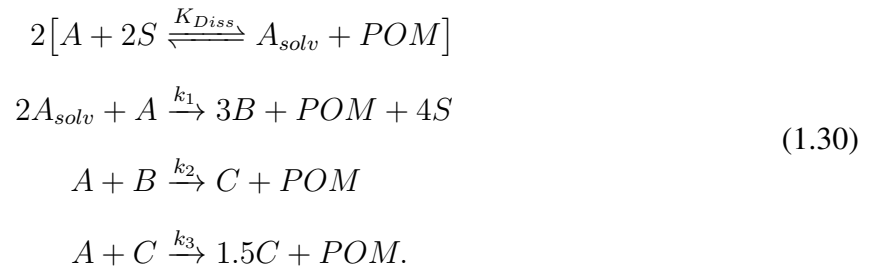
Simulations of 4-step Model with Alternative Nucleation

The CHCRR and histogram fits using (1.29) are seen in Figures 1.20 and 1.21. The CHCRR fit is adequate but has difficulty matching the induction phase. The PSDs from the CHCRR, in addition to the now common trend of having too many small particles, become bimodal with time. This behavior is not seen in the apparent unimodal TEM data.

The histogram fit shows that the addition of the correct alternative nucleation to the 4-step does not remove its capability of producing accurate unimodal PSDs. The companion CHCRR simulation is better than the standard termolecular 4-step simulation, but still uses too much precursor during the early times. The peaks of the PSDs are smoother and the overall shape is better compared to the standard nucleation case in Figure 1.14.

1.4.6 Three-Step Alternative Termolecular Nucleation

Adding the alternative nucleation steps and needed extra species to the best performing new three-step Mechanism (1.22) gives Mechanism (1.30). The associated system of ODEs is seen in (1.31) where each term is labeled with a short description. Again, the intermediate size between "large" and "small" particles grows and loses with two different rate constants and requires its own equation.



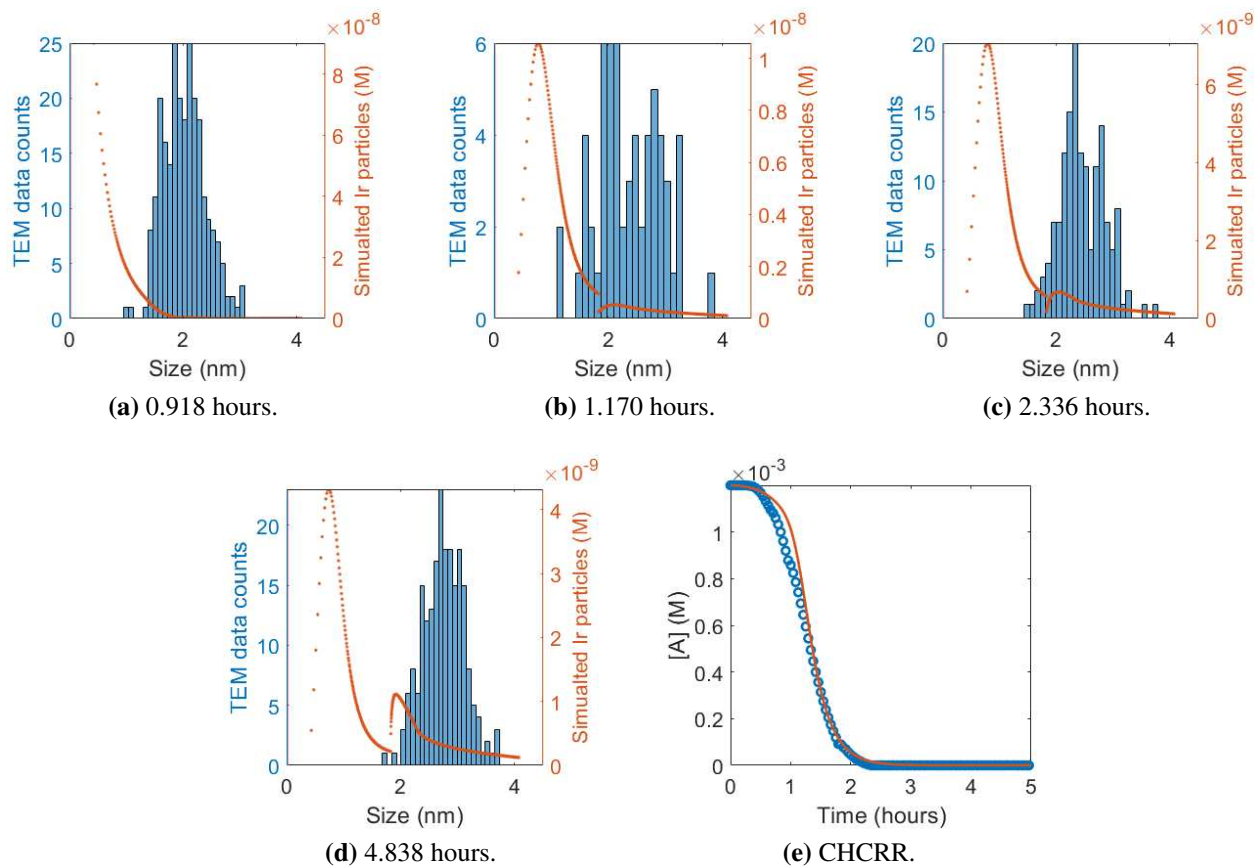


Figure 1.20: Fit to CHCRR curve using the 4-step mechanism and alternative nucleation. The rate constants produced by the fit are $k_1 = 5.99 \times 10^4 \text{M}^{-2} \text{hr}^{-1}$, $k_2 = 4.21 \times 10^3 \text{M}^{-1} \text{hr}^{-1}$, $k_3 = 6.24 \times 10^2 \text{M}^{-1} \text{hr}^{-1}$, $k_4 = 1.68 \times 10^4 \text{M}^{-1} \text{hr}^{-1}$, and B vs. C particle size cutoff $M = 225$. The BFV is 9.55×10^{-4} . The initial solvent amount is 11.3 M. The dissociative rate constants are $k_+ = 3.60 \times 10^{-2}$ and $k_- = 7.27 \times 10^4$.

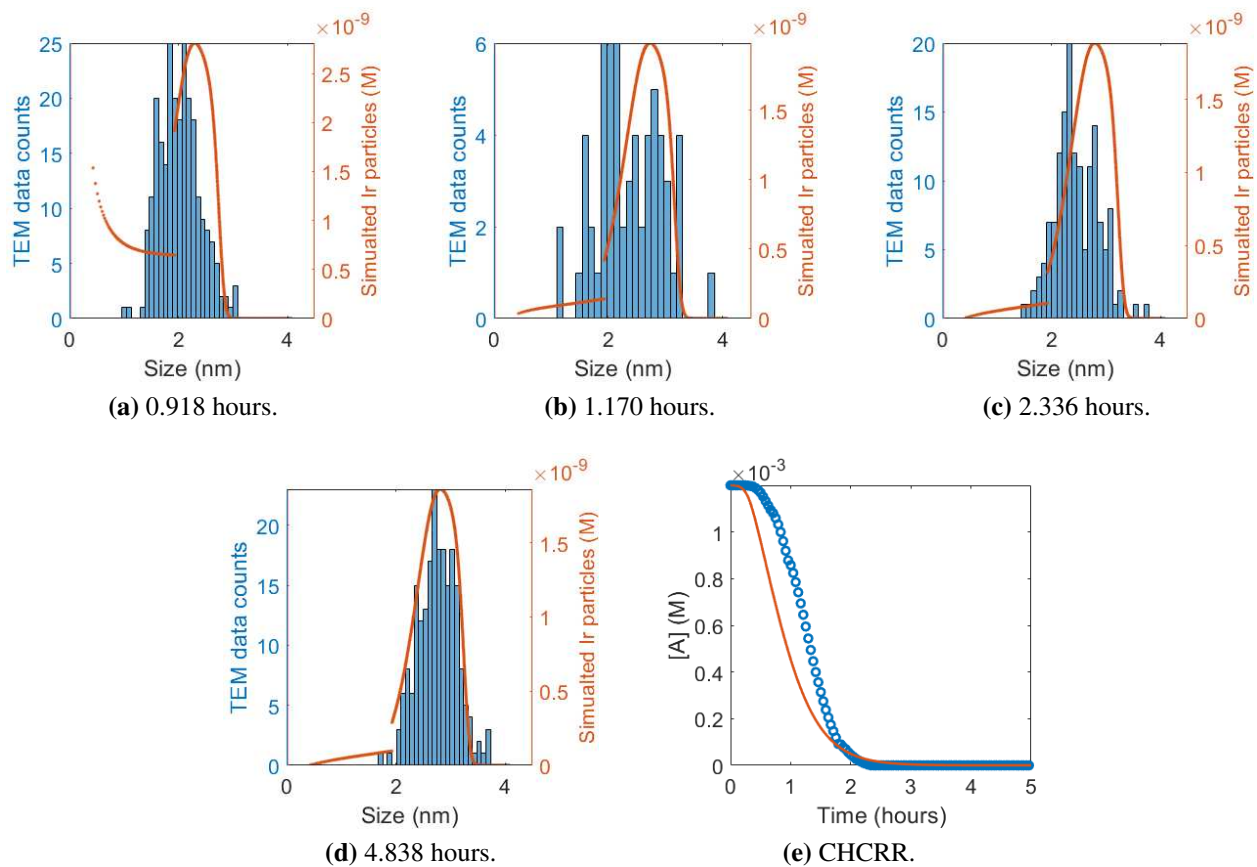


Figure 1.21: Fit to fourth histogram curve using the 4-step mechanism and alternative nucleation. The rate constants produced by the fit are $k_1 = 6.40 \times 10^4 \text{M}^{-2} \text{hr}^{-1}$, $k_2 = 1.61 \times 10^4 \text{M}^{-1} \text{hr}^{-1}$, $k_3 = 1.20 \times 10^1 \text{M}^{-1} \text{hr}^{-1}$, $k_4 = 5.45 \times 10^3 \text{M}^{-1} \text{hr}^{-1}$, and B vs. C particle size cutoff $M = 265$. The BFV is 2.96×10^1 . The initial solvent amount is 11.3 M. The dissociative rate constants are $k_+ = 3.60 \times 10^{-2}$ and $k_- = 7.27 \times 10^4$.

$$\begin{aligned}
\frac{dn_1}{dt} &= \underbrace{-k_1 n_1 n_s^2}_{\text{loss from nucleation}} - \underbrace{k_2 n_1 \sum_{i=3}^M ir(i)n_i}_{\text{loss from small growth}} - \underbrace{k_3 n_1 \sum_{i=M+1}^{\infty} ir(i)n_i}_{\text{loss from large growth}} - \underbrace{k_+ n_1 s^2 + k_- n_s p}_{\text{fast diss step}} \\
\frac{dn_s}{dt} &= \underbrace{k_+ n_1 s^2 - k_- n_s p}_{\text{fast diss step}} - \underbrace{2k_1 n_1 n_s^2}_{\text{loss from nucleation}} \\
\frac{dp}{dt} &= \underbrace{k_+ n_1 s^2 - k_- n_s p}_{\text{fast diss step}} + \underbrace{k_1 n_1 n_s^2}_{\text{gain from nucleation}} + \underbrace{k_2 n_1 \sum_{i=3}^M ir(i)n_i}_{\text{gain from small growth}} + \underbrace{k_3 n_1 \sum_{i=M+1}^{\infty} ir(i)n_i}_{\text{gain from large growth}} \\
\frac{dn_3}{dt} &= \underbrace{k_1 n_1 n_s^2}_{\text{gain from nucleation}} - \underbrace{k_2 n_1 r(3)3n_3}_{\text{loss from growth}} \\
\frac{dn_j}{dt} &= \underbrace{k_2 n_1 (r(j-1)(j-1)n_{j-1} - r(j)jn_j)}_{\text{gain and loss from growth}}, \quad 4 \leq j \leq M \\
\frac{dn_{M+1}}{dt} &= \underbrace{k_2 n_1 Mr(M)n_M - k_3 n_1 (M+1)r(M+1)n_{M+1}}_{\text{gain and loss from growth}} \\
\frac{dn_l}{dt} &= \underbrace{k_3 n_1 ((l-1)r(l-1)n_{l-1} - lr(l)n_l)}_{\text{gain and loss from growth}}, \quad M+2 \leq l < \infty
\end{aligned} \tag{1.31}$$

The results from fitting (1.31) to the CHCRR curve are in Figure 1.22. Similarly to the alternative nucleation 4-step results, the CHCRR curve is a fair match with a slight overshoot on the induction period. The associated PSDs are centered too far to the left since they do not contain large enough particles.

Figure 1.23 has the histogram fit results for (1.31). The fourth time histogram shows an excellent match to the TEM measurements. The earlier time PSDs are slightly more advanced than the data, but all have nice shapes. The corresponding CHCRR curve is similar in shape to the data but does not have a long enough induction period.

The previous two fits were done using the standard polling option for `patternsearch`. Using the complete polling option, see §1.10.1, results a final histogram that is nearly identical to the standard polling method as seen in Figure 1.24. This similarity is seen in both the corresponding figures and also in similar BFVs. The parameters resulting from the two polling methods are the same to 3 significant digits. In this instance, the choice of polling method was inconsequential.

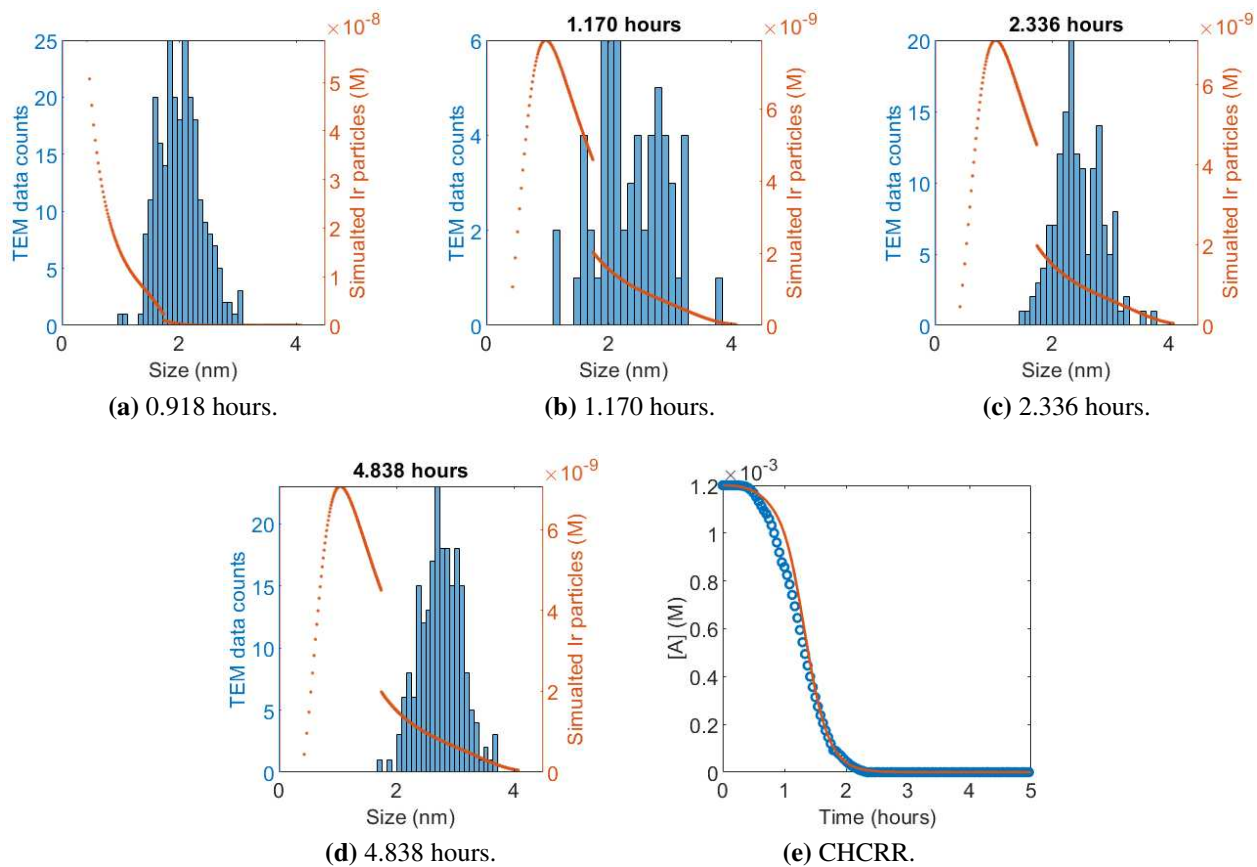


Figure 1.22: Fit to CHCRR curve using the 3-step mechanism and alternative nucleation. The rate constants produced by the fit are $k_1 = 4.97 \times 10^4 \text{M}^{-2} \text{hr}^{-1}$, $k_2 = 4.97 \times 10^3 \text{M}^{-1} \text{hr}^{-1}$, $k_3 = 1.12 \times 10^4 \text{M}^{-1} \text{hr}^{-1}$, and B vs. C particle size cutoff $M = 196$. The BFV is 9.54×10^{-4} . The initial solvent amount is 11.3 M. The dissociative rate constants are $k_+ = 3.60 \times 10^{-2}$ and $k_- = 7.27 \times 10^4$.

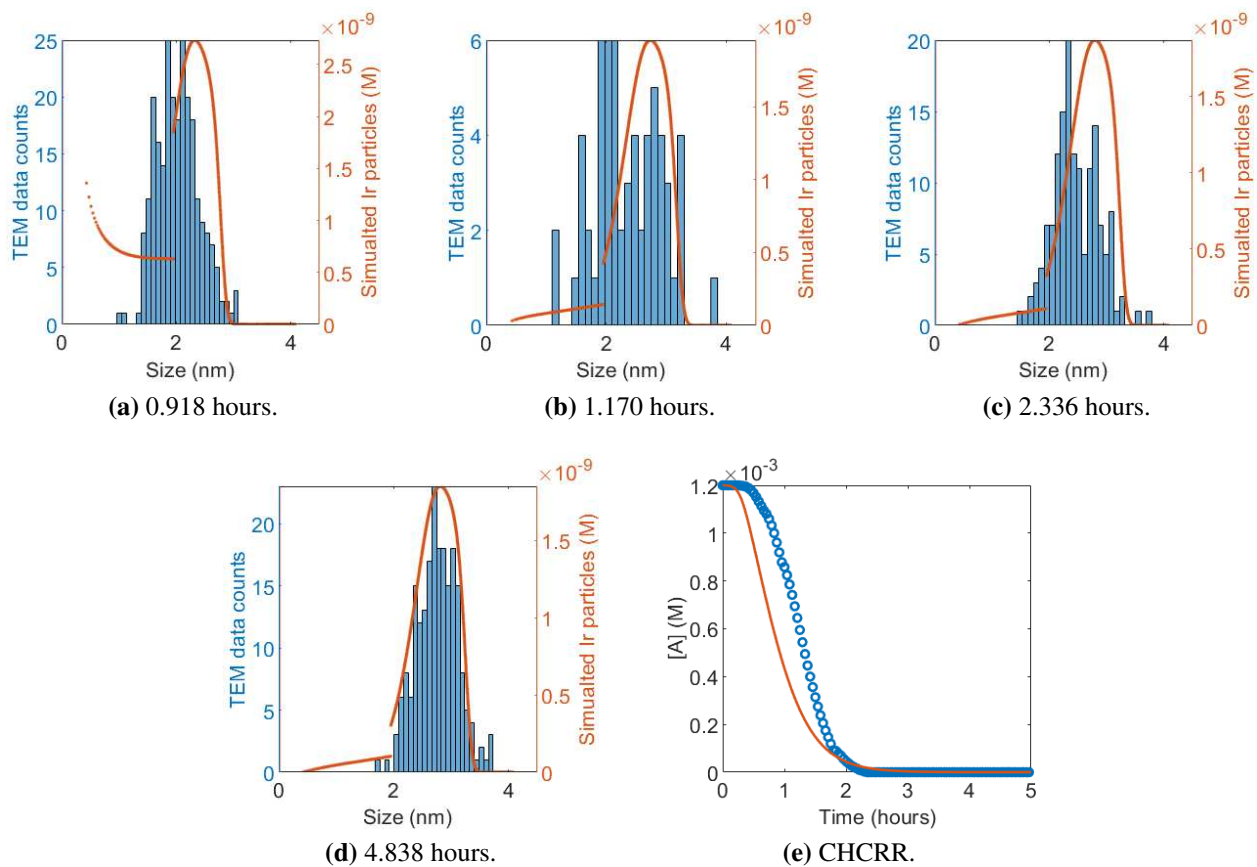


Figure 1.23: Fit to the final histogram using the 3-step mechanism and alternative nucleation. The rate constants produced by the fit are $k_1 = 6.45 \times 10^4 \text{M}^{-2} \text{hr}^{-1}$, $k_2 = 1.63 \times 10^4 \text{M}^{-1} \text{hr}^{-1}$, $k_3 = 5.57 \times 10^3 \text{M}^{-1} \text{hr}^{-1}$, and B vs. C particle size cutoff $M = 274$. The BFV is 2.93×10^1 . The initial solvent amount is 11.3 M. The dissociative rate constants are $k_+ = 3.60 \times 10^{-2}$ and $k_- = 7.27 \times 10^4$.

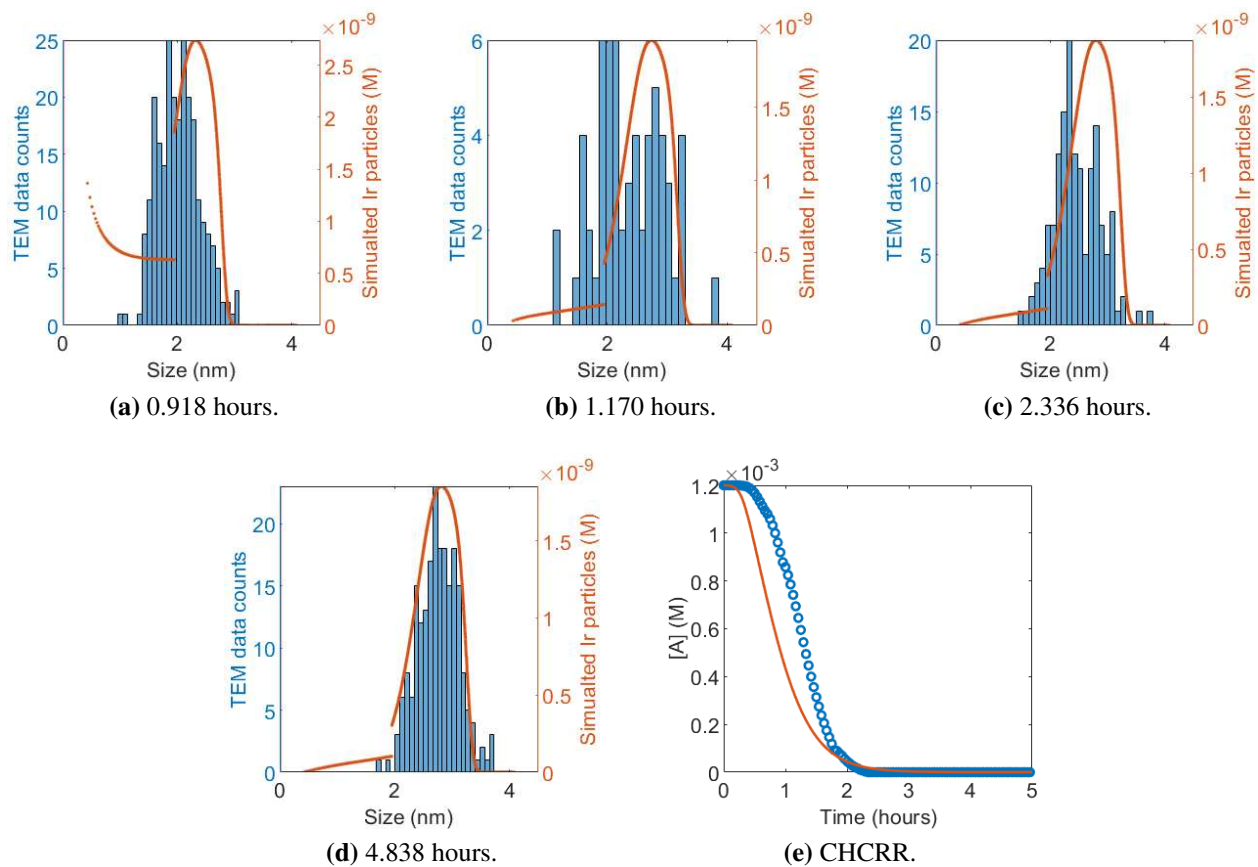
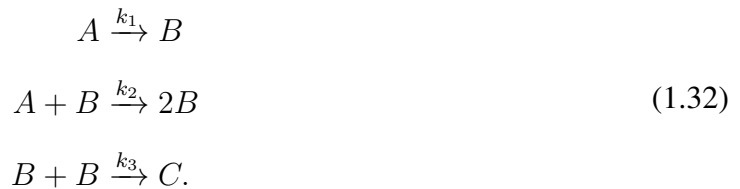


Figure 1.24: Fit to the final histogram using the 3-step mechanism and alternative nucleation using the complete polling option in patternsearch. The rate constants produced by the fit are $k_1 = 6.45 \times 10^4 \text{M}^{-2} \text{hr}^{-1}$, $k_2 = 1.63 \times 10^4 \text{M}^{-1} \text{hr}^{-1}$, $k_3 = 5.56 \times 10^3 \text{M}^{-1} \text{hr}^{-1}$, and B vs. C particle size cutoff $M = 274$. The BFV is 2.93×10^1 . The initial solvent amount is 11.3 M. The dissociative rate constants are $k_+ = 3.60 \times 10^{-2}$ and $k_- = 7.27 \times 10^4$.

Most of the model fits to the TEM histogram measurements result in reporter reaction curves with short induction times. It was noticed from changing the forward and backward K_{diss} values while keeping the same ratio could result in no qualitative change in PSDs, but a precursor concentration that better followed the reporter reaction. This led to an attempt to fit for these k_+ and k_- values. The fit was performed by fixing the k_1 , k_2 , and k_3 values from Figure 1.23 for the alternative termolecular 3-step model and minimizing the CHCRR objective function by changing k_+ then deriving the appropriate k_- value from K_{diss} . The results from this fit are seen in Figure 1.25. With the rate constants for nucleation and growth fixed, changing the K_{diss} constants makes the simulated precursor curve match very well to the reporter reaction, especially during the first half of the reaction. The PSDs maintain overall shapes that are adequate matches to the TEM data, but have a higher polydispersity than before, and "lean back" towards the "small" particles. Better experimental knowledge of the concentration of precursor A , or fitting the simulated precursor curve only the first third or half of the CHCRR curve is worth exploring.

3_β -Step Mechanism

The 4-step mechanism (1.18) is capable of obtaining qualitatively correct PSDs by adding agglomeration to, and splitting the monomer growth step of, the 2-step mechanism (1.13). The 3-step (1.22) is also capable of qualitatively correct PSDs while having only size dependent split monomer growth with no agglomeration. It is then important to check the mechanism which has agglomeration but no size dependence for monomer addition. This mechanism we call the 3_β -step and is given by the pseudoelementary steps



We forgo presentation of the ODE systems as they can easily be created from slight modifications to (1.19) and (1.20). This mechanism needs to have size independent monomer addition across all

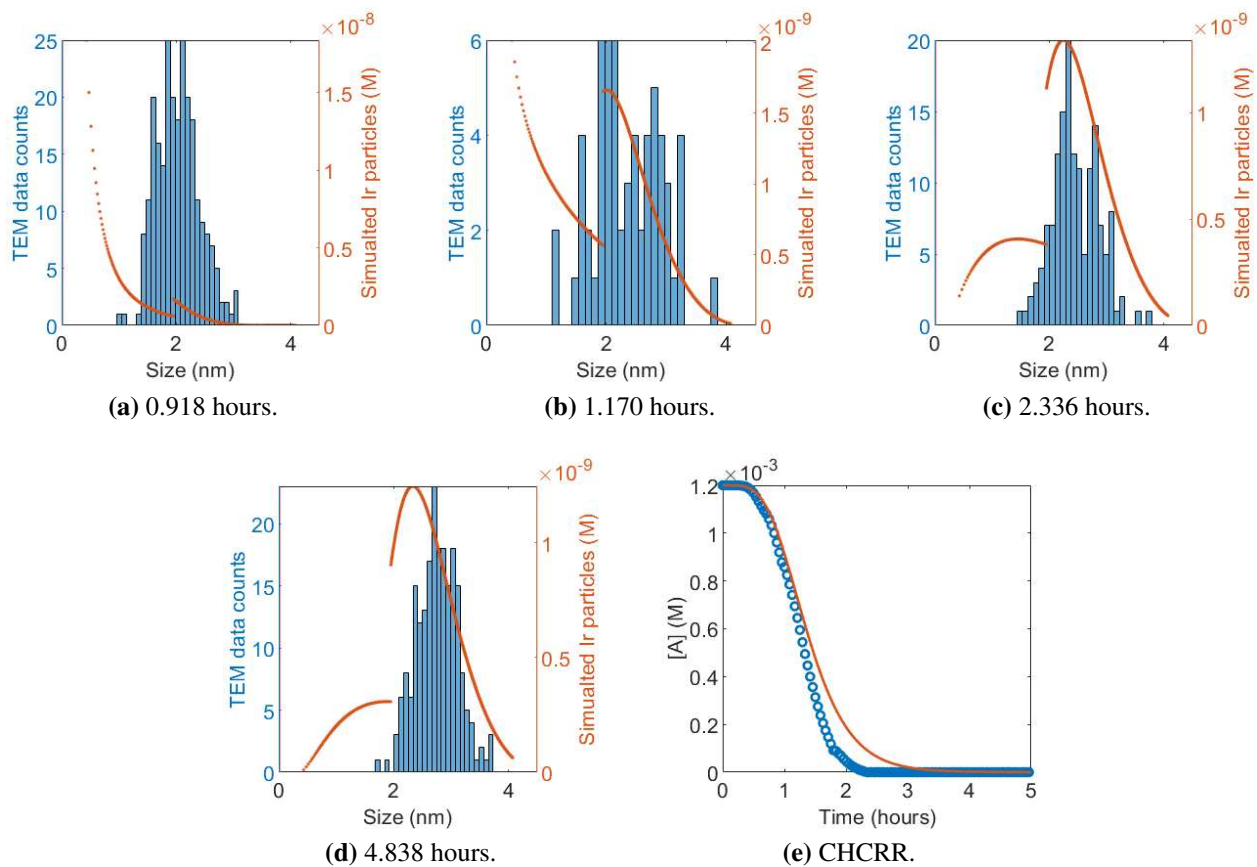


Figure 1.25: Fit to the final histogram using the 3-step mechanism and alternative nucleation using the complete polling option in `patternsearch` and optimizing over K_{diss} . The rate constants produced by the fit are $k_1 = 6.45 \times 10^4 \text{M}^{-2}\text{hr}^{-1}$, $k_2 = 1.63 \times 10^4 \text{M}^{-1}\text{hr}^{-1}$, $k_3 = 5.57 \times 10^3 \text{M}^{-1}\text{hr}^{-1}$, and B vs. C particle size cutoff $M = 274$. The BFV is 7.87×10^{-4} . The initial solvent amount is 11.3 M. The dissociative rate constants are $k_+ = 2.09 \times 10^{-3}$ and $k_- = 4.18 \times 10^3$.

sizes of particles and a "small"- "small" agglomeration step so as to properly isolate the differences between the 2, 3, and 4-step mechanisms. In this regard, the B species in (1.32) plays double duty since in $A + B$ it refers to all sizes, while in $B + B$ it refers only to "small" sizes. In effect, what we have is (1.18) with $k_2 = k_4$.

Fitting (1.32) to the CHCRR curve gives a decent fit as seen in Figure 1.26. The accompanying PSDs are similar to those in Figure 1.10 for the 2-step mechanism. The small-large particle cutoff is very small which means that for all but the smallest 0.48 percent of particles we essentially have the behavior of the 2-step mechanism so the similarities between the PSDs produced by the 3_β -step and the 2-step fits is unsurprising.

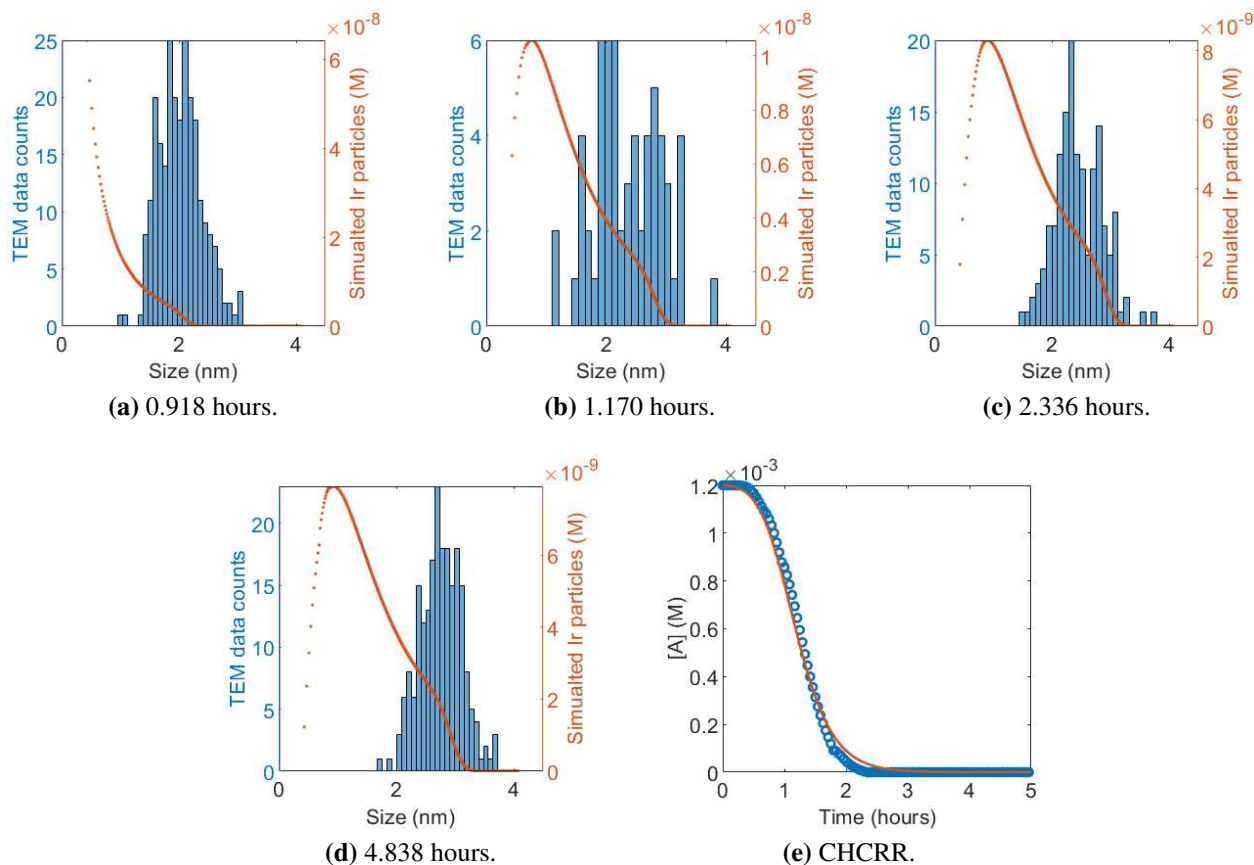


Figure 1.26: Fit to the final histogram using the 3_β -step mechanism using the complete polling option in patternsearch. The rate constants produced by the fit are $k_1 = 2.33 \times 10^3 \text{M}^{-2} \text{hr}^{-1}$, $k_2 = 4.99 \times 10^3 \text{M}^{-1} \text{hr}^{-1}$, $k_3 = 2.00 \times 10^3 \text{M}^{-1} \text{hr}^{-1}$, and B vs. C particle size cutoff $M = 12$. The BFV is 3.23×10^{-4} . The initial solvent amount is 11.3 M.

Fitting (1.32) to the fourth TEM histogram results in a trimodal PSD with very a precursor concentration that is a very poor fit to the reporter reaction which can be seen in Figure 1.27. The rapid use of the precursor is explained in the PSDs by how many large particles are already formed at the first time of 0.918 hours. Since the precursor rapidly becomes depleted both the nucleation and monomer addition steps stop very early. The first bump of the wide part of the distribution is caused by the sizes of particles that form from the $B + B$ agglomeration step. These particles are then unable to grow since there is no remaining monomer.

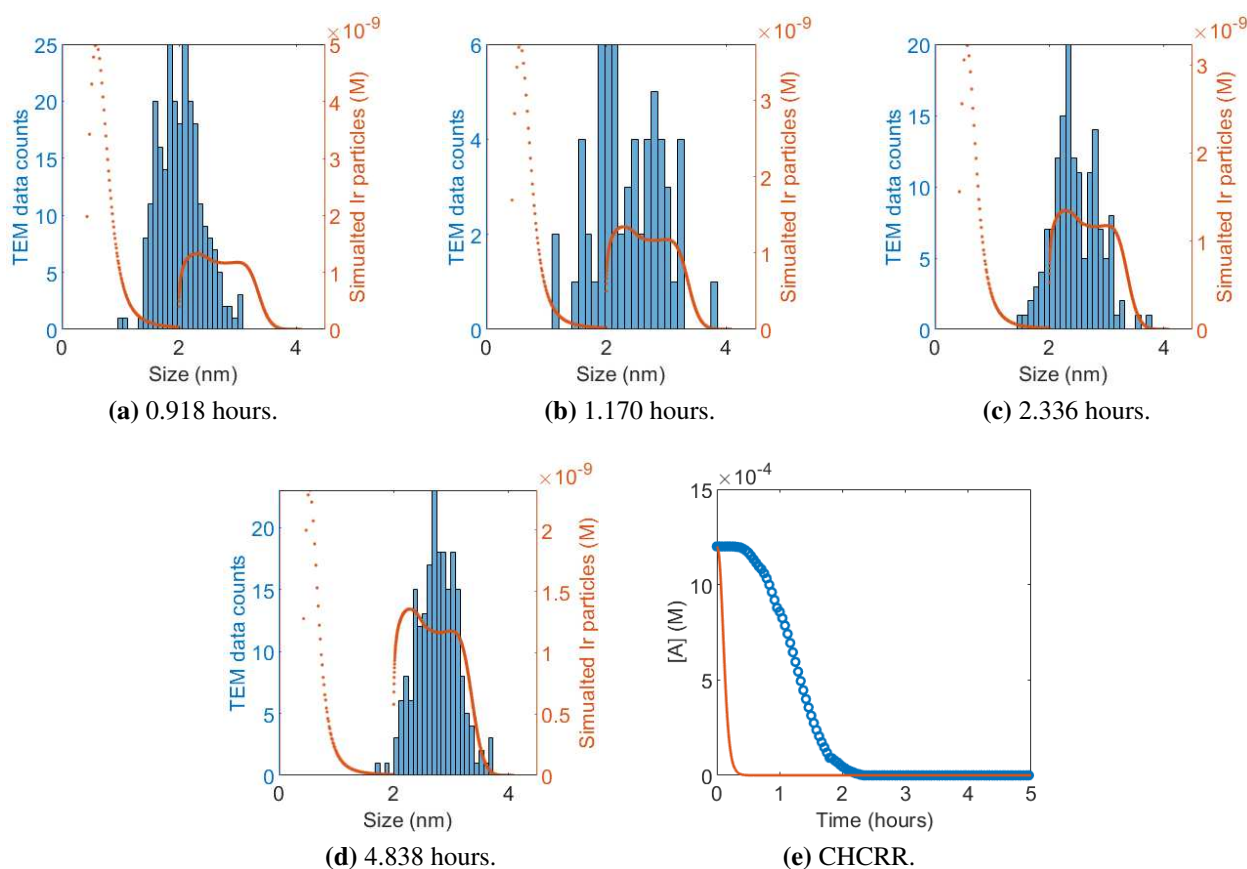


Figure 1.27: Fit to the final histogram using the 3β -step mechanism using the complete polling option in patternsearch. The rate constants produced by the fit are $k_1 = 6.50 \times 10^4 \text{M}^{-2}\text{hr}^{-1}$, $k_2 = 4.00 \times 10^4 \text{M}^{-1}\text{hr}^{-1}$, $k_3 = 9.87 \times 10^3 \text{M}^{-1}\text{hr}^{-1}$, and B vs. C particle size cutoff $M = 296$. The BFV is 1.56×10^2 . The initial solvent amount is 11.3 M.

1.4.7 Five-Step Mechanism

A proposed 5-step mechanism consists of the 4-step mechanism (1.18) with the additional step of "small"- "large" agglomeration $B + C \rightarrow C$ given by the steps



which consist of nucleation, monomer growth, and agglomeration. The monomer growth and agglomeration steps are size-dependent. A monomer is added to "small" particles and "large" particles at different rates. Similarly, agglomeration has "small" particles joining with other "small" particles and "large" particles at different rates. There is no "large"- "large" agglomeration in this mechanism. The lack of this is plausible given the reasoning behind Table 1.1. The effect of having all particles participate in agglomeration takes its toll numerically in the form of significantly increased computation times over the other mechanisms. Some inconclusive simulations with ad hoc parameter choices were run, but a systematic `patternsearch` fit was not performed due to CPU time limitations. It is likely that this mechanism is perfectly capable of producing PSDs that are accurate matches to the experimental data based on the results from the 3-step and 4-step mechanisms.

1.5 Comparison of Results

A table of CHCRR curves and the final measured histogram for various tested mechanisms fit to the CHCRR curve is given below in Figure 1.28 and to the final histogram in Figure 1.29. The CHCRR fits summary clearly shows how each mechanism is able to match the reporter reaction, but that they are not simultaneously able to produce qualitatively accurate PSDs.

The histogram fitting comparison shows that the 4-step and 3-step mechanisms are able to reproduce PSDs with similar polydispersity and mean as the TEM data while the 2-step cannot. These simulations all result in similar CHCRR curves which have a shorter-than-measured induction period compared to the reporter reaction.

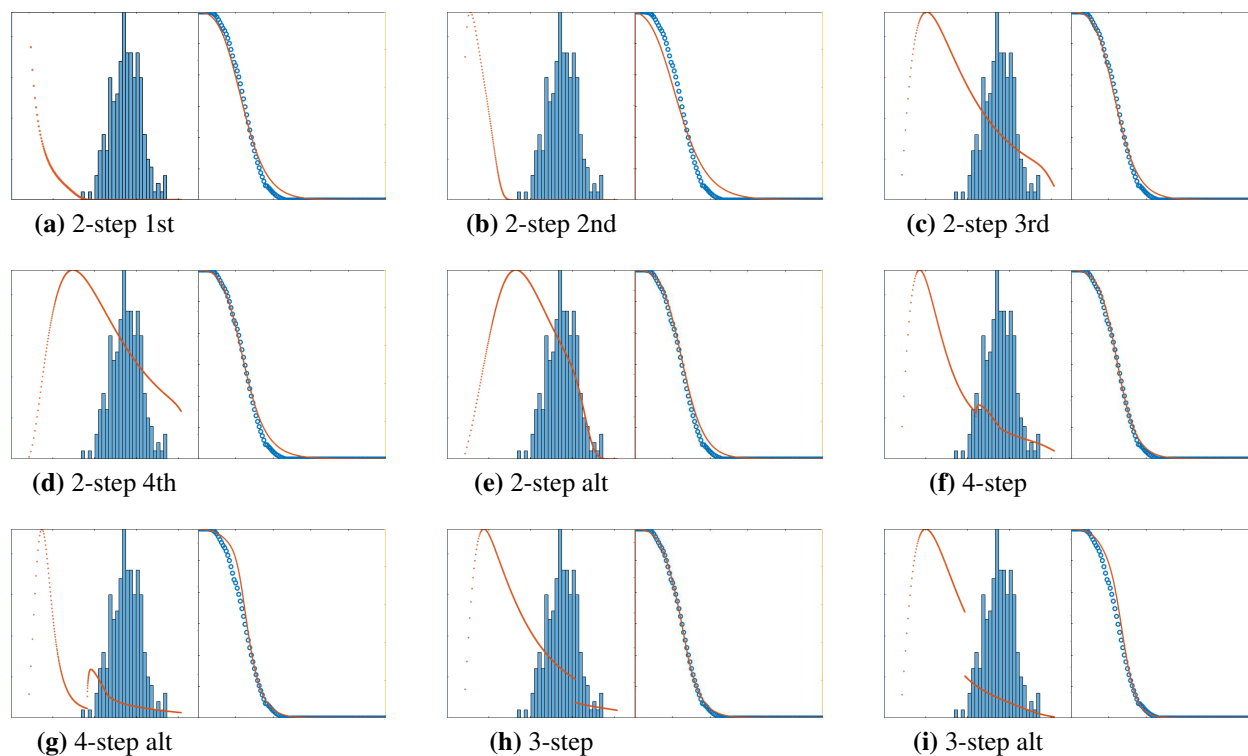


Figure 1.28: A side-by-side comparison of the fourth and final histogram and CHCRR curves for some of tested models fit to the CHCRR curve. See previous figures for appropriate axes labels. This demonstrates that regardless of the mechanism or model fitting to the reporter reaction is easily accomplished. It also demonstrates that just knowing *when* precursor is consumed via the reporter reaction does nothing to show *where* it goes in the size distributions.

1.6 Comparison of Growth and Nucleation Rates

Figure 1.30 details how the number of particles, nucleation rate, and growth rate change over time for the 3-step mechanism with alternative nucleation (1.30). The nucleation and growth rates are the nucleation and growth terms in the dn_1/dt equation in (1.25).

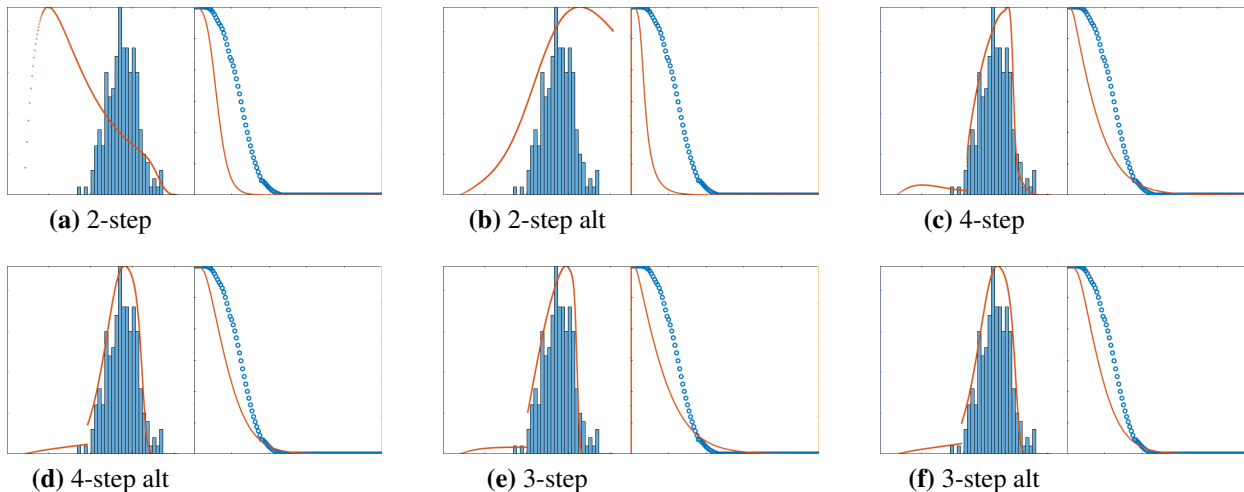


Figure 1.29: A side-by-side comparison of the fourth and final histogram and CHCRR curves for some of tested models fit to the final histogram. See previous figures for appropriate axes labels. Similar CHCRR curves between fits with different PSDs shows again that knowing *when* the precursor is used does not say *where* it is used. The 4-step and 3-step models produce very similar and well fitting PSDs. The two models both have smaller particles growing faster than larger particles.

The number of particles looks to plateau, but is monotonically increasing when looking at the derivative. The increase in the number of particles reiterates the continuous nucleation of the model. Interestingly, the nucleation rate appears to be burst-like, but this is not the case. The mechanism and model both implement continuous nucleation. Nucleation and growth have significant overlap and are not completely separated in time. Continuous nucleation can appear burst-like.

1.7 Open Flow Reactor Simulations

The first ODE in the best performing 3-step model in System (1.25) or (1.31) can be modified to simulate an open flow chemical reactor in which precursor is continuously fed into the system by adding a constant term to the $\frac{dn_1}{dt}$ equation. Open reactors [26, 64] are used in chemistry and the study of nanoparticle formation, so it is important to test the mechanisms ability to produce realistic PSDs in this scenario. The available TEM data was produced in a closed batch with no incoming source of precursor after the initial seeding, so there is no appropriate data to compare the simulations to. However, we can see how the PSDs are affected by a source term in the model.

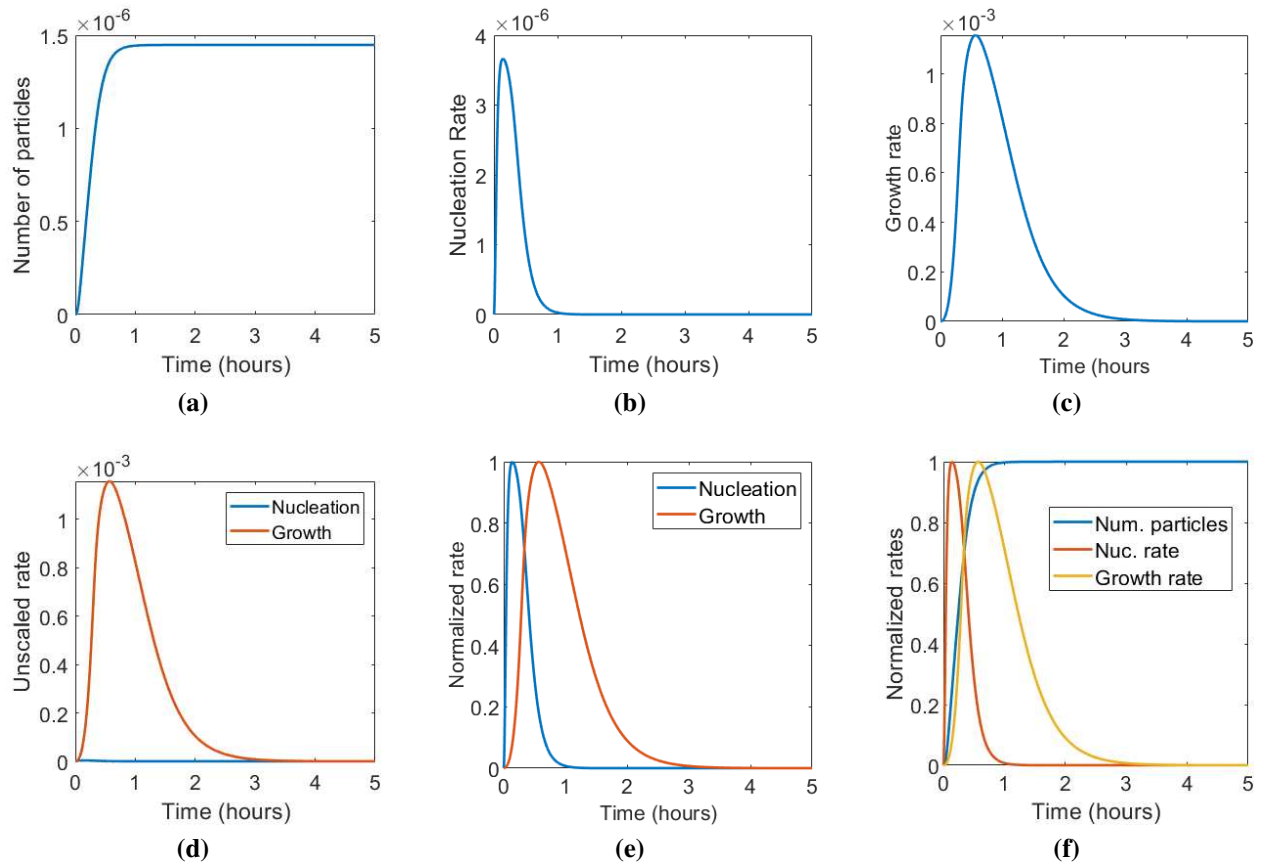


Figure 1.30: The number of particles a) increases throughout the reaction, but the effective nucleation rate b) appears burst-like. The growth rate is seen in c). The unscaled nucleation and growth rates are in d) and show how much larger the growth rate is. The unscaled versions are in e) where their changes over time can be compared. The nucleation and growth rates have significant overlap and are not separated in time. Normalized number of particles and the two rates are compared in f).

Figure 1.31 show the simulation results of using the 3-step model with alternative nucleation where the dynamical equation for the precursor has a constant source term. The source term is such that after 5 hours the total concentration of monomers in all particles as increased by around one mM. This constant increase in monomer concentration is shown in the figure in addition to PSDs at now familiar times. The concentration $[A]$, the sum of both the A and A_{solv} species, is also given. The simulation shows an increase in $[A]$ at early times due to the source term, and then similar behavior to the closed experiment once growth becomes dominant. The inflow of precursor is not high enough here so as to overwhelm the systems ability to consume it. Experimental data in an open flow system is needed to definitively validate this simulation. However, the simulation seems to behave in an expected manner and should be able to predict such an experiment.

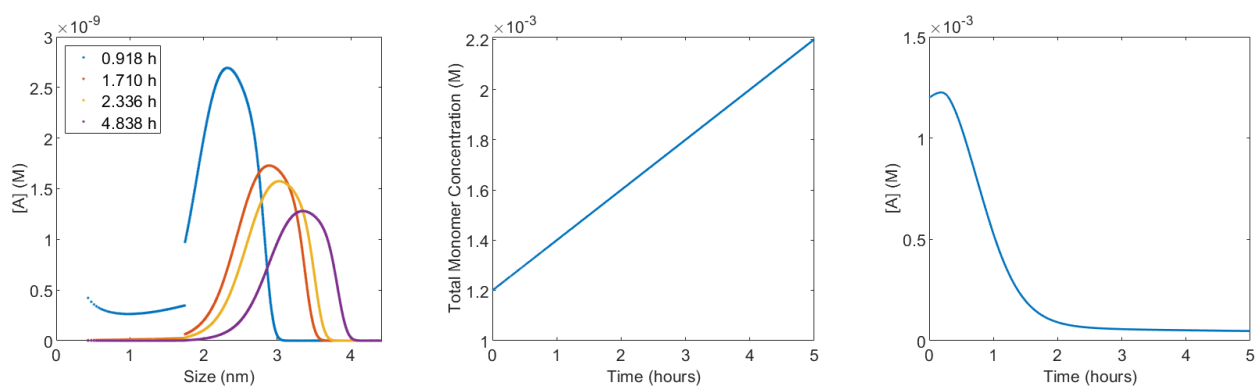


Figure 1.31: Simulation of an open flow reactor with a constant source of precursor A such that the total monomer concentration increased by approximately 1mM after 5 hours. PSDs are shown at the times given, but there is not experimental data to match to. The simulations were done with the 3-step mechanism with alternative termolecular nucleation using the best values obtained from histogram fitting with the closed system TEM data.

1.8 Extension to Larger Systems via Binning

The iridium system modeled via ME-PBM in this dissertation is a relatively small system with a maximum particle size of 2500 leading to ODE systems of 2500 equations. For larger particle systems with maximum particle sizes potentially in the millions, it is not feasible to use a single equation for each size.

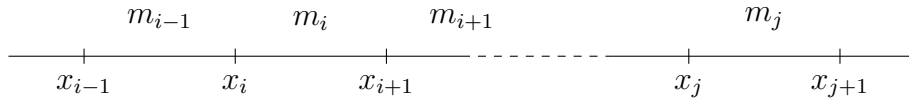
The standard monomer ODEs for the 2-step mechanism are given in (1.16). These have a single equation for each individual particle size which becomes prohibitive to compute when the maximum particle size becomes large. To overcome this, we will bin multiple sizes together to reduce the overall number of equations. This binning or grouping is usually done by

$$\frac{d}{dt} \int_{x_i}^{x_j} m(x, t) dx = f(x_i, t) - f(x_j, t) \quad (1.34)$$

where the change of mass over an interval is equal to the flux in from the left and right boundaries and the particle size x is continuous. The number of monomers is integral and not continuous and is being studied on a scale where it is not necessarily require. So, to keep things discrete we can write

$$\frac{d}{dt} \int_{x_i}^{x_{j+1}} m(x, t) dx = \frac{d}{dt} \left(\sum_{k=i}^j m_k \right) = \frac{dm_i}{dt} + \frac{dm_{i+1}}{dt} + \dots + \frac{dm_j}{dt}, \quad (1.35)$$

where the indices are arranged as



Equation (1.16) can now be used in the right-hand side of (1.35). For example with the nucleation order $\omega = 3$ and using bin groups of size 3 starting with $m_{\omega+1}$ we get for the first bin

$$\begin{aligned} \frac{d}{dt} \int_{x_4}^{x_7} m(x, t) dx &= \frac{d}{dt} \left(\sum_{k=4}^6 m_k \right) = \frac{dm_4}{dt} + \frac{dm_5}{dt} + \dots + \frac{dm_6}{dt} \\ &= k_2 m_1 (4b_3 - 4b_4 + 5b_4 - 5b_5 + 6b_5 - 6b_6) \\ &= k_2 m_1 (4b_3 + b_4 + b_5 - 6b_6). \end{aligned} \quad (1.36)$$

The form for a bin over an arbitrary interval is then given by

$$\frac{d}{dt} \int_{x_i}^{x_{j+1}} m(x, t) dx = \frac{dM_{i,j}}{dt} = k_2 m_1 \left(i b_{i-1} + \sum_{k=i}^{j-1} b_k - j b_j \right), \quad (1.37)$$

where the interval monomer concentrations are denoted $M_{i,j}$. The right-hand side of (1.37) is still in terms of the individual monomer species. The leftmost term is the gain from growth where i monomers are gained from a monomer combining with with m_{i-1} . The middle term is the gain from particles that stay in the bin. The coefficient on these terms is 1 from the additional precursor monomer. Finally, the rightmost term is loss from growth where we lose the largest size in the bin.

We are concerned with the total number of monomers in a given bin $M_{i,j} = \sum_{k=i}^j m_k$. If we assume an odd number of monomer species in each bin with size β we have that $M_{i,j} \approx \beta m_{(i+j)/2}$. We also say that $R_{i,j} = r_{(i+j)/2}$. The number of bindable spots in each bin is then $B_{i,j} = \beta r_{(i+j)/2} m_{(i+j)/2} = \beta b_{(i+j)/2} = R_{i,j} M_{i,j}$.

Let us also assume that every species in a bin is approximately the average size species in the bin so $m_i \approx m_{i+1} \approx \dots \approx m_j \approx m_{(i+j)/2}$. We can now approximate (1.37) and obtain

$$\begin{aligned} \frac{dM_{i,j}}{dt} &\approx \frac{k_2 m_1}{\beta} \left(i B_{i-\beta, j-\beta} + (\beta - 1) B_{i,j} - j B_{i,j} \right) \\ &= \frac{k_2 M_1}{\beta} \left(i R_{i-\beta, j-\beta} M_{i-\beta, j-\beta} + (\beta - 1 - j) R_{i,j} M_{i,j} \right). \end{aligned} \quad (1.38)$$

Combining this with the equations for the precursor and nucleus we arrive at the system

$$\begin{aligned} \frac{dM_1}{dt} &= -\omega k_1 M_1^\omega - k_2 M_1 B_\omega - k_2 M_1 \sum_{i,j} B_{i,j} \\ \frac{dM_\omega}{dt} &= \omega k_1 M_1^\omega - \omega k_2 M_1 B_\omega \\ \frac{dM_{i,j}}{dt} &= \frac{k_2 M_1}{\beta} \left(i B_{i-\beta, j-\beta} + (\beta - 1) B_{i,j} - j B_{i,j} \right). \end{aligned} \quad (1.39)$$

It is important to note that β is a function of the bin it is referring to. The precursor and nucleus bins have a size $\beta = 1$ which means that the first $M_{i,j}$ equation bin can not have the $1/\beta$ factored out since the first term refers to the previous nucleus bin which a different size. The number of particles in a bin is given by the total number of monomers divided by the average particle size or $N_{i,j} = \frac{1}{\alpha_{i,j}} \sum_{k=i}^j m_k = \frac{1}{\alpha_{i,j}} M_{i,j}$ where the average size in a bin $\alpha_{i,j} = \frac{i+j}{2}$. This in (1.38) gives

$$\alpha_{i,j} \frac{dN_{i,j}}{dt} = \frac{k_2 N_1}{\beta} \left(i \alpha_{i-\beta, j-\beta} R_{i-\beta, j-\beta} N_{i-\beta, j-\beta} + \alpha_{i,j} (\beta - 1 - j) R_{i,j} N_{i,j} \right), \quad (1.40)$$

then

$$\frac{dN_{i,j}}{dt} = \frac{k_2 N_1}{\alpha_{i,j} \beta} \left(i (\alpha_{i,j} - \beta) R_{i-\beta, j-\beta} N_{i-\beta, j-\beta} + \alpha_{i,j} (\beta - 1 - j) R_{i,j} N_{i,j} \right) \quad (1.41)$$

where we have used $\alpha_{i-\beta, j-\beta} = \alpha_{i,j} - \beta$. If we have a bin size of $\beta = 1$ where $i = j$ (1.41)

becomes

$$\frac{dN_j}{dt} = \frac{k_2 N_1}{j} \left(j(j-1) R_{j-1} N_{j-1} - j^2 R_j N_j \right), \quad (1.42)$$

then

$$\frac{dN_j}{dt} = k_2 N_1 \left((j-1) R_{j-1} N_{j-1} - j R_j N_j \right), \quad (1.43)$$

which is identical to the originally derived equations (1.17).

Letting the precursor and nucleus comprise their own bins we can combine their equations from (1.17) with (1.41) giving the system

$$\begin{aligned} \frac{dN_1}{dt} &= -\omega k_1 N_1^\omega - k_2 N_1 \sum_{i=\omega}^{\infty} R_i N_i \\ \frac{dN_\omega}{dt} &= k_1 N_1^\omega - \omega k_2 N_1 R_\omega N_\omega \\ \frac{dN_{i,j}}{dt} &= \frac{k_2 N_1}{\alpha_{i,j} \beta} \left(i (\alpha_{i,j} - \beta) R_{i-\beta, j-\beta} N_{i-\beta, j-\beta} + \alpha_{i,j} (\beta - 1 - j) R_{i,j} N_{i,j} \right), \end{aligned} \quad (1.44)$$

for the binned particle species. This system can be used to simulate populations of particles that contain too many atoms to use a single equation for each size.

1.9 On the Growth Kernel

The growth kernel $\Gamma_{i,j}$ which determines the growth rate between particles sized i and j is difficult to determine. The work in this paper uses a surface-area-dependent, atom-to-atom contact model for the kernel. For example, monomer addition in the 3-step model (1.25) with "small" particles gives

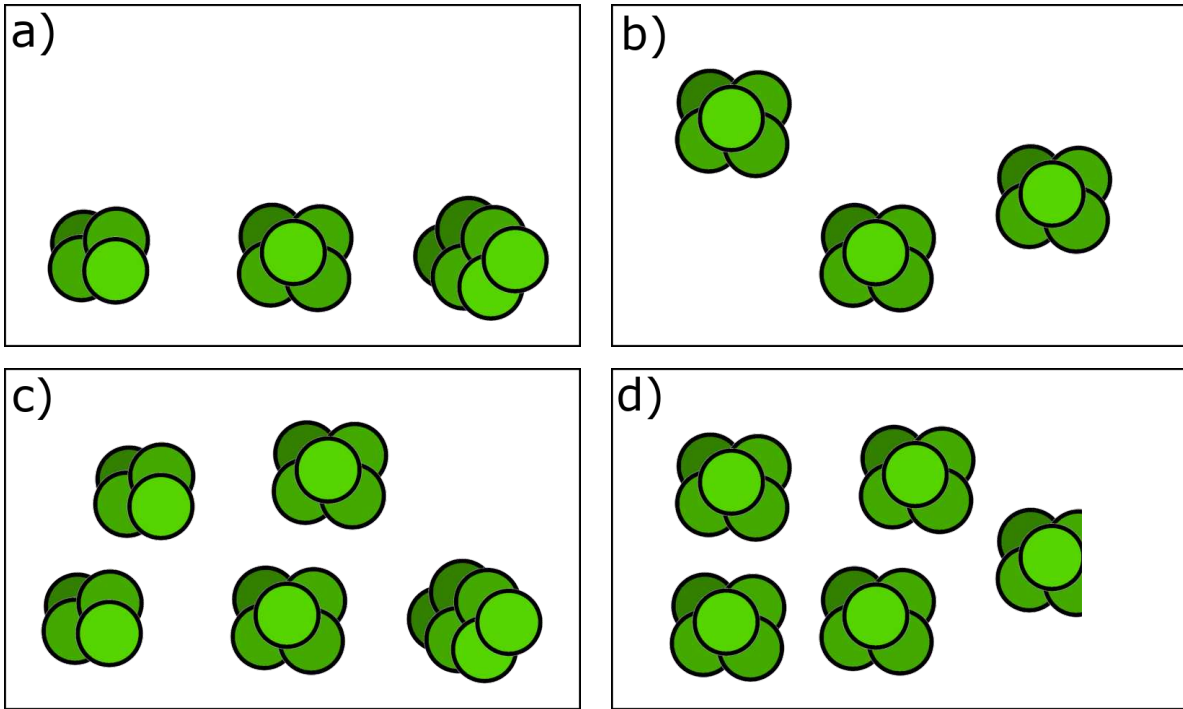


Figure 1.32: Pictorial description of how the binning process works. Each box represents the bin $M_{4,6}$ formed of m_4 , m_5 , and m_6 . In a) there are three particles, one of each size. When we bin these particles we no longer have any knowledge of the individual sizes, we only know the total number of atoms. In this case there are 15 atoms, so we effectively have 3 $N_{4,6}$ particles as demonstrated in b). In c) we have various sizes which do not lead to an integer number of average size particles. The result of binning this case is seen in d) where the 24 total atoms are now 4.8 average sized particles. In each case the total number of precursor atoms is conserved.

$$\Gamma_{1,j} = \begin{cases} k_2 j r_j, & j \leq M \\ k_3 j r_j, & j > M. \end{cases} \quad (1.45)$$

while the kernel in the 2-step model (1.17) is

$$\Gamma_{1,j} = k_2 j r_j, \quad \forall j. \quad (1.46)$$

Recall that $r(j) = 2.677j^{-7.2}/j$ which is the number of surface monomers N_S divided by the total number of monomers N_Σ where N_S is from [57]. The above kernels then are just a rate constant times the number of surface atoms $k_i N_S$. While the ratio of surface atoms to total atoms N_S/N_Σ is a decreasing function of size, N_S is obviously increasing. In Figure 1.33 we see the effect of the step function kernel in the 3-step mechanism compared to two 2-step mechanism kernels. From this figure, we see that the conclusion of large particles needing to grow more slowly than small ones should really be interpreted as *the binding sites on large particles are less reactive, and the binding sites on small particles are more reactive, compared to an increased reactivity just due to increased particle size*. A large particle has more binding sites which makes reactivity increase with size. But, something needs to dampen the overall ability of each site to grow.

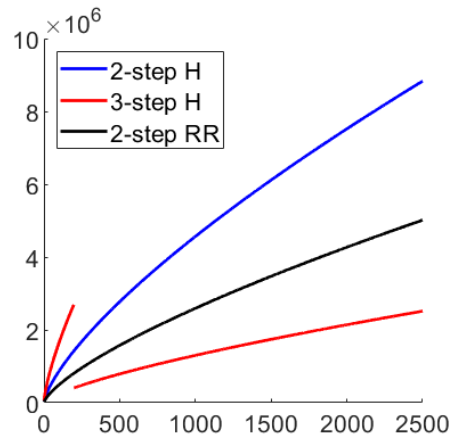


Figure 1.33: The growth kernels (1.45) and (1.46) for the 2-step histogram fit (blue), 3-step histogram fit (red), and 2-step reporter reaction fit (black) with rate constants taken from Table 1.3. The increased reactivity of the smallest particles and decreased reactivity of the larger ones is critical to recreating accurate PSDs.

There has been some work in finding analytical solutions for the continuous version of Smoluchowski's equation with the constant, additive, and multiplicative growth kernels $\Gamma_{i,j} = 2$, $i + j$, and ij [44,45], and recently for the 2-step model with 2nd-order nucleation with rate constants proportional to particle mass [65]. A typically used kernel for two spherical particles is proportional to $(r+R)(1/r+1/R)$ which is then $(1+j)(1+1/j) = 2+j+1/j$ for monomer addition. This kernel is approximately given by $\Gamma_{1,j} = kj$ for large particles where k is some constant. The ME-PBM shows that the addition of dust to this system dramatically increases the rate of nucleation.

1.10 Experimental Methods

The ODE system models of the mechanisms in this paper were coded in MATLAB. Due to the inherent stiffness of the solution wave in size space `ode15s` was chosen as the solver. Even using the stiff ode solver, the relative and absolute tolerances needed to be made substantially smaller than the default. These were chosen to be 10^{-13} , but larger values are possible without the creation of unphysical oscillations. No large effort was made to optimize computation time by maximizing the tolerances. These small tolerance values increase the computation time, but this remains under five minutes except in the mostly unstudied five-step mechanism. The two-step mechanism takes around 30 seconds. The simulations were mainly done on a late 2013 MacBook Pro with a 4th generation Intel Core i7 processor at 2.3 Ghz and 16 GB 1600 Mhz DDR3 RAM.

The ODEs are in terms of particle size while the experimental data is grouped into particles of similar diameter in nanometers. To compare the simulations to experiment a conversion function was needed and $d(n) = 0.300082023n^{1/3}$ was picked. This is the result of a fit from measurements taken for particles with a number of atoms between approximately 12 and 300 as provided by chemists. See Figure 1.6. The exponent of $d(n)$ was picked based on volume arguments. Others were also tested but resulted in fits that were both worse looking and had constant terms.

The mechanisms were fit to the data in two ways. The first was minimizing the L^2 -norm difference between the experimental cyclohexane reporter reaction curve and the simulated precursor curve calculated via the `norm` function. The second way was to match the experimental data his-

togram at the fourth time step of 4.838 hours to the simulated population distribution. To compare the simulations to the experimental histograms MATLAB's `histfit` function was used on the TEM data. The result was normalized and compared to the normalized simulation distribution. Both of the distributions were interpolated onto the same domain for comparison and the L^1 -norm of their difference was minimized. The L^1 norm was computed via the `trapz` function. The minimization was done via the function `patternsearch`.

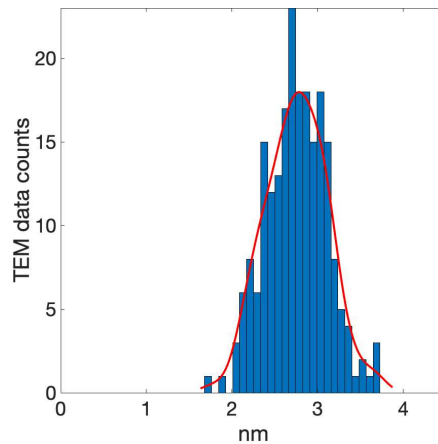


Figure 1.34: Red curve from MATLAB's `histfit` function together with TEM data histogram. The red curve is interpolated and normalized, and compared to the normalized simulated distribution

1.10.1 The Pattern Search Algorithm

The pattern search algorithm implemented by MATLAB in the function `patternsearch` was chosen since it is capable of bounded, multivariate optimization. It works by starting at an initial point and then polling a potential $2N$ number of points where N is the number of parameters being minimized over. Each of these points is the same distance away from the starting point but in $2N$ orthogonal directions creating a mesh. If a poll is successful whereby the algorithm finds a point with a smaller objective function value it will move to this better point and create a new, larger search mesh. If the poll is unsuccessful it will refine the mesh. The default polling behavior is to move to the first better point. Complete polling may be enabled which searches all points along the mesh and picks the best one before going to the next iteration. Using complete polling can help

minimize objective function that have many local minima at the expense of more function calls. A few iterations of the standard and complete polling behaviors can be seen in Figure 1.35.

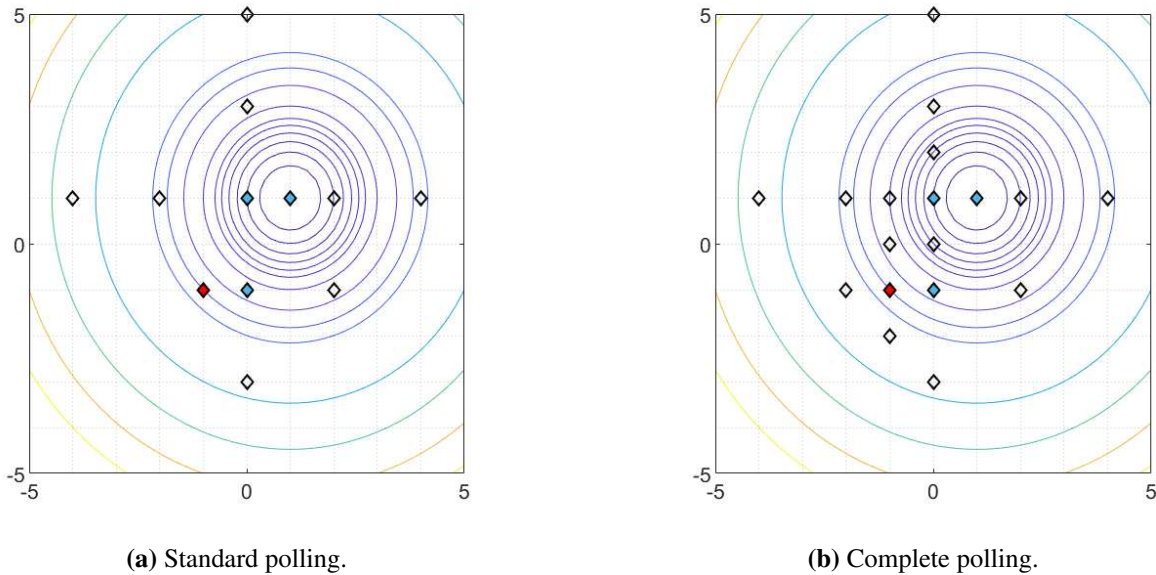
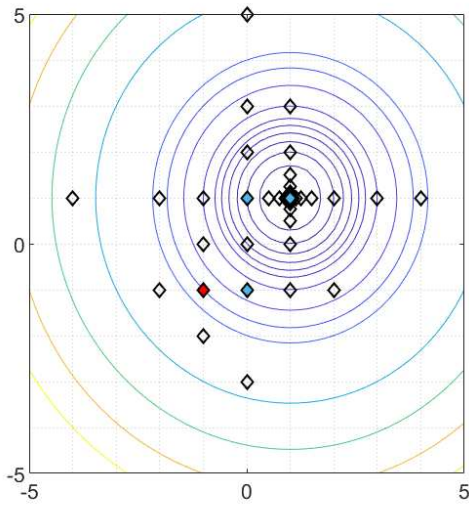


Figure 1.35: Different polling methods for the pattern search algorithm. The default behavior (a) which sequentially searches around the point and moves on when the first better point is found, and (b) complete polling where each potential point is polled before picked the best. Red-filled diamonds are starting locations, blue-filled are successful polls, and unfilled are unsuccessful polls.

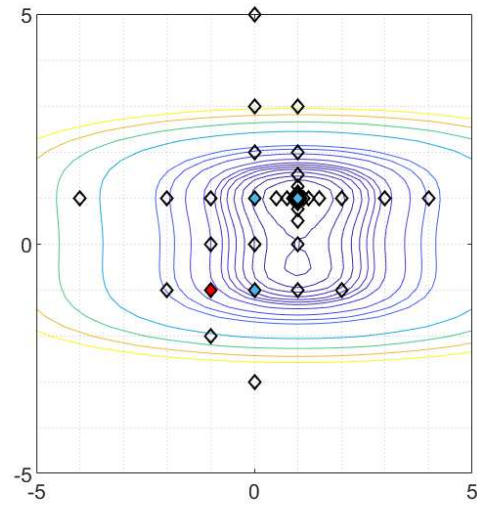
Further examples of the pattern search algorithm polling process can be seen in Figure 1.36 with functions $f_1(x, y) = (x-1)^2 + (y-1)^2$ with one minimum, $f_2(x, y) = (x-1)^2 + y^2(y^2 - \frac{2}{3}y - 1)$ one local and one global minima, and the Rosenbrock function $f_3(x, y) = (1-x)^2 + 100(y-x^2)^2$ with global minimum at (1, 1).

1.10.2 The Objective Function for Pattern Search

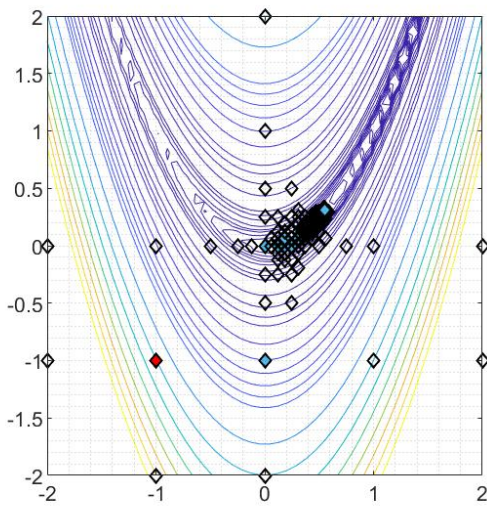
There were two different objective functions used to get the rate constants above. The first was for fitting to the CHCRR curve and the second was for fitting to the fourth and final particle size histogram. The former was a very straightforward use of the L^2 norm via MATLAB's built in `norm` function. The latter was more complicated.



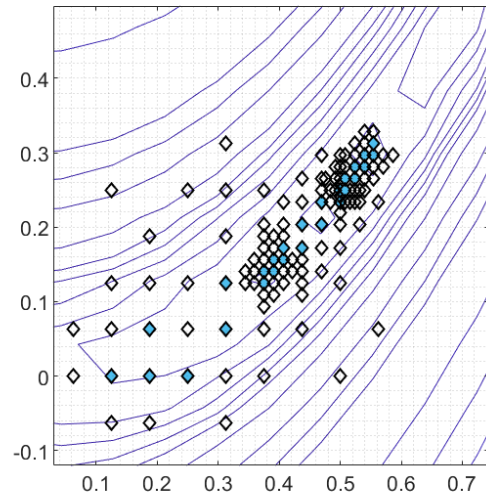
(a) $f_1(x, y)$.



(b) $f_2(x, y)$.



(c) $f_3(x, y)$.



(d) $f_3(x, y)$ zoomed in.

Figure 1.36: Illustrative example of the pattern search algorithm polling process. Red-filled diamonds are initial values, blue-filled are successful polling locations, and unfilled are unsuccessful polling locations. (a) $f_1(x, y) = (x - 1)^2 + (y - 1)^2$ with its only minima at $(1, 1)$, (b) $f_2(x, y) = (x - 1)^2 + y^2(y^2 - \frac{2}{3}y - 1)$ with a global minimum at $(1, 1)$ and a local minimum at $(1, -\frac{1}{2})$, (c) the Rosenbrock function $f_3(x, y) = (1 - x)^2 + 100(y - x^2)^2$ with global minimum at $(1, 1)$, and (d) zoomed-in version of (c). The first two functions were run for 20 iterations of `patternsearch` and reached their global minimums, while the Rosenbrock function was run for 60 and failed to converge. All with complete polling.

First, a curve was generated from the histogram using the `histfit` function. Next, this curve and the simulated PSD generated by an ODE system for a mechanism were interpolated onto the same grid via `griddedInterpolant`. Having the data values for each curve on the same grid points was necessary in order to take the norm between them. For this the `trapz` function was used to compute the L^1 difference.

1.11 Summary and Conclusions

The concept of *mechanism-enabled* PBM has been introduced. This is using PBM with an experimentally determined nucleation mechanism together with experimentally determined growth and agglomeration mechanisms. The definition of mechanism here comes from physical-organic chemistry and means a minimal, disproof-based, experimentally determined reaction mechanism which is well supported by, at least, a balance reaction and experimental kinetic studies. Our ME-PBM was implemented via systems of ODEs which allowed for the direct computation of particle size distributions. The simulated PSDs could then be directly compared to experimental size histograms in order to fit rate constants. Mechanistically enabling the ODEs with the experimentally established alternative termolecular nucleation for the $\text{Ir}(0)_n$ nanoparticle system under study improved the histogram fits of each mechanism by yielding lower BFVs and was done with experimentally established nucleation rates.

A previously unknown 3-step mechanism was discovered that is a simple extension of the well established FW 2-step mechanism. This 3-step mechanism has "small" and "large" particles grow by monomer addition at different rates. Under conditions where agglomeration is kinetically noncompetitive particle growth is fundamentally monomer addition. This is the best evidence to date that the $A + B \rightarrow 2B$ autocatalytic pseudoelementary step of the FW 2-step mechanism represents the summation of the individual $A + B_i \rightarrow B_{i+1}$ single monomer addition steps. This is physically expected but previously was not strongly experimentally supported.

There is now compelling evidence that the *continuous nucleation* of the FW 2-step and the new 3-step mechanisms constitute a paradigm shift in the understanding of particle formation in the

69 years since the LaMer model was introduced in 1950. The application of the FW 2-step and new 3-step mechanism is across a wide variety of systems in nature ranging from homogeneous catalyst formation, protein aggregation, solid-state kinetics, dye aggregation, and other areas of nature which show "cooperative", autocatalytic phenomena. These two mechanisms provide slow, continuous nucleation and autocatalytic surface growth as replacements for CNT.

Given the inapplicability of LaMer's model of burst nucleation [73] to the formation of narrow size distributions in strong-bond systems our new insight that *smaller particles grow faster than larger particles* offers an alternative. If the growth of large particles slows down it gives the small particles an opportunity to catch up in size so that the end size distribution is narrow. This result is summarized in Table 1.2 which shows the results of the possible combinations of turning off or leaving on nucleation and growth. Two of the choices are ineffective. The third choice, corresponding to burst nucleation and a separation of the nucleation and growth phases has been the standard assumption for nearly 70 years. We have shown that this long-held belief is not necessary for the production of near-monodispersed populations. The combination of slow, continuous nucleation coupled with a decreasing reactivity with particle size should be valid for any physical system where the final product is a collection of particles and not a bulk metal or complete phase change.

The ME-PBM was possible due to having sufficient experimental data to fit model parameters. Without accurate experimental size distributions, other indirect methods such as the reporter reaction which follows the precursor concentration must be used. However, as we have seen, the sigmoidal decrease of precursor can be quantitatively matched seemingly with any mechanism. The reporter reaction does give helpful insights into the underlying chemical mechanism, but it is inadequate. As an analogy, it is like trying to determine where people live by watching the rate at which they leave a sports stadium. This rate determines how fast they leave, but tells nothing about where they go.

Table 1.3 is given as a reference to easily compare the rate constants between the various fits performed. This table readily shows that the rate constants for "large" particles are an order of

magnitude smaller than those for "small" particles in mechanisms where such a size distinction is made when fitting to the TEM histograms. It also shows that having and using the experimentally correct nucleation mechanism and rates improves the performance of the overall mechanism.

ME-PBM, together with the paradigm shift away from burst nucleation, should be used in any further modeling efforts of systems whose mean particle size limits to a finite value (*e.g.*, for nanoparticles, but not for say bubbles which will coalesce into one large bubble). ME-PBM was used here on a closed system with particle sizes sufficiently small to simulate an equation for each particle size. The binning process described can be used to extend ME-PBM to systems too large to model each particle size individually, and there is evidence that the models are well suited to open flow systems.

Table 1.2: The four possibilities for keeping nucleation or growth on or shutting them off.

Nucleation	Growth	Status
Off	Off	Nothing happens
On	On	Size-broadening
Off	On	LaMer burst nucleation
On	Off	New 3-step

Table 1.3: Table of rate constants and BFVs for each tested mechanism. See original figures for units. Each mechanism capable of producing qualitatively accurate PSDs has larger particles growing an order of magnitude more slowly than smaller particles.

CHCRR fit	k_1	k_2	k_3	k_4	M	BFV
2-step 1st	6.70×10^{-3}	2.52×10^3	.	.	.	3.92×10^{-4}
2-step 2nd	2.30×10^1	1.71×10^3	.	.	.	6.87×10^{-4}
2-step 3rd	9.14×10^2	6.70×10^3	.	.	.	2.48×10^{-4}
2-step 4th	8.61×10^5	6.93×10^3	.	.	.	3.04×10^{-4}
2-step alt	4.80×10^4	6.50×10^3	.	.	.	1.04×10^{-3}
4-step	1.06×10^3	5.61×10^3	5.16×10^3	8.69×10^3	394	3.92×10^{-4}
4_β -step	3.34×10^4	2.86×10^3	1.44×10^2	1.44×10^2	225	2.40×10^{-3}
4-step alt	5.99×10^4	4.21×10^3	6.24×10^2	1.68×10^4	225	9.55×10^{-4}
3-step	9.78×10^2	6.19×10^3	1.57×10^4	.	1068	1.15×10^{-4}
3-step alt	4.96×10^4	4.97×10^3	1.12×10^4	.	196	9.54×10^{-4}
5-step
Histogram fit	k_1	k_2	k_3	k_4	M	BFV
2-step	2.46×10^3	1.18×10^4	.	.	.	3.88×10^2
2-step alt	4.80×10^4	3.99×10^4	.	.	.	2.53×10^2
4-step	2.71×10^3	2.00×10^4	9.36×10^2	3.94×10^3	331	4.63×10^1
4-step alt	6.40×10^4	1.61×10^4	1.20×10^1	5.45×10^3	265	2.96×10^1
3-step	1.95×10^3	2.24×10^4	3.63×10^3	.	308	4.43×10^1
3-step alt	6.45×10^4	1.63×10^4	5.57×10^3	.	274	2.93×10^1
5-step

Chapter 2

Anisotropies in Spatially Extended Systems

This chapter begins with background and an introduction to pattern formation. The methods of linear stability, weakly nonlinear analysis, amplitude and phase equations are discussed. These methods are applied to the complex Ginzburg-Landau equation (CGLE) and an overview of the CGLE is given. A stability and weakly nonlinear analysis of the anisotropic complex Ginzburg-Landau equation (ACGLE) are performed and a set of phase equations are derived. The phase equations are used to recreate solutions to the ACGLE. The effects of the anisotropy are studied by comparing solutions of the CGLE to solutions of the ACGLE, and by using the L^2 energy to create a phase diagram for two different initial conditions of the ACGLE. The linear stability of the ACGLE is numerically verified and uniquely anisotropic solutions are presented.

This work was supported by Colorado State University, revised by National Science Foundation Division of Mathematical Sciences, via NSF grant DMS-1615909 to PI I. Oprea and Co-PIs G. Dangelmayr and P. Shipman.

2.1 Background and Introduction

There are many natural and experimental examples of pattern formation such as sand ripples, animal coats, fish skin, convection rolls, ion bombarded surfaces, snowcups, icebergs, and chemical systems. Two well known pattern forming systems in fluid mechanics are Rayleigh-Bénard convection and Taylor-Couette flow. In Rayleigh-Bénard convection, fluid is placed between two horizontal plates and a temperature gradient is induced between them creating a buoyancy effect. The fluid heated by the bottom plate will rise and cool fluid near the top plate will fall. This will lead to a pattern of vertical rolls as the control parameter is increased. For Taylor-Couette flow, fluid is placed between two vertical cylinders which are each rotated at different velocities creating a velocity gradient between the inside and outside walls. This leads to a complicated phase diagram of possible patterns as a function of the inner and outer Reynolds numbers, a dimensionless

number that relates the fluid's inertial and viscous forces. General overviews of pattern formation and pattern forming systems can be found in [13, 14, 27, 28].

The patterns in these systems form as some control parameter is varied which controls how far the system is from equilibrium. For example, in Rayleigh-Bénard convection the control parameter is the Rayleigh number $R = \alpha d g^3 \Delta t / \nu \kappa$. The Rayleigh number can be varied experimentally by increasing or decreasing the temperature gradient Δt between the top and bottom plates. The other parameters in R relate to gravity, the distance between the plates, and the fluid properties of thermal expansion and diffusivity, and viscosity.

The basic pattern states are stripes, squares, and hexagons. These patterns are linear combinations of one, two, or three Fourier modes respectively, see Figure 2.1. Stripes, also known as rolls, and their traveling wave counterparts, are the easiest to study since there is only one critical wavenumber.

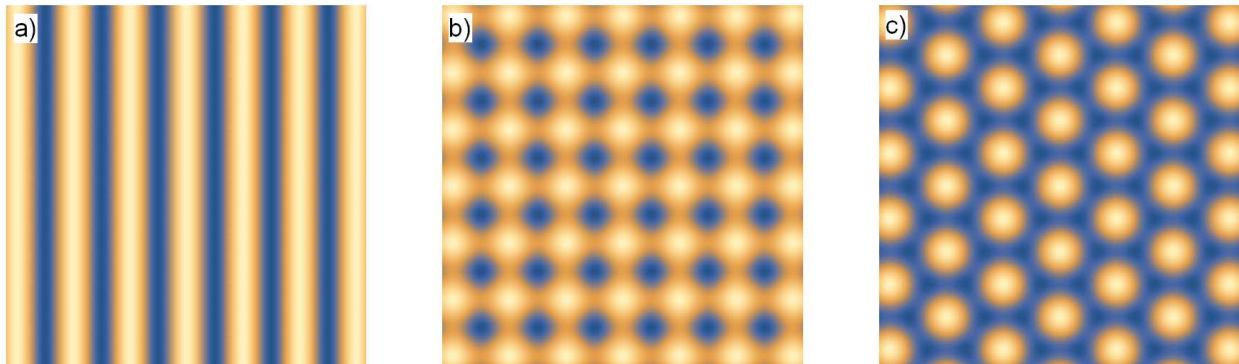


Figure 2.1: Basic patterns of combinations of Fourier modes. a) stripes with one mode, b) squares with two modes, and c) hexagons with three modes.

Different underlying physical systems can produce similar patterns, *e.g.* zebra stripes and sand ripples, for example Figure 2.2. The universality of these patterns can be studied by *amplitude equations*. Amplitude equations describe the slow modulation of the pattern near the threshold of instability. They can be derived via symmetry arguments or through a multiple-scales analysis. The same amplitude equation can be derived from different underlying equations up to some unknown coefficients that determine the length and time scales, and the effect of the nonlinearity. The

underlying equations can be used to determine the correct coefficients of the amplitude equation or they can be scaled out completely. The ability to completely remove the system-dependent coefficients from the equation demonstrates the universality of amplitude equations. The main amplitude equations of concern here are the complex Ginzburg-Landau equation (CGLE) (2.8), and its anisotropic version the ACGLE (2.31).

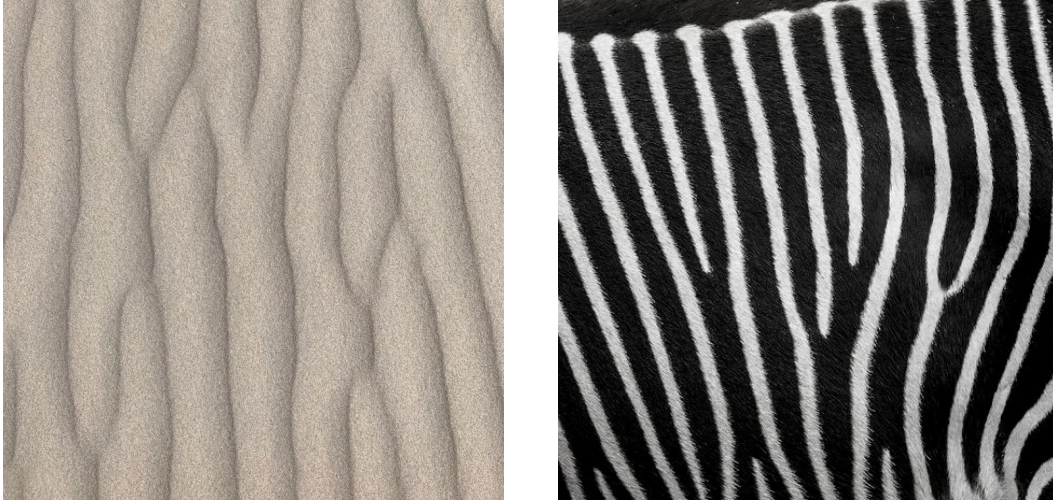


Figure 2.2: Sand ripples and zebra stripes display the same behavior although the physical systems that create the patterns are quite different. Photo credit (sand ripples): Sophia Potoczak Bragdon.

The slow modulations of an amplitude equation yield *phase equations* which describe the extremely slow variation of the phase of the underlying system equations. The phase equation of the CGLE is a fourth-order diffusive equation called the Kuramoto-Sivashinsky (KS) equation [34,60]. The KS equation has been studied in its own right as a model for phenomena such as flame fronts and the leading edge of a viscous fluid flowing down an inclined plane as well as its spatiotemporal chaotic behavior.

When a system consists of more than one spatial dimension it, and thus the amplitude and phase equations, can be either isotropic or anisotropic. Nematic liquid crystals, ion bombardment, surface erosion, and growth are examples of physical scenarios that can be described by anisotropic phase equations. The anisotropic Kuramoto-Sivashinsky (aKS) equation models surface sputter erosion and epitaxial growth [56].

Due to the assumptions used in the derivation of amplitude and phase equations, it is important to consider the regions and circumstances in which they are valid. In the parameter regime where a 1D, periodic traveling wave solution $A(X, T) = A_q e^{i(qX + \omega_q T)}$ is stable to perturbations (Benjamin-Feir or Eckhaus stable) the validity has been looked at in [23, 43]. In the Benjamin-Feir unstable regime validity of the KS phase equation as a description of the phase dynamics for the CLGE has been shown in [67].

2.1.1 Methods

There are certain methods that have become standard when studying pattern-forming systems. Modulation equations for the amplitude or phase are useful to characterize pattern-forming instabilities near the onset of instability. A linear stability analysis can be used to describe the dynamics of perturbations when the control parameter is small such that any nonlinear effects can be ignored. As the control parameter is increased the first nonlinear term will start to balance the linear instability in what is termed the weakly nonlinear regime. A multiple-scales analysis is used to formally derive both amplitude equations from the governing physical equations and phase equations from amplitude equations.

Linear Stability Analysis

As a system is driven out of equilibrium it can become unstable to small perturbations. Patterns initially form when a spatially-uniform solution to the system first becomes unstable to these perturbations. The perturbations are small at this initial point and their dynamics are therefore dominated by the linear terms. As such, we can perform a linear stability analysis to analyze the onset of pattern formation.

By assuming translational invariance one can eliminate the effect of the boundary in the extended directions. This allows the dynamic equations for small perturbations of the homogeneous state to be solved with a single Fourier mode $e^{\sigma_q t + i q \cdot \mathbf{x}}$. Translational invariance can be achieved by assuming either infinite extended directions or by finite extended directions with periodic boundary conditions. Any wave number is possible with infinite boundaries while the periodic boundaries

restricts the wave numbers to integer multiples of $2\pi/L$. Infinite boundaries are also rotationally invariate whereas periodic boundaries are not.

The growth rate $\sigma_q(\mathbf{q})$ of the perturbations is a function of the wave vector \mathbf{q} . The associated uniform state is linearly stable if $\text{Re } \sigma_q < 0$ for all choices of wave vectors \mathbf{q} . As a control parameter is varied the growth rate may become neutrally stable at a critical wave vector \mathbf{q}_c when $\text{Re } \sigma_q = 0$. As the control parameter is further increased, if considering a supercritical bifurcation, there becomes a band of unstable wave vectors around \mathbf{q}_c . The magnitude of the critical wave vector \mathbf{q}_c is used to determine the characteristic length scale and critical frequency that determines the characteristic oscillatory time scale of the perturbations. The characteristic length scale is $2\pi/q_c$, and the critical frequency is $\omega_c = -\text{Im } \sigma_{q_c}$.

The linear growth rate $\text{Re } \sigma_q < 0$ can be classified in three groups called type-I, type-II, and type-III [13, 14]. Each type can be either stationary or oscillatory in nature depending whether ω_c is zero and is designated with either an 's' or 'o' suffix.

The three types are distinguished by the wave number at which the growth rate maximum $\text{Re } \sigma_q$ passes through zero as the control parameter is increased. In a type-I instability the real part of the growth rate becomes positive at a positive critical wave number $q_c > 0$. A band of unstable wave numbers will then develop around q_c and the characteristic length is $2\pi/q_c$. When the control parameter p is equal to its critical value p_c the growth rate can be described by

$$\sigma_q \approx -\frac{\xi_0^2}{\tau_0}(q - q_c)^2, \quad (2.1)$$

where ξ_0 is the coherence length which describes the length over which a local perturbation effects the pattern, and τ_0 is the characteristic time scale.

In a type-II instability $\text{Re } \sigma_q$ is always zero at $q = 0$ which leads to patterns with long characteristic wave lengths when $p > p_c$. This type of instability growth usually occurs when the field obeys a conservation law. When the control parameter is near its critical value

$$\text{Re } \sigma_q \approx D \left(\varepsilon q^2 - \frac{1}{2} \xi_0^2 q^4 \right). \quad (2.2)$$

A type-III instability has a maximum growth rate at $q = 0$. The band of unstable wave numbers that appears around $q = 0$ leads to structure on long length scales. These types of instabilities are often seen as type-III-o oscillatory instabilities. Near the critical control parameter value the growth is described as

$$\text{Re } \sigma_q \approx \frac{1}{\tau_0} [\varepsilon - \xi_0^2 q^2]. \quad (2.3)$$

Pattern forming systems that share an instability type will have similar behavior near onset regardless of the governing physical system or equations. The growth rates for type-I, type-II, and type-III instabilities can be seen in Figure 2.3 each with control parameter values under, at, and above the critical value.

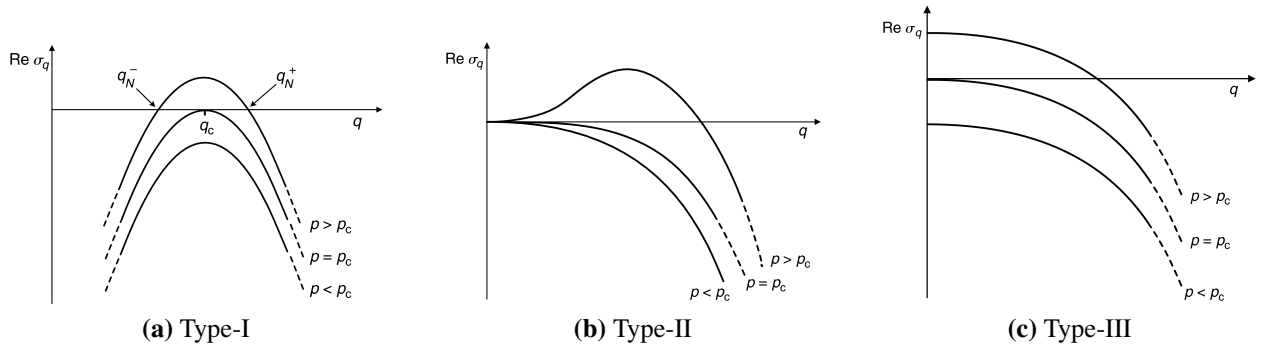


Figure 2.3: Linear instability types according to Cross and Hohenberg [14] with images from [13]. The type-I instability (a) has a nonzero critical wave number and is locally parabolic with an unstable band of wave numbers from q_N^- to q_N^+ . The type-II instability (b) is always zero at $q = 0$ and has a band of instability starting at 0 that grows as p increases. The type-III instability (c) has its maximum at $q = 0$ and is often the oscillatory type-III-o version.

An example of a type-I instability is the Swift-Hohenberg (SH) equation $\partial_t u = ru - (\partial_x^2 + 1)^2 u - u^3$ which has growth rate $\sigma_q^{SH} = r - (q^2 - 1)^2$ where r is the control parameter. The Kuramoto-Sivashinsky (KS) equation $\partial_t u = -\partial_x^2 - \partial_x^4 - \frac{1}{2} |\partial_x u|^2$ is a type-II instability with growth rate $\sigma_q^{KS} = q^2 - q^4$. The version of the KS equation given here has had the control parameter scaled out. The complex Ginzburg-Landau (CGL) equation $\partial_t A = \mu A + (1 + i\alpha) \partial_x A^2 - (1 + i\beta) |A|^2 A$ has a type-III-o instability with growth rate $\text{Re } \sigma_q^{CGL} = \mu - q^2$ with μ as the control parameter. These growth rates can be seen in Figure 2.4.

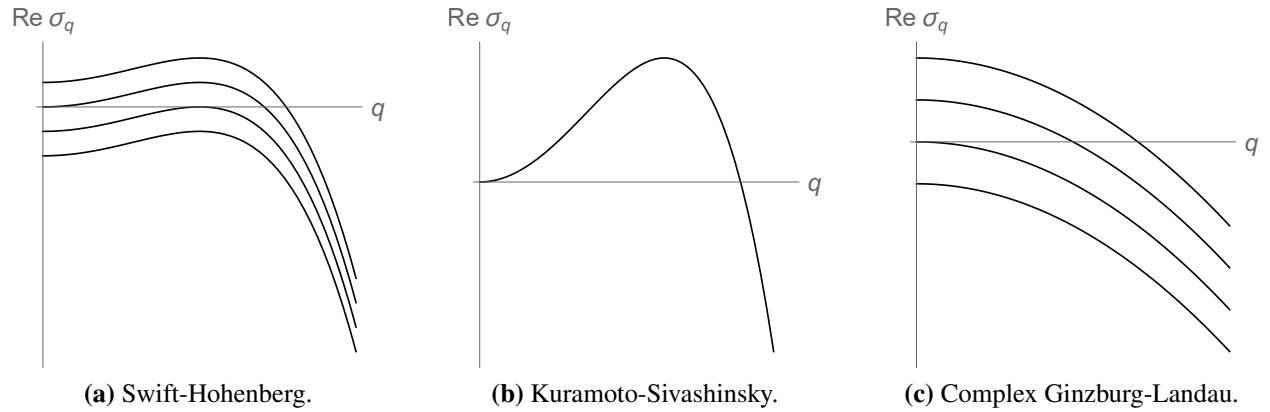


Figure 2.4: Examples of the three linear instability types according to [13, 14]. (a) The Swift-Hohenberg equation with various r values, (b) the Kuramoto-Sivashinsky equation with the control parameter scaled out. (c) The complex Ginzburg-Landau equation with various μ values. The CGLE has nonzero w_c and is type-III-o.

These linear instabilities will grow exponentially unless they are saturated by a nonlinearity.

Weakly Nonlinear Analysis

The linear analysis assumed a small perturbation and ignored nonlinear terms of the perturbation. The exponential growth of the linear instability is physically unrealistic for long times. It is the role of the nonlinear terms to balance the linear growth. When the nonlinear and linear terms are balanced the solution is said to be saturated. For a stationary instability this results in constant patterns, like stripes or hexagons. For oscillatory instabilities the linear and nonlinear terms only balance on average which leads to time-dependent patterns.

A simple example of the saturating effect of the nonlinearities can be seen using the normal forms for bifurcations in ODEs. The normal form of a transcritical bifurcation is

$$d_t u = ru - u^2 \tag{2.4}$$

which has fixed points $u = 0$ and $u = r$. For negative values of r the solutions decay without bound away from the lower unstable fixed point. If we add in a higher-order nonlinear term to (2.4) so that

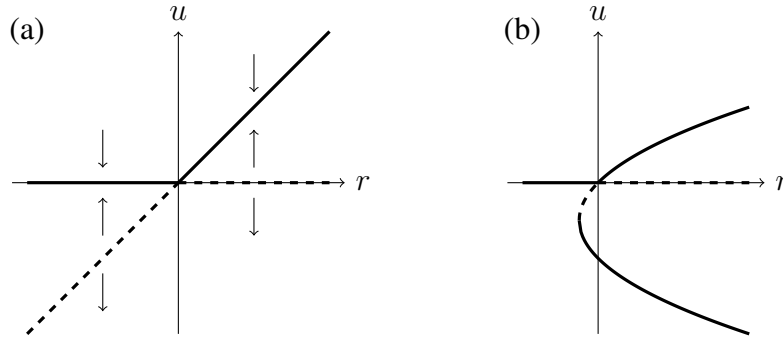


Figure 2.5: Bifurcation diagrams for (a) the standard transcritical bifurcation, and (b) transcritical with a higher-order term. The higher-order term causes the exponentially decaying solutions below the unstable fixed point to saturate into a stable fixed point.

$$d_t u = ru - u^2 - u^3, \quad (2.5)$$

we get that the fixed points are $u = 0$ and $\pm \frac{1}{2}(\sqrt{4r+1} \mp 1)$. The bifurcation diagrams for (2.4) and (2.5) are plotted in Figure 2.5. Near the origin (2.5) has the same behavior as (2.4), but the extra nonlinear term that was added causes the $u = r$ fixed point to bend in on itself so that solutions approach a stable fixed point for all values of r .

Amplitude Equations

A physical system described by $\mathbf{u}(\mathbf{x}, t)$, with the vector \mathbf{x} describing fields such as temperature, velocity, or concentration, of potentially many equations u_i can be described by a single complex-valued field $A(\mathbf{x}, t)$. This amplitude field is valid near the onset of instability and captures the main characteristics of pattern formation: (i) the growth of the perturbation around the base state, (ii) the linear growth saturation by the nonlinearity, and (iii) the effects of spatial distortions. This amplitude formalism is valid near the onset of pattern formation and for period patterns whose characteristics vary slowly in space. Near threshold the amplitude equation is able to capture the time-dependent distortions of an idealized pattern. A pattern usually only locally resembles an idealized pattern like stripes or squares, and the idealized state may distort on long length and time scales. It is on these long scales and near the instability threshold that amplitude equations are valid. This is since they are derived by an expansion of the governing equations with the dimensionless control parameter $\varepsilon = \frac{p-p_c}{p_c}$. The restriction to long length and time scales means

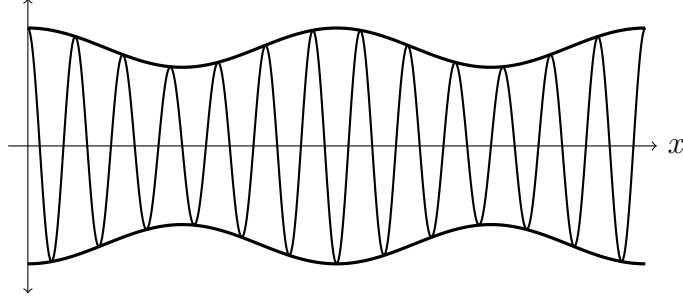


Figure 2.6: The modulation of the carrier wave $u(x) = \cos(13x)$ by the amplitude $A(x) = 0.2 \cos(2x + 1)$.

that quickly varying modulations of an ideal pattern can not be studied by amplitude equations. The long scale requirement also holds true for any boundary conditions which also need to change on the long length and time scales.

Amplitude equation can be derived from symmetry arguments or by a multiple-scales expansion and examples include both the real and complex Ginzburg-Landau equations, Helmholtz equation, and nonlinear Schrödinger equation. An amplitude equation is also called a modulation equation since it describes the modulation of the amplitude of some more general pattern wave. This is similar to how AM (amplitude modulation) radio works. The amplitude modulation of a carrier wave can be seen in Figure 2.6. The amplitude has a much smaller wave number than the carrier wave and therefore varies on a much longer length scale.

For the type-I-s instability, see Figure 2.3, near onset there is a narrow band of unstable wave numbers between q_N^- and q_N^+ centered at q_c . Using a trig identity we have for two unstable wave numbers q_1 and q_2 that

$$\cos(q_1 x) + \cos(q_2 x) = \left[2 \cos \left(\frac{q_1 - q_2}{2} x \right) \right] \cos(q_c x), \quad (2.6)$$

where $q_c = (q_1 + q_2)/2$ is the mean wave number. So then, for pairs of wave numbers centered at the critical value q_c we get that their superposition is a slowly varying amplitude modulation of the wave at critical wave number. Near onset q_1 and q_2 are near q_c so that $|q_1 - q_2| \ll q_c$ which means that the amplitude in (2.6) has a much longer wave length and varies over a larger scale than the carrier wave.

The amplitude description for 1D pattern formation was introduced by Newell and Whitehead [47], and Segel [58] to study patterns in convection. Newell and Whitehead used a continuous band of wavenumbers instead of a discrete band of modes of previous works, and made note of the diffusive spread of perturbations. Segel used the slow modulation of the amplitude to study the effects of side walls on the patterns.

Multiple-scales Analysis

Amplitude equations can be derived from symmetry and phenomenological arguments, but also more rigorously via a multiple-scales analysis. The governing equations u have the fast time scales x , y , and t , but from the discussion of amplitude equations we know that there is the slow space and time scale of the slowly varying amplitude. These slow space and time variables are $X = \varepsilon^{p_x}x$, $Y = \varepsilon^{p_y}y$, $T = \varepsilon^{p_t}t$ where the exponents of ε for each variable can be deduced from the governing equation itself or from the expansion.

For example, for the Swift-Hohenberg equation

$$\partial_t u = [\mu - (\Delta + q_c^2)]u - u^3, \quad (2.7)$$

near threshold when the control parameter scales as $\mu \rightarrow \varepsilon^2\mu$, the correct scalings of time and space are $T = \varepsilon^2t$, $X = \varepsilon x$, and $\sqrt{\varepsilon}y$. These lead to the substitutions $\partial_x \rightarrow \partial_x + \varepsilon\partial_X$, $\partial_y \rightarrow \partial_y + \sqrt{\varepsilon}\partial_Y$, and $\partial_t \rightarrow \partial_t + \varepsilon^2\partial_T$. Using these in (2.7) together with the expansion $u = \varepsilon u_1 + \varepsilon^2 u_2 + \dots$ gives a set of equations for the u_i 's. There will be resonant terms which will grow unbounded unless their coefficients are set to zero. Setting the coefficient to zero results in the amplitude equation.

Phase Equations

The phase of the complex amplitude gives the position of the pattern and captures symmetry aspects of the pattern. Similarly to how an amplitude equation can be derived for the slowly varying amplitude of a perturbation to a set of governing equations, a perturbation to the phase ϕ of the amplitude $A = ae^{i\phi}$ is also slowly varying. Perturbations to the magnitude a of the amplitude have

relaxational dynamics and can be adiabatically eliminated to recover a phase diffusion equation that describes the slow variation in the phase of the amplitude.

2.1.2 The Complex Ginzburg-Landau Equation (Isotropic)

One example of an amplitude equation is the complex Ginzburg-Landau equation (CGLE)

$$\partial_t A = \mu A + (1 + i\alpha)\Delta A - (1 + i\beta)|A|^2 A, \quad (2.8)$$

whose anisotropic version features significantly in this dissertation. The CGLE is the canonical equation describing the dynamics of the slowly varying amplitude near the onset of a supercritical Hopf bifurcation in spatially extended systems. It can be derived via a multiple-scales analysis from many physical systems, but can also be derived independently of any physical system such as from either a reaction-diffusion system [33], or as the amplitude equation of a modulated stripe near a type-I-s instability in the language of [13]. In the limit as the parameters $\alpha \rightarrow 0$, $\beta \rightarrow 0$ the CGLE reduces to the real Ginzburg-Landau equation (RGLE). In the limit as $\alpha \rightarrow \infty$ and $\beta \rightarrow \infty$ the CGLE becomes the nonlinear Schrödinger equation [1, 11, 33].

Coherent Structures

In addition to the methods previously described, *coherent structures* have been used to study the CGLE and its solutions, as their use often results in a more tractable system of ODEs which describes the behavior of solutions to the CGLE. Coherent structures are solutions, or features of solutions, that are localized in space. These include fronts, pulses, sources, and sinks in one spatial dimension, and targets, spirals, dislocations, and grain boundaries in two dimensions [69]. A dynamical system in terms of the wave variable $\xi = x - ct$ can be derived from a PDE in certain cases. For example, the uniformly translating solution $A(\xi) = a(\xi)e^{i\phi(\xi)}$ yields a set of three ODEs when plugged in the CGLE. The heteroclinic solutions of the dynamical system are the coherent structures. As an example, in one dimension the heteroclinic solution connecting one with zero is a front.

Bohr et al. [5, 6] were able to approximate the shock wall positions that surround the spiral domains in the BFN stable region by a hyperbola if the distance between two spirals is significantly larger than the wavelength in which case the phase of the spiral is given by a simple formula.

In [68] the author found that coherent structures called homoclinic holes describe spatiotemporal intermittency and are connected to phase slips. The authors take a uniformly propagating ansatz $A(x, t) = a(z)e^{i\omega t}$ to get a system of ODEs whose fixed points are plane waves. Homoclinic orbits connecting two of the fixed points correspond to the sought after intermittent solutions with $q_l = q_r$. They determined heteroclinic Nozaki-Bekki holes and homoclinic holes are two distinct types of hole solutions of the CGLE. The authors say that, loosely speaking, homoclinic holes are unstable equilibria between plane waves and phase slips.

In [8, 9] Brusch et al. used the pulse-like periodic coherent structure

$$A(x, t) = a(x - vt)e^{i\phi(x-vt)}e^{-i\omega t} \quad (2.9)$$

with period P to investigate the transition from phase to defect chaos in the 1D CGLE. Plugging (2.9) into the CGLE gives a system of three ODEs in the variables a , $b = da/dz$, and $\psi = d\phi/dz$ where $z = x - vt$. They call the periodic coherent structures modulated amplitude waves (MAWs); these are the limit cycles of the ODE system. For the case where the average phase gradient is zero, or in other words when $A(x, t) = e^{-i\beta t}$, MAWs bifurcate from unstable plane waves. As the linear and nonlinear dispersion coefficients α and β , are increased the MAWs undergo a saddle-node (SN) bifurcation. This happens when the period of the MAW becomes larger than the period at the saddle-node.

In [36] the authors recast the 1D CGLE in a finite box with periodic boundary conditions as a fourth-order ODE in terms of the modulation of the amplitude squared of a plane wave solution. This is used to prove the existence of MAWs in two cases: bifurcation of the trivial solution $A = 0$, and bifurcation of the plane wave solution with zero wavenumber.

Sherratt et al. [59] looked at patterns of sources and sinks in the CGLE without linear dispersion. This allows the CGLE to be transformed into a reaction-diffusion for u and v by using

$A = u + iv$. The source-sink patterns are similar to homoclinic hole solutions in that they are both localized disturbances to wavetrains, but the source-sink patterns contain a band of oppositely moving wavetrains. Homoclinic holes are connect via a wavetrain while source-sink patterns are instead connected around a heteroclinic cycle. MAWs are distinct from the repeating patterns of sources and sinks.

Phase diagram

Similar to the well know stability or Busse ballon analysis which plots the control parameter against the wavenumber to study the stability of solutions, the phase diagram bounds different solution types into regions based on the non-control parameters of linear and nonlinear dispersion. The phase diagram of the 2D CGLE given by Chaté and Manneville in [11], see Figure 2.7, is broken into regions by several lines: BF , S_1 , S_2 , L , and T . The BF line represents the Benjamin-Feir-Newell instability. The S_1 and S_2 lines denote where plane waves become linearly or absolutely unstable respectively. Between the two S lines perturbations are amplified and convected away from the spiral core. To the left of the L line is when phase chaos (turbulence) is transient. The T line is the division between phase chaos (to the right) and defect chaos (to the left). As the parameters are varied a the solution crosses one of these lines it undergoes a "phase" transition. The form of the CGLE used [11] requires the transformation $A \rightarrow \sqrt{i}A$ to get to (2.8). Their b_1 is unaffected by this transformation and directly relates to α_1 , but the nonlinear coefficient $-(b_3 - i)$ becomes our $-(1 + i\beta)$.

Linear Stability Analysis

We perform a linear stability analysis on the CGLE (2.8). Let

$$A = R_0(1 + r)e^{i(\mathbf{k} \cdot \mathbf{X} - \omega T + \phi)}, \quad R_0^2 = \mu - \mathbf{k}^2, \quad \omega = \beta R_0^2 + \alpha \mathbf{k}^2. \quad (2.10)$$

where $\mathbf{k} = (k_x, k_y)$, $\mathbf{X} = (X, Y)$, and $r, \phi \ll 1$ are small perturbations to the amplitude and phase of a uniform traveling wave solution. Substituting this into (2.8) then separating real and

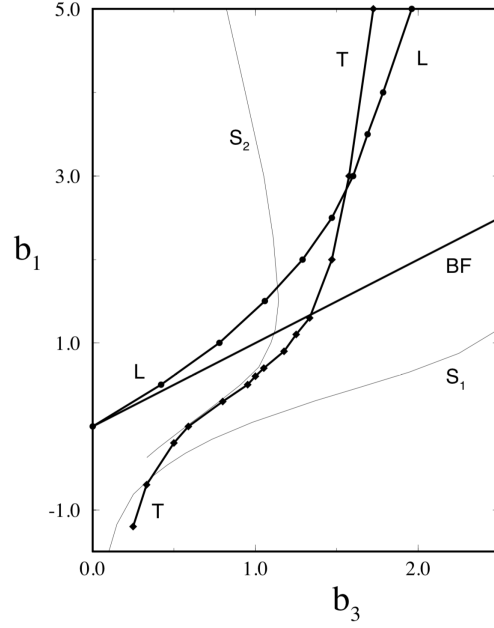


Figure 2.7: Phase diagram given by Chaté and Manneville. Reprinted from [11], Copyright 1996, with permission from Elsevier.

imaginary parts yields dynamic equations for the two perturbations.

$$\begin{aligned} \partial_T r = & -2R_0^2 - 3R_0^2 r^2 - R_0^2 r^3 - 2\alpha(k_1 \partial_X r + k_2 \partial_Y r + \partial_X r \partial_X \phi + \partial_Y r \partial_Y \phi) + \partial_X^2 r + \partial_Y^2 r \\ & - (1+r)[2(k_1 \partial_X \phi + k_2 \partial_Y \phi) + \alpha(\partial_X^2 \phi + \partial_Y^2 \phi) + (\partial_X \phi)^2 + (\partial_Y \phi)^2], \end{aligned} \quad (2.11a)$$

$$\begin{aligned} \partial_T \phi = & 2k_1 \partial_X r - 2\alpha k_1 \partial_X \phi + 2\partial_X r \partial_X \phi - \alpha(\partial_X \phi)^2 + \alpha \partial_X^2 r + \partial_X^2 \phi \\ & + 2k_2 \partial_Y r - 2\alpha k_2 \partial_Y \phi + 2\partial_Y r \partial_Y \phi - \alpha(\partial_Y \phi)^2 + \alpha \partial_Y^2 r + \partial_Y^2 \phi \\ & + r[-2R_0^2 \beta - 2k_1 \partial_X r - 2\partial_X r \partial_X \phi - \alpha \partial_X^2 r - 2k_2 \partial_Y r - 2\partial_Y r \partial_Y \phi - \alpha \partial_Y^2 r] + \mathcal{O}(r^2). \end{aligned} \quad (2.11b)$$

We now linearize the above equations about the solution $(r, \phi) = (0, 0)$ to get

$$\partial_T r = -2R_0^2 - 2\alpha(k_1\partial_X r + k_2\partial_Y r) + \partial_X^2 r + \partial_Y^2 r - 2(k_1\partial_X \phi + k_2\partial_Y \phi) - \alpha(\partial_X^2 \phi - \partial_Y^2 \phi), \quad (2.12a)$$

$$\partial_T \phi = -2R_0^2 \beta r + 2(k_1\partial_X r + k_2\partial_Y r) + \alpha(\partial_X^2 r + \partial_Y^2 r) - 2\alpha(k_1\partial_X \phi + k_2\partial_Y \phi) + \partial_X^2 \phi + \partial_Y^2 \phi. \quad (2.12b)$$

Setting $r = \hat{r}e^{\sigma T + iq \cdot \mathbf{X}}$ and $\phi = \hat{\phi}e^{\sigma T + iq \cdot \mathbf{X}}$ where $|q| \ll |k|$, we can get the eigenvalues

$$\sigma_1 = -2R_0^2 + \mathcal{O}(q), \quad (2.13a)$$

$$\begin{aligned} \sigma_2 = 2i(\beta - \alpha)(k_1 q_1 + k_2 q_2) - (1 + \alpha\beta)(q_1^2 + q_2^2) \\ + \frac{1 + \beta^2}{R_0^2} [2k_1^2 q_1^2 + 2k_2^2 q_2^2 + 4k_1 k_2 q_1 q_2] + \mathcal{O}(q^3). \end{aligned} \quad (2.13b)$$

The first eigenvalue σ_1 decays exponentially and is always stable. For instability we need $\text{Re}(\sigma_2) > 0$. This will happen when

$$-(1 + \alpha\beta)(q_1^2 + q_2^2) + \frac{1 + \beta^2}{R_0^2} (2k_1^2 q_1^2 + 2k_2^2 q_2^2 + 4k_1 k_2 q_1 q_2) > 0. \quad (2.14)$$

For the 1D case, say along the x -direction when $q_2 = 0$, we recover the condition

$$-(1 + \alpha\beta) + \frac{2k_1^2(1 + \beta^2)}{R_0^2} > 0. \quad (2.15)$$

From (2.15) we see that the Benjamin-Feir instability will happen when $k_1 = 0$ and the Eckhaus instability will happen when $\alpha = \beta = 0$ [38].

Weakly nonlinear analysis for long-wave instability

A linear phase equation can be extracted from the second eigenvalue in (2.13b) if we expand to fourth-order in q . Then after picking the appropriate nonlinear term we can use Kuramoto's method [32] to find its coefficient. We will use another approach here based on [17], and again in the section on the anisotropic CGLE.

Since we are looking for a long-wave instability where $\mathbf{k} = 0$, the ansatz in (2.10) becomes

$$A = \sqrt{\mu}(1+r)e^{i(-\beta\mu T+\phi)}. \quad (2.16)$$

From the linear stability we know that amplitude perturbations decay rapidly compared to phase perturbations. Using this insight we can use a multiple-scales analysis to get a *phase-diffusion equation*. From [17], we use the scalings

$$r(x, y, t) = \delta^6 W(\delta x, \delta y, \delta^4 t), \quad \psi(x, y, t) = \delta^3 \Psi(\delta x, \delta y, \delta^4 t), \quad (2.17)$$

and let $\psi = \nabla\phi = (\psi_x, \psi_y) = (\partial_X\phi, \partial_Y\phi)$ be the phase gradient. Plugging (2.16) into the CGLE (2.8) results in

$$\begin{aligned} \partial_T r = & -2\mu r - 3\mu r^2 - \mu r^3 + \partial_X^2 r + \partial_Y^2 r - (1+r)((\partial_X\phi)^2 + (\partial_Y\phi)^2) \\ & - \alpha(1+r)(\partial_X^2\phi + \partial_Y^2\phi) - 2\alpha(\partial_X r \partial_X\phi + \partial_Y r \partial_Y\phi), \end{aligned} \quad (2.18a)$$

$$\begin{aligned} \partial_T \phi = & -2\mu\beta r - \mu\beta r^2 - \alpha((\partial_X\phi)^2 + (\partial_Y\phi)^2) + \partial_X^2\phi + \partial_Y^2\phi \\ & + \frac{2(\partial_X r \partial_X\phi + \partial_Y r \partial_Y\phi) + \alpha(\partial_X^2 r + \partial_Y^2 r)}{1+r}. \end{aligned} \quad (2.18b)$$

Which may be written as

$$\partial_T r = -2\mu r - 3\mu r^2 - \mu r^3 + \Delta r - 2\alpha \nabla r \cdot \nabla\phi - (1+r)(|\nabla\phi|^2 + \alpha\Delta\phi), \quad (2.19a)$$

$$\partial_T \phi = -2\mu\beta r - \mu\beta r^2 - \alpha|\nabla\phi|^2 + \Delta\phi + \frac{2\nabla r \cdot \nabla\phi + \alpha\Delta r}{1+r}. \quad (2.19b)$$

Using the phase gradient substitution gives

$$\partial_T r = -\mu(2r + 3r^2 + r^3) + \Delta r - 2\alpha \nabla r \cdot \psi - (1+r)(|\psi|^2 + \alpha \nabla \cdot \psi), \quad (2.20a)$$

$$\partial_T \psi = \nabla \left(-\mu(2\beta r + \beta r^2) - \alpha|\psi|^2 + \nabla \cdot \psi + \frac{2\nabla r \cdot \psi + \alpha\Delta r}{1+r} \right) \quad (2.20b)$$

$$= \Delta\psi + \nabla \left(-\mu(2\beta r + \beta r^2) - \alpha|\psi|^2 + \frac{2\nabla r \cdot \psi + \alpha\Delta r}{1+r} \right). \quad (2.20c)$$

We can now using the scalings (2.17) in the above equations to obtain

$$\begin{aligned} \delta^{10} \partial_T W &= -\mu \delta^6 (2W + \delta^6 3W^2 + \delta^{12} W^3) + \delta^8 \Delta W \\ &\quad - 2\delta^{10} \alpha \nabla W \cdot \Psi - \delta^6 (1 + \delta^6 W) (|\Psi|^2 + \delta^{-2} \alpha \nabla \cdot \Psi), \end{aligned} \quad (2.21a)$$

$$\delta^7 \partial_T \Psi = \delta^5 \Delta \Psi + \delta \nabla \left(-\mu \delta^6 (2\beta W + \beta \delta^6 W^2) - \delta^6 \alpha |\Psi|^2 + \frac{\delta^{10} 2 \nabla W \cdot \Psi + \delta^8 \alpha \Delta W}{1 + \delta^6 W} \right), \quad (2.21b)$$

and divide the two equations by δ^6 and δ^7 respectively to obtain

$$\begin{aligned} \delta^4 \partial_T W &= -\mu (2W + \delta^6 3W^2 + \delta^{12} W^3) + \delta^2 \Delta W \\ &\quad - 2\delta^4 \alpha \nabla W \cdot \Psi - (1 + \delta^6 W) (|\Psi|^2 + \delta^{-2} \alpha \nabla \cdot \Psi), \end{aligned} \quad (2.22a)$$

$$\partial_T \Psi = \delta^{-2} \Delta \Psi - \nabla (2\mu \beta W + \alpha |\Psi|^2) + \delta^2 \nabla \left(\frac{2\delta^2 \nabla W \cdot \Psi + \alpha \Delta W}{1 + \delta^6 W} - \mu \beta \delta^6 W^2 \right). \quad (2.22b)$$

At leading order in W and Ψ the first equation is

$$W = -\frac{\alpha}{2\mu\delta^2} \nabla \cdot \Psi + \mathcal{O}(1). \quad (2.23)$$

Using this in the first equation at $\mathcal{O}(1)$ gives

$$0 = -\mu 2W - |\Psi|^2 - \frac{\alpha}{\delta^2} \nabla \cdot \Psi - \delta^2 \Delta \frac{\alpha}{2\mu\delta^2} \nabla \cdot \Psi + \mathcal{O}(\delta), \quad (2.24)$$

resulting in a solution

$$W = -\frac{|\Psi|^2}{2\mu} - \frac{\alpha}{2\mu\delta^2} \nabla \cdot \Psi - \frac{\alpha}{4\mu^2} \Delta (\nabla \cdot \Psi) + \mathcal{O}(\delta). \quad (2.25)$$

This can now be substituted into the Ψ equation yielding

$$\begin{aligned} \partial_T \Psi = & \delta^{-2} \Delta \Psi - \nabla \left(2\mu\beta \left[-\frac{|\Psi|^2}{2\mu} - \frac{\alpha}{2\mu\delta^2} \nabla \cdot \Psi - \frac{\alpha}{4\mu^2} \Delta(\nabla \cdot \Psi) \right] + \alpha|\Psi|^2 \right) \\ & + \delta^2 \alpha \nabla^3 \left[-\frac{|\Psi|^2}{2\mu} - \frac{\alpha}{2\mu\delta^2} \nabla \cdot \Psi - \frac{\alpha}{4\mu^2} \Delta(\nabla \cdot \Psi) \right] + h.o.t. \end{aligned} \quad (2.26)$$

Simplifying gives

$$\partial_T \Psi = \frac{1 + \alpha\beta}{\delta^2} \Delta \Psi + \frac{\alpha(\beta - \alpha)}{2\mu} \Delta^2 \Psi + (\beta - \alpha) \nabla(|\Psi|^2) + \mathcal{O}(\delta). \quad (2.27)$$

Near the instability we can set $1 + \alpha\beta = \kappa\delta^2$ giving the equation

$$\partial_T \Psi = \kappa \Delta \Psi + \frac{\alpha(\beta - \alpha)}{2\mu} \Delta^2 \Psi + (\beta - \alpha) \nabla(|\Psi|^2) + \mathcal{O}(\delta). \quad (2.28)$$

Defining $q := \Psi|_{\delta=0}$ gives the 2D Kuramoto-Sivashinsky equation

$$\partial_T q = \kappa \Delta q + \frac{\alpha(\beta - \alpha)}{2\mu} \Delta^2 q + (\beta - \alpha) \nabla(|q|^2) \quad (2.29)$$

for the wave number q in derivative form. Using $\Phi = \int_{-\infty}^x q \cdot ds$ gives the integrated form of the KS equation for the scaled phase

$$\partial_T \Phi = \kappa \Delta \Phi + \frac{\alpha(\beta - \alpha)}{2\mu} \Delta^2 \Phi + (\beta - \alpha) (|\nabla \Phi|^2). \quad (2.30)$$

Example Solutions of the CGLE

Some examples of the variety of solutions the CGLE produces are seen in Figure 2.8. Amongst these are frozen states characterized by a cellular structure with spiral defects surrounded by shock wall boundaries, defect chaos, and phase chaos. The frozen and chaotic states depend on the initial conditions provided. The spiral defects are demonstrated in Figure 2.9 where the phase clearly shows the spiral structure. Figure 2.9 has a side-by-side of phase and defect chaos. Phase chaos is characterized by the amplitude of A being bounded away from zero. In defect chaos, the amplitude is zero at defects which leads to the phase being undefined. The parameter region for

phase chaos is considerably smaller than that of defect chaos. For some some parameter values, phase chaos exists for early times but is only transient and the solutions evolve into defect chaos. In 1D MAWs [9] have been used to describe this transition and it occurs when the peak-to-peak distance becomes too large. A similar behavior is seen in 2D where defects appear when the cells in the phase chaotic solution grow too large. Interesting fronts develop around the defects and spread out, turning the entire domain into a defect chaotic state, see Figure 2.11. The nucleation of these defect chaos containing fronts is reminiscent of the vortex class solutions described in [11], but in that case stable spirals of the kind in Figure 2.9 nucleate out of defect chaos, whereas ours are unstable spirals nucleating out of phase chaos.

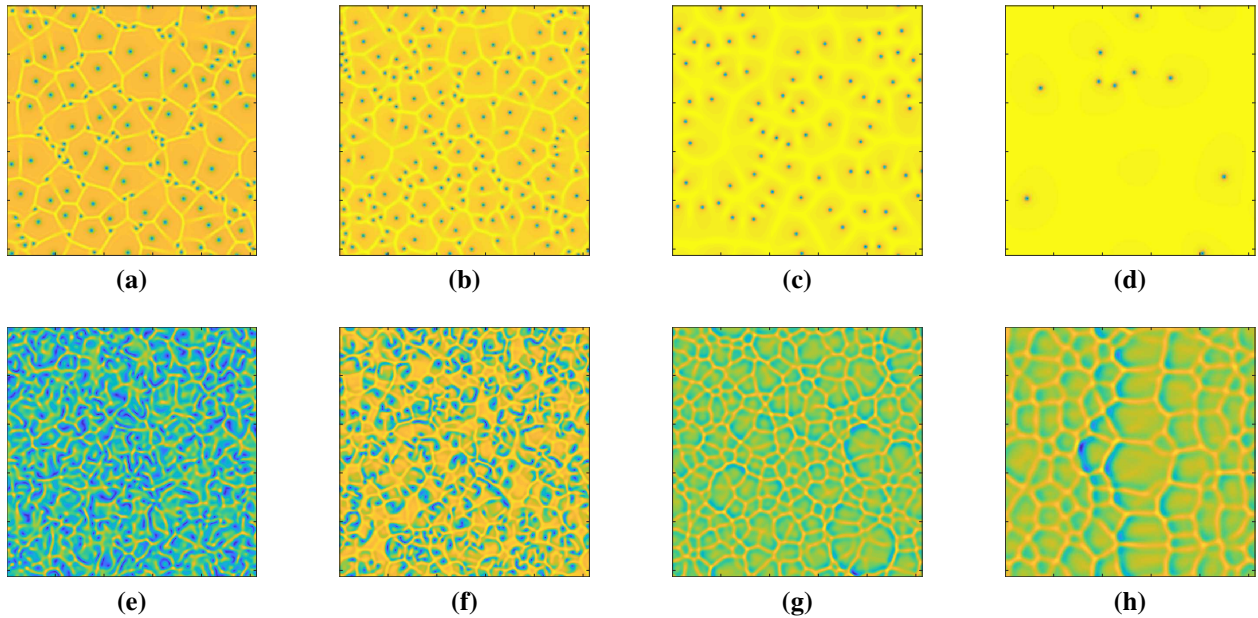
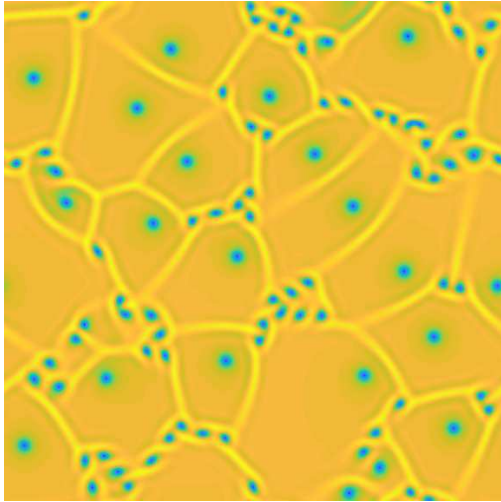
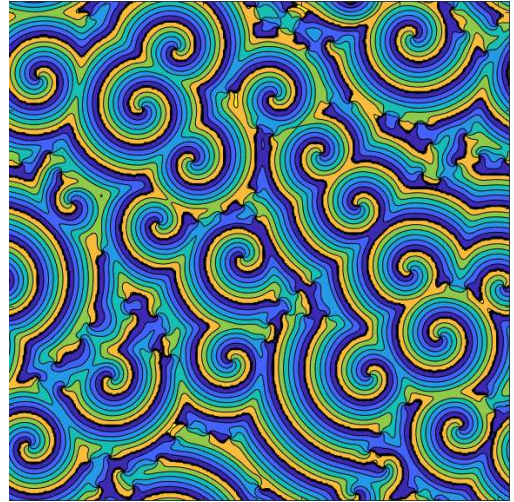


Figure 2.8: Various numerical solutions of the CGLE. (a-d) Frozen cellular states where defect spiral cores are separated by shock wall boundaries. For a fixed β value, From left to right corresponds to an α value that starts unstable and is then brought closer and crosses the BFN stability boundary. (e-f) Defect chaos. (g-h) Phase chaos. The phase chaotic solution in (h) started from a single stripe aligned vertically whose influence can be seen in the cellular structure. For a fixed β value phase chaos occurs for an α value well in the BFN unstable regime. As α is brought closer to BFN stability the solution in (e) changes to (f), then in a small region near the boundary to the phase chaos seen in (g).

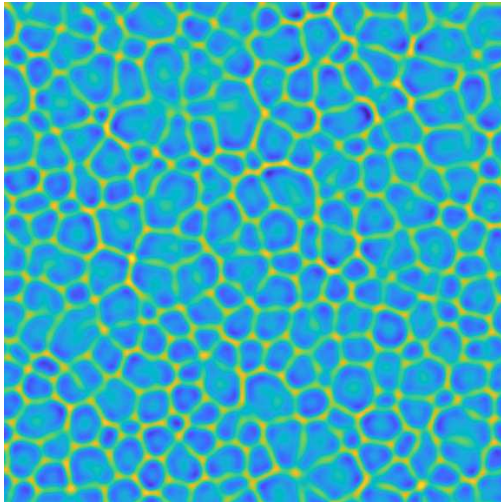


(a) $|A|$.

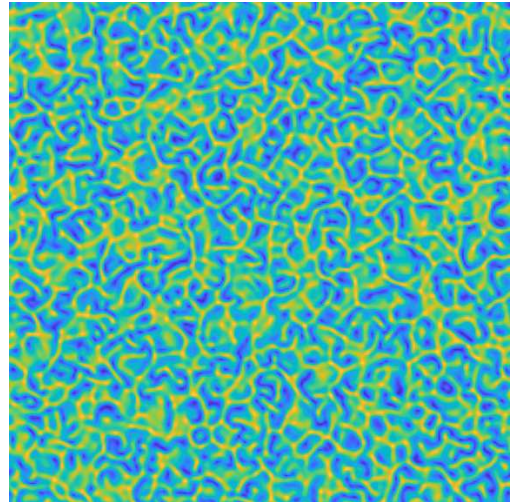


(b) Phase of A .

Figure 2.9: Hole and shock-wall solution to the CGLE. (a) The magnitude of the solution and (b) a contour plot of the phase showing the spiral structure.

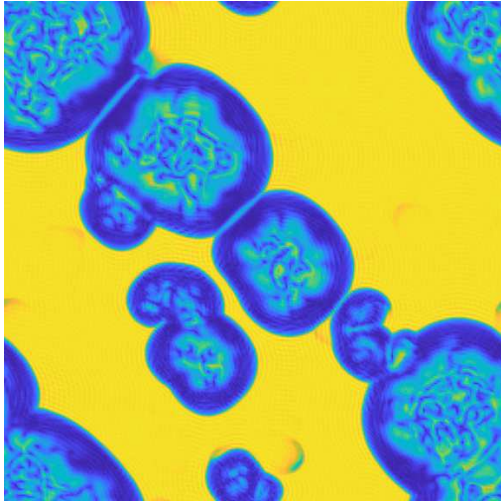


(a) Phase chaos in the CGLE.

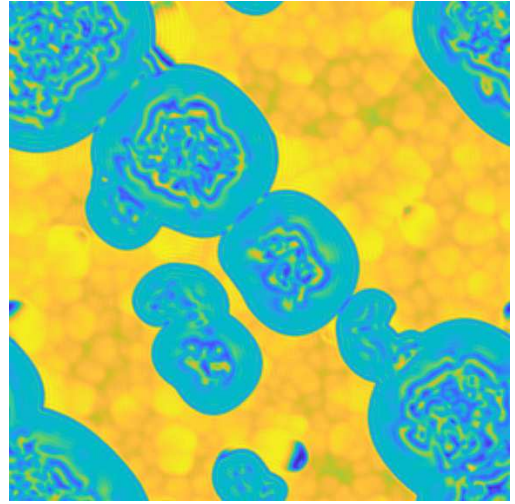


(b) Defect chaos in the CGLE.

Figure 2.10: Chaotic solutions to the CGLE. (a) Phase chaos where the amplitude is bounded away from zero $|A| > 0$ and (b) defect chaos which has regions of vanishing $|A|$.



(a) $|A|$.



(b) $\text{Re } A$.

Figure 2.11: A transient vortex glass like state with propagating regions emanating from defects. The interior of the region is chaotic unlike the inside of the cells in true vortex glass. This solution connects an initial phase chaotic state to defect chaos.

2.2 Anisotropic Complex Ginzburg-Landau

There has been much less research into the anisotropic complex Ginzburg-Landau equation (ACGLE) compared with the CGLE. A limited investigation of phase chaos in the ACGLE was done in [19]. A study of a perturbed amplitude in the longwave case was done in [7]. The authors of this paper used a perturbed ansatz of the form $A(x, y, t) = \sqrt{\mu}(1 + r(x, y, t))e^{-i\beta\mu t}$ which lacks any phase perturbation as in (2.47). A globally coupled system of Ginzburg-Landau equations was used to study the modulational stability of traveling waves in anisotropic systems in [15], but the form of Equation (2.31) was only mentioned.

In this section we look at the solutions, linear stability, and phase equations for the ACGLE where the anisotropy presents itself in the linear dispersion terms. The two-dimensional ACGLE is

$$\partial_t A = \mu A + (1 + i\alpha_1)\partial_x^2 A + (1 + i\alpha_2)\partial_y^2 A - (1 + i\beta)|A|^2 A. \quad (2.31)$$

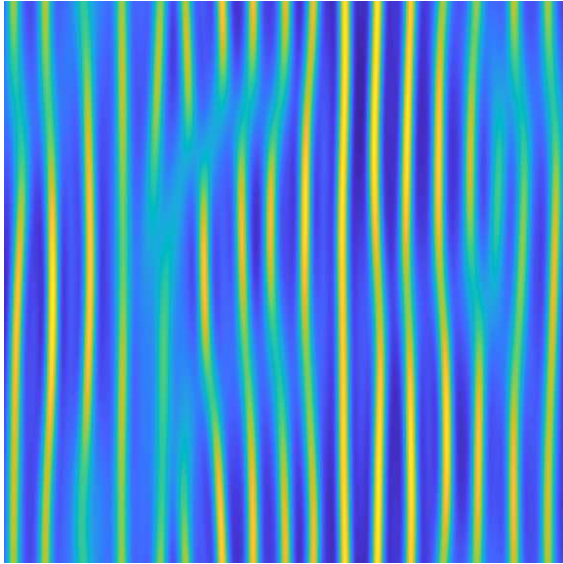
A traveling plane wave, see Figure 2.14, solution to the ACGLE in the k -direction and frequency ω is given by

$$A = R_0 e^{i(\mathbf{k} \cdot \mathbf{x} - \omega t)}, \quad (2.32a)$$

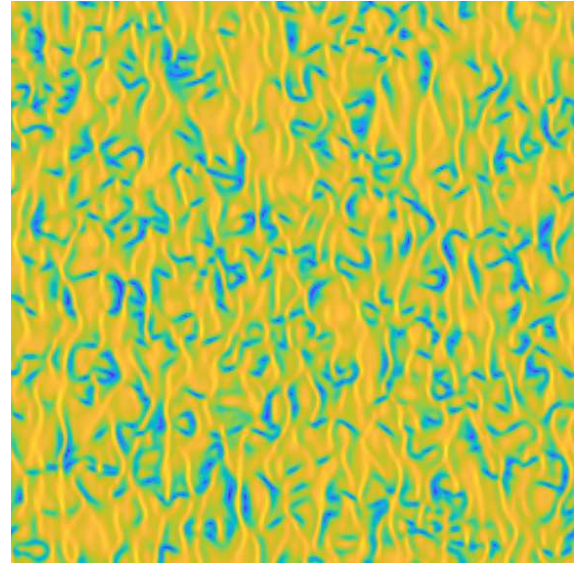
$$R_0^2 = \mu - (k_1^2 + k_2^2), \quad (2.32b)$$

$$\omega = \beta R_0^2 + \alpha_1 k_1^2 + \alpha_2 k_2^2, \quad (2.32c)$$

where $\mathbf{k} = (k_1, k_2)$ and $\mathbf{x} = (x, y)$. The requirements (2.32b) and (2.32c) are found by substituting (2.32a) into the ACGLE (2.31).



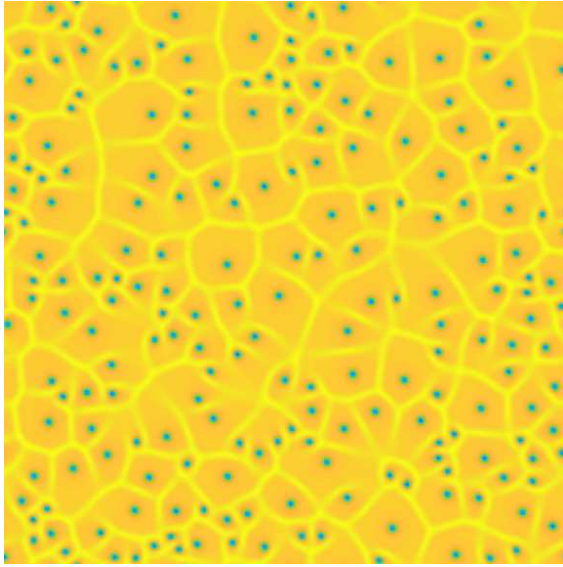
(a) Phase chaos in the ACGLE.



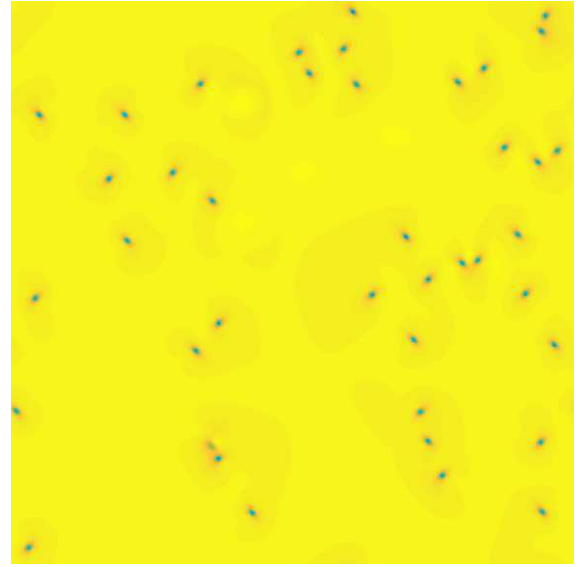
(b) Defect chaos in the ACGLE.

Figure 2.12: Chaotic solutions to the ACGLE where plane waves are stable in the y -direction and unstable in the x -direction. (a) Phase chaos where the amplitude is bounded away from zero $|A| > 0$. The cellular structure of the phase chaotic solution of the CGLE has been replaced with a ripple structure. The stability in the y -direction is also apparent in the defect chaos parameter regime (b) which shows partial coherence in the stable direction. The regions of defects appears to travel horizontally along the unstable direction.

The ACGLE is capable of producing any CGLE solution by setting $\alpha_1 = \alpha_2$, but the added anisotropy allows for solutions that are not possible in the isotropic case. Not only can traveling plane waves have different degrees of stability or instability in the x and y directions, they can now be both stable and unstable to perturbations depending on direction. For example, in the CGLE phase chaos demonstrates itself as an evolving cellular structure. This type of phase chaos can exist in the ACGLE, but as one of the linear dispersion parameters is adjusted so that traveling



(a) CGLE $|A|$.



(b) ACGLE $|A|$.

Figure 2.13: Hole and shock-wall solutions: (a) The isotropic case $\alpha_1 = \alpha_2$ produces a stable cellular structure wherein spiral defects are confined by shock walls; (b) The anisotropic case $\alpha_1 < 0 < \alpha_2$ sees the spiral defects break free of their cells, convect, and annihilate similarly to the isotropic case, but now the spiral centers have an obvious slant depending on which way they are rotating. The spiral centers appear radially symmetric in the isotropic case, see Figure 2.8(c-d).

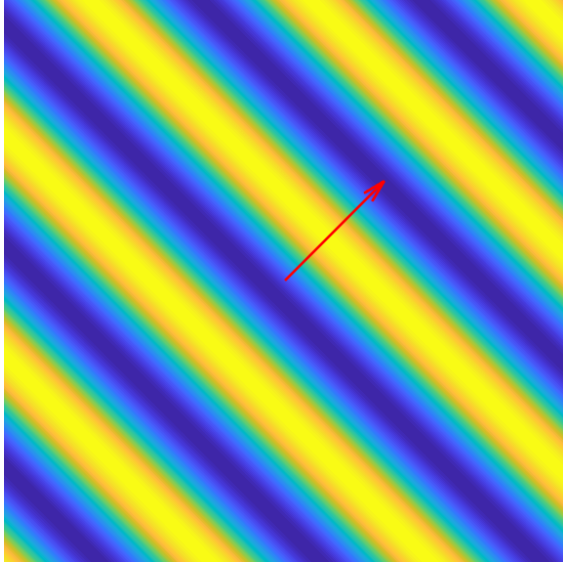
waves become BFN stable in one direction the isotropic cellular behavior gives way to a phase chaotic structure of ripples which are aligned along the stable direction, see Figure 2.12a. A similar behavior also happens for parameter values which yield defect chaos in the CGLE. As one direction is made BFN stable, ripples appear aligned along the stable direction. Defects appear and travel mostly along the unstable direction, see Figure 2.12b.

2.2.1 Linear Stability Analysis

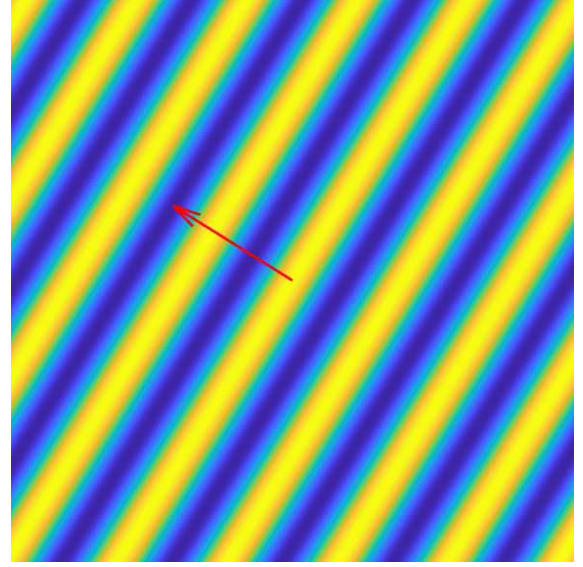
To determine the stability of the traveling wave solution (2.32) we can perturb it and see how the perturbations evolve in time. Perturbing the amplitude and phase we get

$$A(x, y, t) = R_0(1 + r(x, y, t))e^{i[\mathbf{k} \cdot \mathbf{x} - \omega t + \phi(x, y, t)]}. \quad (2.33)$$

Plugging (2.33) into (2.31) then separating real and imaginary parts leads to dynamic equations for the perturbations



(a) $\mathbf{k} = (4, 4)$.



(b) $\mathbf{k} = (-8, 5)$.

Figure 2.14: Examples of traveling waves of the form $e^{i(\mathbf{k}\cdot\mathbf{x}-\omega t)}$. The real part is shown. The red arrow denotes the \mathbf{k} -direction along which the wave moves.

$$\begin{aligned}
\partial_t r &= -R_0^2 + \mu - 3R_0^2 r^2 - R_0^2 r^3 - (k_2 + \partial_y \phi)(k_2 + 2\alpha_2 \partial_y r + \partial_y \phi) \\
&+ \partial_y^2 r - \alpha_2 \partial_y^2 \phi - (k_1 + \partial_x \phi)(k_1 + 2\alpha_1 \partial_x r + \partial_x \phi) \\
&+ \partial_x^2 r - \alpha_1 \partial_x^2 \phi - r(3R_0^2 - \mu + (k_2 + \partial_y \phi)^2 + \alpha_2 \partial_y^2 \phi + (k_1 + \partial_x \phi)^2 + \alpha_1 \partial_x^2 \phi),
\end{aligned} \tag{2.34}$$

$$\begin{aligned}
\partial_t \phi &= \frac{1}{1+r} \left[-R_0^2 \beta + \omega - 3R_0^2 \beta r^2 - R_0^2 \beta r^3 - (k_2 + \partial_y \phi)(-2\partial_y r + \alpha_2(k_2 + \partial_y \phi)) \right. \\
&+ \alpha_2 \partial_y^2 r + \partial_y^2 \phi - (k_1 + \partial_x \phi)(-2\partial_x r + \alpha_1(k_1 + \partial_x \phi)) \\
&\left. + \alpha_1 \partial_x^2 r - r(3R_0^2 \beta - \omega + \alpha_2(k_2 + \partial_y \phi)^2 - \partial_y^2 \phi + \alpha_1(k_1 + \partial_x \phi)^2 - \partial_x^2 \phi) + \partial_x^2 \phi \right].
\end{aligned} \tag{2.35}$$

After expanding and using the requirements (2.32b) and (2.32c) for R_0^2 and ω , the equation for the amplitude perturbation r is

$$\begin{aligned}
\partial_t r &= -2R_0^2 r - 3R_0^2 r^2 - R_0^2 r^3 + \partial_x^2 r + \partial_y^2 r - (\partial_x \phi)^2 - (\partial_y \phi)^2 - r(\partial_x \phi)^2 - r(\partial_y \phi)^2 \\
&- 2k_1 \alpha_1 \partial_x r - 2k_2 \alpha_2 \partial_y r - 2k_1 \partial_x \phi - 2k_2 \partial_y \phi - 2k_1 r \partial_x \phi - 2k_2 r \partial_y \phi \\
&- \alpha_1 \partial_x^2 \phi - r \alpha_1 \partial_x^2 \phi - \alpha_2 \partial_y^2 \phi - r \alpha_2 \partial_y^2 \phi - 2\alpha_1 \partial_x r \partial_x \phi - 2\alpha_2 \partial_y r \partial_y \phi.
\end{aligned} \tag{2.36}$$

A useful substitution to use in expanding to get (2.36) is

$$-R_0^2\beta - 3R_0^2\beta r - 3R_0^2\beta r^2 - R_0^2\beta r^3 = -R_0^2\beta - R_0^2\beta r - 2R_0^2\beta r - 2R_0^2\beta r^2 - R_0^2\beta r^2 - R_0^2\beta r^3.$$

After expanding and simplifying, the equation for the phase perturbation ϕ becomes

$$\begin{aligned} \partial_t\phi &= \omega - R_0^2\beta - 2R_0^2\beta r - R_0^2\beta r^2 - k_1^2\alpha_1 - k_2^2\alpha_2 - \alpha_1(\partial_x\phi)^2 - \alpha_2(\partial_y\phi)^2 \\ &+ \partial_x^2\phi + \partial_y^2\phi - 2k_1\alpha_1\partial_x\phi - 2k_2\alpha_2\partial_y\phi \\ &+ \frac{1}{1+r} \left[\alpha_1\partial_x^2r + \alpha_2\partial_y^2r + 2k_1\partial_xr + 2k_2\partial_yr + 2\partial_xr\partial_x\phi + 2\partial_yr\partial_y\phi \right]. \end{aligned} \quad (2.37)$$

Using the requirement (2.32c) for ω , this becomes

$$\begin{aligned} \partial_t\phi &= -2R_0^2\beta r - R_0^2\beta r^2 - \alpha_1(\partial_x\phi)^2 - \alpha_2(\partial_y\phi)^2 + \partial_x^2\phi + \partial_y^2\phi - 2k_1\alpha_1\partial_x\phi - 2k_2\alpha_2\partial_y\phi \\ &+ \frac{1}{1+r} \left[\alpha_1\partial_x^2r + \alpha_2\partial_y^2r + 2k_1\partial_xr + 2k_2\partial_yr + 2\partial_xr\partial_x\phi + 2\partial_yr\partial_y\phi \right]. \end{aligned} \quad (2.38)$$

Upon linearizing around the base state $(r, \phi) = (0, 0)$ of the unperturbed traveling wave, (2.36) and (2.38) become

$$\partial_t r = -2R_0^2r + \partial_x^2r + \partial_y^2r - 2k_1\alpha_1\partial_xr - 2k_2\alpha_2\partial_yr - 2k_1\partial_x\phi - 2k_2\partial_y\phi - \alpha_1\partial_x^2\phi - \alpha_2\partial_y^2\phi \quad (2.39)$$

$$\partial_t\phi = -2R_0^2\beta r + \partial_x^2\phi + \partial_y^2\phi - 2k_1\alpha_1\partial_x\phi - 2k_2\alpha_2\partial_y\phi + \alpha_1\partial_x^2r + \alpha_2\partial_y^2r + 2k_1\partial_xr + 2k_2\partial_yr. \quad (2.40)$$

Using the modes $r = \hat{r}e^{\sigma t + iq \cdot x}$ and $\phi = \hat{\phi}e^{\sigma t + iq \cdot x}$ for the perturbations where the wavenumber of the perturbation is much smaller than the wavenumber of the base state, $|q| \ll |k|$, we can get the eigenvalues

$$\sigma_1 = -2R_0^2 + O(q), \quad (2.41)$$

$$\begin{aligned} \sigma_2 = & 2ik_1(\beta - \alpha_1)q_1 + 2ik_2(\beta - \alpha_2)q_2 + \left(\frac{2k_1^2}{R_0^2} + \frac{2\beta^2 k_1^2}{R_0^2} - \alpha_1\beta - 1\right)q_1^2 \\ & + \left(\frac{4k_1 k_2}{R_0^2} + \frac{4\beta^2 k_1 k_2}{R_0^2}\right)q_1 q_2 + \left(\frac{2k_2^2}{R_0^2} + \frac{2\beta^2 k_2^2}{R_0^2} - \alpha_2\beta - 1\right)q_2^2 + O(q^3). \end{aligned} \quad (2.42)$$

The first eigenvalue always has negative real part which results in the exponential decay and elimination of the amplitude perturbation. Looking at the real part of the second eigenvalue we see that it will be unstable if

$$D_x q_1^2 + D_{xy} q_1 q_2 + D_y q_2^2 > 0, \quad (2.43)$$

where

$$D_x = \left(\frac{2k_1^2(1 + \beta^2)}{\mu - (k_1^2 + k_2^2)} - (\alpha_1\beta + 1) \right), \quad (2.44a)$$

$$D_{xy} = \left(\frac{4k_1 k_2(1 + \beta^2)}{\mu - (k_1^2 + k_2^2)} \right), \quad (2.44b)$$

$$D_y = \left(\frac{2k_2^2(1 + \beta^2)}{\mu - (k_1^2 + k_2^2)} - (\alpha_2\beta + 1) \right) \quad (2.44c)$$

which are in agreement with the linear stability analysis of the isotropic CGL equation [37]. The rational parts of (2.44a) and (2.44c) are non-negative inside the μ unit circle and as required by $R_0^2 = \mu - (k_1^2 + k_2^2)$. The crossterm coefficient (2.44b) will be non-negative as long as k_1 and k_2 are not of opposite sign. Also, note that the choice of wavevector \mathbf{k} for the base stripe state must lie inside a circle with radius of the control parameter μ . This help to emphasize the validity of the linear stability as only near onset. Inequality (2.43) will then be met if $(\alpha_1 + \alpha_2)\beta + 2 < 0$, which reduces to the standard Benjamin-Feir criterion in the isotropic case when $\alpha_1 = \alpha_2$.

Expanding the eigenvalue (2.42) to fourth order in q for the long-wave base state $k_1 = k_2 = 0$ yields the linear phase equation

$$\partial_t \phi = (1 + \alpha_1\beta)\partial_x^2 \phi + (1 + \alpha_2\beta)\partial_y^2 \phi - \frac{\alpha_1^2(1 + \beta^2)}{2R_0^2}\partial_x^4 \phi - \frac{\alpha_2^2(1 + \beta^2)}{2R_0^2}\partial_y^4 \phi - \frac{\alpha_1\alpha_2(1 + \beta^2)}{R_0^2}\partial_x^2 \partial_y^2 \phi. \quad (2.45)$$

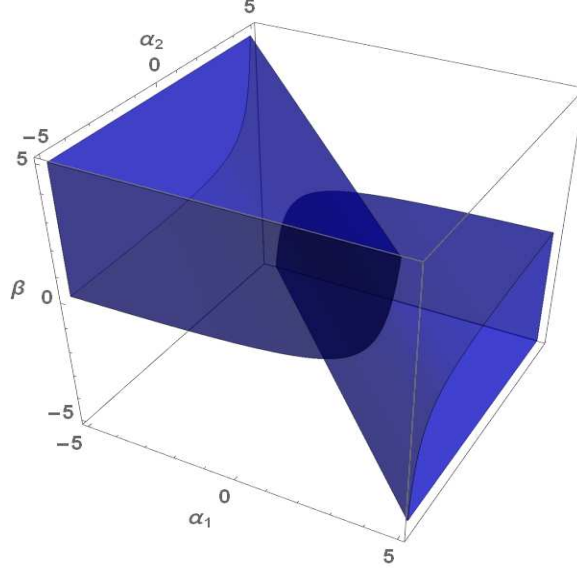


Figure 2.15: The shaded region is where $(\alpha_1 + \alpha_2)\beta + 2 < 0$.

Adding in the appropriate nonlinearity we get

$$\begin{aligned} \partial_t \phi = & (1 + \alpha_1 \beta) \partial_x^2 \phi + (1 + \alpha_2 \beta) \partial_y^2 \phi - \frac{\alpha_1^2 (1 + \beta^2)}{2R_0^2} \partial_x^4 \phi - \frac{\alpha_2^2 (1 + \beta^2)}{2R_0^2} \partial_y^4 \phi \\ & - \frac{\alpha_1 \alpha_2 (1 + \beta^2)}{R_0^2} \partial_x^2 \partial_y^2 \phi + g(k_1, k_2) (\partial_x \phi)^2 + h(k_1, k_2) (\partial_y \phi)^2 \end{aligned} \quad (2.46)$$

where the coefficients $g(k_1, k_2)$ and $h(k_1, k_2)$ for the nonlinear terms are to be solved for later. From the phase equation (2.46) we see that the Benjamin-Feir instability $\alpha\beta + 1 < 0$ manifests itself in each of the diffusion terms with different α_i values because of the anisotropy in (2.31). This demonstrates the unique possibility of the traveling wave ansatz (2.32) to be stable in one direction and unstable in the other, which is not possible in the isotropic version (2.8).

2.2.2 Weakly Nonlinear Analysis for long-wave instability

To look at the behavior of the long-wave instability for the ACGLE (2.31) we substitute $\mathbf{k} = 0$ into the traveling wave solution (2.32). This leads to the ansatz with perturbed amplitude and phase

$$A(x, y, t) = \sqrt{\mu} (1 + r(x, y, t)) e^{i(-\beta\mu t + \phi(x, y, t))}. \quad (2.47)$$

For the slow space and time scalings we use

$$r(x, y, t) = \delta^6 W(\delta x, \delta y, \delta^4 t), \quad \phi(x, y, t) = \delta^2 \Phi(\delta x, \delta y, \delta^4 t) \quad (2.48)$$

from [17]. After separating real and imaginary parts, scaling, and dividing the W and Φ equations each by δ^6 we get that

$$\begin{aligned} \delta^4 \partial_T W &= \delta^2 (\partial_X^2 W + \partial_Y^2 W) - 2\delta^4 (\alpha_1 \partial_X W \partial_X \Phi + \alpha_2 \partial_Y W \partial_Y \Phi) \\ &+ (1 + \delta^6 W) (-2\mu W - \delta^6 \mu W - (\partial_X \Phi)^2 - (\partial_Y \Phi)^2 - \delta^{-2} \alpha_1 \partial_X^2 \Phi - \delta^{-2} \alpha_2 \partial_Y^2 \Phi), \end{aligned} \quad (2.49)$$

$$\begin{aligned} \partial_T \Phi &= -2\beta \mu W - \delta^6 \beta \mu W^2 - \alpha_1 (\partial_X \Phi)^2 - \alpha_2 (\partial_Y \Phi)^2 + \delta^{-2} (\partial_X^2 \Phi + \partial_Y^2 \Phi) \\ &+ \frac{\delta^2 (\alpha_1 \partial_X^2 W + \alpha_2 \partial_Y^2 W) + 2\delta^4 (\partial_X W \partial_X \Phi + \partial_Y W \partial_Y \Phi)}{1 + \delta^6 W} \end{aligned} \quad (2.50)$$

Balancing the leading order terms in the W equation leads to

$$W = \frac{-(\alpha_1 \partial_X^2 \Phi + \alpha_2 \partial_Y^2 \Phi)}{2\delta^2 \mu} + \mathcal{O}(1). \quad (2.51)$$

Plugging this back into the full W equation (2.49) gives

$$\begin{aligned} W &= \frac{-(\alpha_1 \partial_X^4 \Phi + \alpha_2 \partial_X^2 \partial_Y^2 \Phi + \alpha_1 \partial_Y^2 \partial_X^2 \Phi + \alpha_2 \partial_Y^4 \Phi)}{4\mu^2} \\ &- \frac{(\partial_X \Phi)^2 + (\partial_Y \Phi)^2}{2\mu} - \frac{\alpha_1 \partial_X^2 \Phi + \alpha_2 \partial_Y^2 \Phi}{2\delta^2 \mu} + \mathcal{O}(\delta), \end{aligned} \quad (2.52)$$

or slightly more succinctly as

$$W = \frac{-(\alpha_1 \partial_X^4 \Phi + (\alpha_1 + \alpha_2) \partial_X^2 \partial_Y^2 \Phi + \alpha_2 \partial_Y^4 \Phi)}{4\mu^2} - \frac{(\partial_X \Phi)^2 + (\partial_Y \Phi)^2}{2\mu} - \frac{\alpha_1 \partial_X^2 \Phi + \alpha_2 \partial_Y^2 \Phi}{2\delta^2 \mu} + \mathcal{O}(\delta). \quad (2.53)$$

Equation (2.53) can be used to eliminate W from the Φ equation (2.50). Doing so yields

$$\begin{aligned}
\partial_T \Phi = & -2\beta\mu \left[\frac{-(\alpha_1 \partial_X^4 \Phi + (\alpha_1 + \alpha_2) \partial_X^2 \partial_Y^2 \Phi + \alpha_2 \partial_Y^4 \Phi)}{4\mu^2} \right. \\
& \left. - \frac{(\partial_X \Phi)^2 + (\partial_Y \Phi)^2}{2\mu} - \frac{\alpha_1 \partial_X^2 \Phi + \alpha_2 \partial_Y^2 \Phi}{2\delta^2 \mu} \right] - \frac{(\alpha_1^2 \partial_X^4 \Phi + 2\alpha_1 \alpha_2 \partial_X^2 \partial_Y^2 \Phi + \alpha_2^2 \partial_Y^4 \Phi)}{2\mu} \\
& + \delta^{-2} (\partial_X^2 \Phi + \partial_Y^2 \Phi) - \alpha_1 (\partial_X \Phi)^2 - \alpha_2 (\partial_Y \Phi)^2 + h.o.t.
\end{aligned} \tag{2.54}$$

where the fourth-order terms on the second line come from the first-order series approximation for $\frac{\delta^2 \alpha_1 \partial_X^2 W}{1 + \delta^6 W}$ and similar Y term. Cleaning up results in the phase equation

$$\begin{aligned}
\partial_T \Phi = & \frac{(1 + \alpha_1 \beta) \partial_X^2 \Phi + (1 + \alpha_2 \beta) \partial_Y^2 \Phi}{\delta^2} \\
& + \frac{(\beta \alpha_1 - \alpha_1^2) \partial_X^4 \Phi + (\beta(\alpha_1 + \alpha_2) - 2\alpha_1 \alpha_2) \partial_X^2 \partial_Y^2 \Phi + (\beta \alpha_2 - \alpha_2^2) \partial_Y^4 \Phi}{2\mu} \\
& + (\beta - \alpha_1) (\partial_X \Phi)^2 + (\beta - \alpha_2) (\partial_Y \Phi)^2.
\end{aligned} \tag{2.55}$$

We have now found the coefficients for the nonlinear terms in Equation (2.46). The linear coefficients of (2.46) and (2.55) are equal at the BFN neutral stability curve $1 + \alpha_1 \beta = 1 + \alpha_2 \beta = 0$ and match the form from our derivation of the isotropic phase equation (2.30) and from [38].

Just as in (2.46), the anisotropy allows for the possibility of a Benjamin-Feir type instability to occur the X or Y directions individually while the other is stable, or for both directions to become unstable simultaneously. This leads naturally leads to codimension one and codimension two phase equations.

The solutions of the phase equation can be compared to the solutions of the phase of solutions of the ACGLE as seen in Figures 2.16 and 2.17 which show isotropic and anisotropic phase chaos. The phase of A computed with `angle(A)` should look similar to the solution of the phase equation Φ . We can use the approximation (2.51) for $W(\Phi)$ after solving the phase equation for Φ and recreate solutions of the ACGLE by substituting $W(\Phi)$ and Φ into the ansatz (2.47).

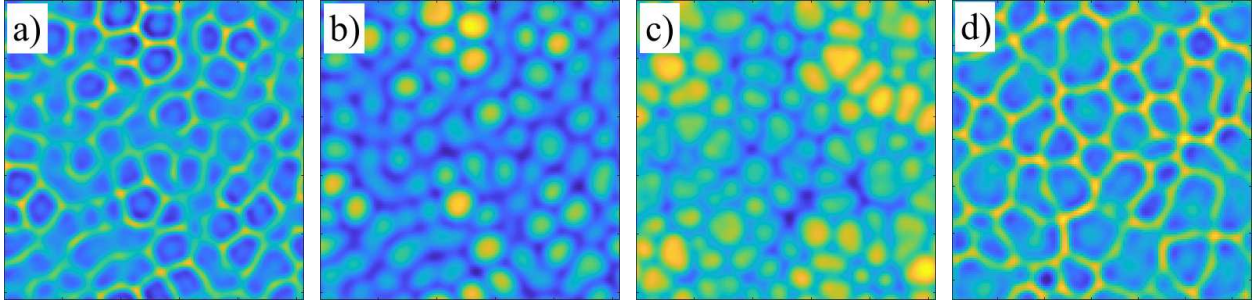


Figure 2.16: A solution to the ACGLE with parameters $\alpha_1 = \alpha_2 = -0.22$, $\beta = 5$ was simulated on a square domain $[-100, 100] \times [-100, 100]$ to time $t = 150$. (a) The absolute value of a solution to the ACGLE $|A|$ and (b) its phase $\text{angle}(A)$. (c) The solution Φ of the phase equation (2.55) using the same parameters at time $t = 50$. Φ from the phase equation displays the same behavior as the phase of the ACGLE with isotropic parameters. The phase equation solution Φ can be used to approximate a solution to the ACGLE by using $W(\Phi)$ and Φ in $A = (1 + W(\Phi))e^{i\Phi}$

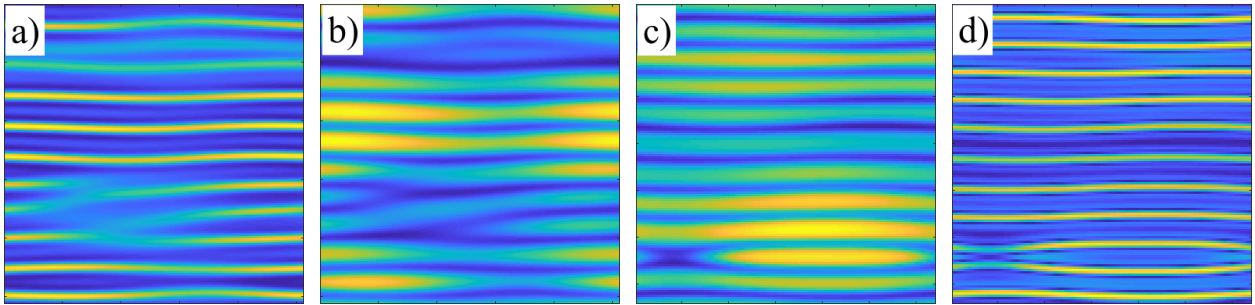


Figure 2.17: A solution to the ACGLE with parameters $\alpha_1 = 2$, $\alpha_2 = -1.2$, $\beta = 1.1$ was simulated on a square domain $[-100, 100] \times [-100, 100]$ to time $t = 600$. (a) The absolute value of a solution to the ACGLE $|A|$ and (b) its phase $\text{angle}(A)$. (c) The solution Φ of the phase equation (2.55) using the same parameters at time $t = 50$. Φ from the phase equation displays the same behavior as the phase of the ACGLE with isotropic parameters. The phase equation solution Φ can be used to approximate a solution to the ACGLE by using $W(\Phi)$ and Φ in $A = (1 + W(\Phi))e^{i\Phi}$

Codimension One Bifurcation

For the codimension one case where w.l.o.g. the y -direction is BFN-stable so that $1 + \alpha_2\beta > 0$. This gives the familiar stability region seen in Figure 2.20. If we set the second-order X coefficient equal to some arbitrary κ so that $1 + \alpha_1\beta = \kappa\delta^2$ and rescale the slow Y variable back to the fast variable as $y = \frac{Y}{\delta}$ in the full phase equation (2.55) we get the codimension one phase equation

$$\partial_T\Phi = \kappa\partial_X^2\Phi + (1 + \alpha_2\beta)\partial_y^2\Phi + \frac{(\beta\alpha_1 - \alpha_1^2)\partial_X^4\Phi}{2\mu} + (\beta - \alpha_1)(\partial_X\Phi)^2 + \mathcal{O}(\delta^2) \quad (2.56)$$

with κ as a control parameter. Limiting the bifurcation to $\kappa \ll 1$ we set $1 + \alpha_1\beta = 0$ in order to eliminate the α_1 dependence from (2.56). Removing α_1 in this manner together with ignoring higher order terms gives the final codimension one phase equation

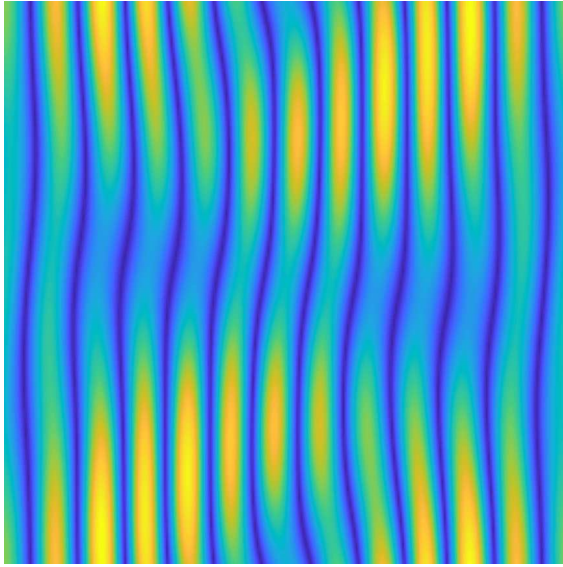
$$\partial_T\Phi = \kappa\partial_X^2\Phi + (1 + \alpha_2\beta)\partial_y^2\Phi - \frac{1}{2\mu}\left(1 + \frac{1}{\beta^2}\right)\partial_X^4\Phi + \left(\beta + \frac{1}{\beta}\right)(\partial_X\Phi)^2, \quad (2.57)$$

which retains the nonlinear dispersion parameter β and the y -direction linear dispersion parameter α_2 from the ACGLE (2.31). Again, it is required that $1 + \alpha_2\beta > 0$ so that the waves are stable in the y -direction and the diffusion coefficient stays positive so as not require any fourth-order linear or nonlinear terms to saturate the instability.

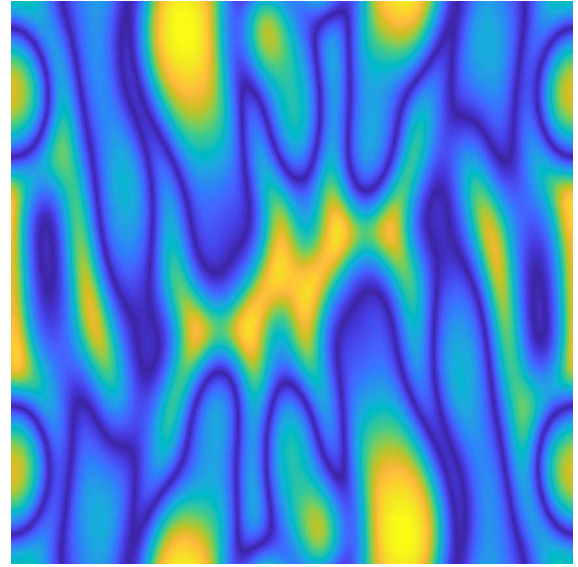
The codimension one phase equation (2.57) is similar to the equation

$$\partial_t h = -\partial_x^2 h - \partial_x^4 h + \frac{1}{2}(\partial_x h)^2 + \partial_y^2 h \quad (2.58)$$

which Rost and Krug [56] derived and described as an "elastically coupled chain" of one dimensional KS systems. They derived (2.58) to analyze the "pinching length" of the patterns produced by their version of the aKS equation which was only anisotropic in the 2nd-order derivative terms and the nonlinear terms, see Figure 2.18. They considered the case where the 4th-order spatial derivatives were isotropic.

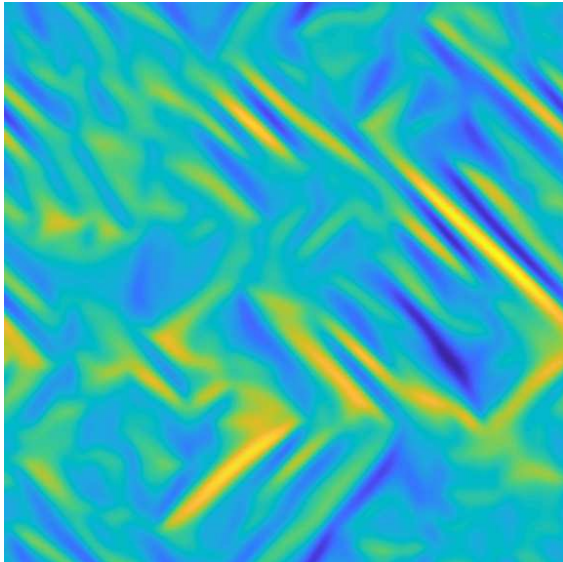


(a)

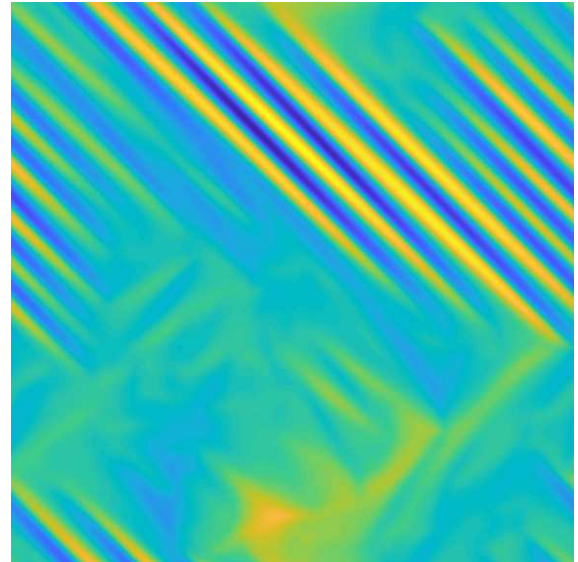


(b)

Figure 2.18: Real part of ripple solutions for the codimension one phase equation. (a) unpinched and (b) pinched.



(a) $t = 90$.



(b) $t = 120$.

Figure 2.19: Real part of cancellation mode solution of the Rost and Krug AKS equation.

However, upon using the transformations $\hat{t} = -\frac{\kappa T}{\hat{\mu}}$, $\hat{x} = \sqrt{\hat{\mu}}X$, $\hat{y} = i\sqrt{\frac{\kappa\hat{\mu}}{1+\alpha_2\beta}}y$, $\hat{\mu} = -\frac{2\kappa}{(1+\frac{1}{\beta^2})}\mu$, $\hat{\Phi} = \frac{2i^2}{\kappa}(\beta + \frac{1}{\beta})\Phi$ in Equation (2.57) gives an identical equation

$$\partial_t \Phi = -\partial_x^2 \Phi - \partial_x^4 \Phi + \frac{1}{2}(\partial_x \Phi)^2 + \partial_y^2 \Phi, \quad (2.59)$$

where all the hats from the transformations have been dropped. We choose to retain the parameters in Equation (2.57) so that its solutions may be directly compared to solutions of the CGL with the same parameters.

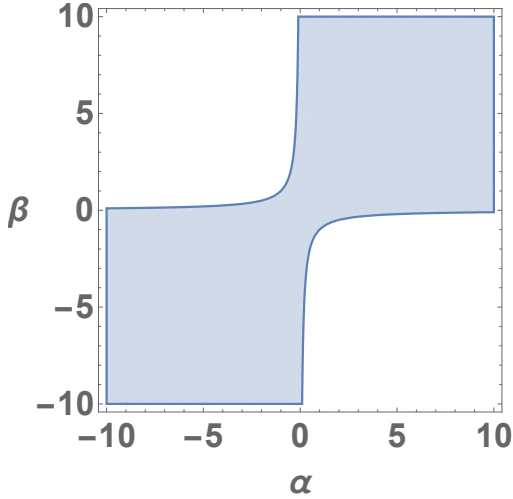


Figure 2.20: (α_2, β) parameter space for stability in the y -direction in the codimension-one bifurcation.

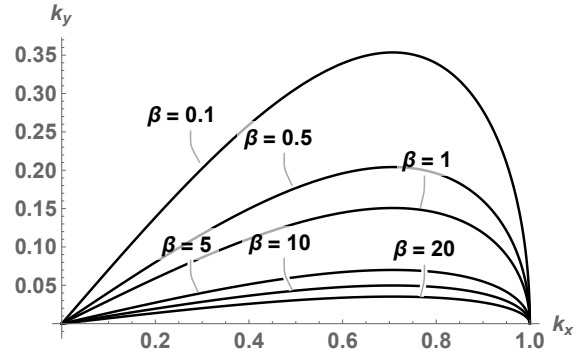


Figure 2.21: Dispersion relations of Equation (2.57) for fixed $\alpha_2 = \mu = 1$ and varying β with $\kappa = -1$ for codimension-one phase equation.

The parameter β can be kept if the scalings $\hat{t} = -\frac{\kappa T}{\hat{\mu}}$, $\hat{x} = \sqrt{\hat{\mu}}X$, $\hat{y} = \frac{i\sqrt{\kappa\hat{\mu}}}{\sqrt{1+\alpha_2\beta}}y$, $\hat{\mu} = -\kappa\mu$, $\hat{\Phi} = \frac{1}{\kappa}\Phi$ are used in Equation (2.57). The resulting phase equation, after dropping hats, is

$$\partial_t \Phi = -\partial_x^2 \Phi - \frac{1}{2} \left(1 + \frac{1}{\beta^2}\right) \partial_x^4 \Phi - \left(\beta + \frac{1}{\beta}\right) (\partial_x \Phi)^2 + \partial_y^2 \Phi. \quad (2.60)$$

We can use this form of the phase equation to explore the phase space near the Benjamin-Feir bifurcation in the ACGLE when one direction is stable and the other direction is unstable. We have

removed dependence on both the linear dispersion terms α_1 and α_2 , but have kept the dependence on the nonlinear dispersion coefficient β . Keeping the relation on β explicit allows a comparison of phase solutions back to solutions to the ACGLE. The sign on the nonlinear term is switched under the reflection transformation $\Phi \rightarrow -\Phi$.

Codimension two bifurcation

For the codimension two case we have both of the second-order derivative terms becoming unstable simultaneously. We can set $1 + \alpha_1\beta = \delta^2 r \cos(\theta)$ and $1 + \alpha_2\beta = \delta^2 r \sin(\theta)$ where $\kappa_1 = r \cos(\theta)$ and $\kappa_2 = r \sin(\theta)$ to explore the κ_1 - κ_2 parameter space numerically. For the higher-order linear and nonlinear terms we set $1 + \alpha_1\beta = 1 + \alpha_2\beta = 0$ based on begin near onset. All of this gives

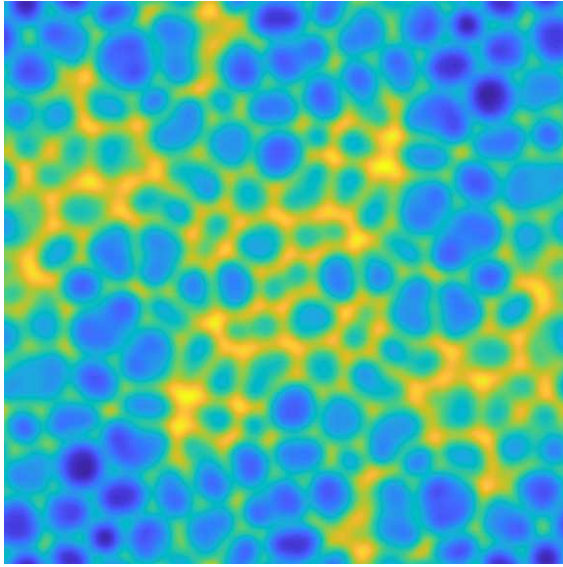
$$\partial_T \Phi = \kappa_1 \partial_X^2 \Phi + \kappa_2 \partial_Y^2 \Phi - \left(1 + \frac{1}{\beta^2}\right) \frac{\partial_X^4 \Phi + 2\partial_X^2 \partial_Y^2 \Phi + \partial_Y^4 \Phi}{2\mu} + \left(\beta + \frac{1}{\beta}\right) ((\partial_X \Phi)^2 + (\partial_Y \Phi)^2). \quad (2.61)$$

Under the assumptions leading to (2.61), cancellation modes are clearly not possible as the nonlinear terms have the same coefficient. Two examples of the codimension two phase equation are in Figure 2.22 where both θ values are in the third quadrant where both κ 's are unstable.

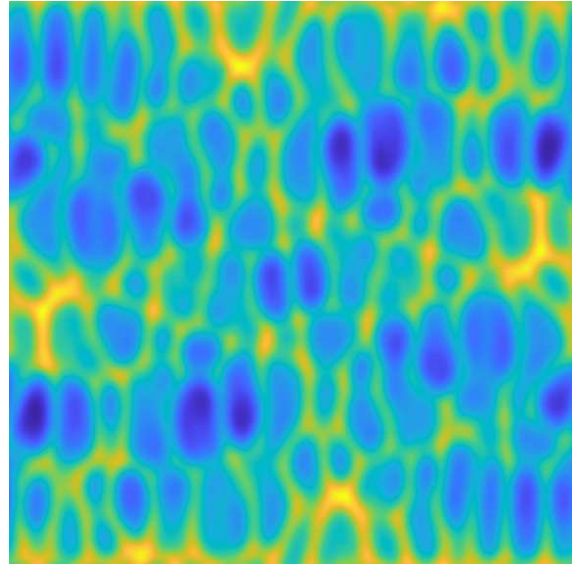
The codimension two phase equation (2.61) can also be used to recreate solutions of the CGLE. An example of this is seen in Figure 2.23. The phase of the solution A to the ACGLE and the solutions Φ of the phase equation display characteristically the same behavior. Using the lowest order approximation of W together with Φ yields a recreation of a ACGLE solution A . Using the phase equation gives considerable time savings. The ACGLE was simulated to a time of $t = 3000$ while the phase equation to only $t = 35$.

2.2.3 ACGLE Phase Diagram

Using a pseudospectral code based on [12, 30] we've numerically explored the $(\alpha_1, \alpha_2, \beta)$ parameter space to investigate the affect of anisotropy in the ACGLE (2.31). The results of the simulations show a variety of solutions similar to those in the isotropic case [11], including phase



(a) $\theta = 1.25\pi$.



(b) $\theta = 1.05\pi$.

Figure 2.22: Two solutions of the codimension two phase equation (2.61). $\text{Re}(\Phi)$ is plotted where $r = 1$ in κ_1 and κ_2 and the angle θ is given. The angle 1.25π is in the isotropic region with both control parameters equally unstable. When $\theta = 1.05\pi$, there is still instability in both directions, but barely any in the y -direction which leads to the phase chaotic cells becoming elongated along this nearly stable direction. If made stable we could see phase chaotic ripples instead of stretched cells.

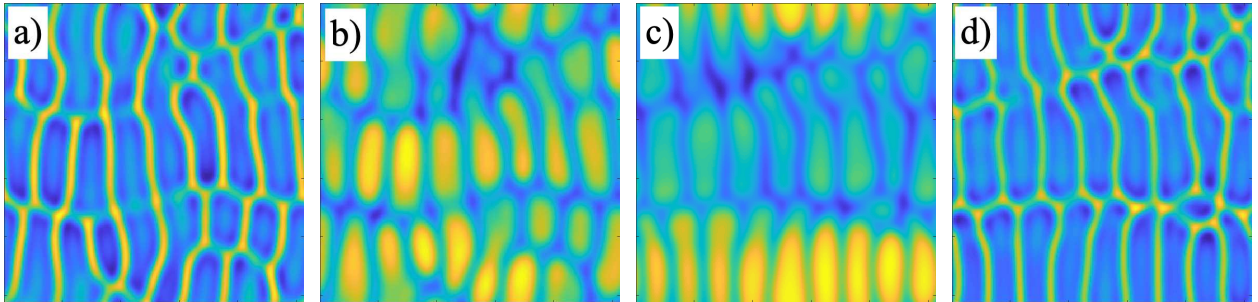


Figure 2.23: A solution to the ACGLE with parameters $\theta = 1.05\pi$ and $\beta = 2$ was simulated on a square domain $[-100, 100] \times [-100, 100]$ to time $t = 3000$. (a) The absolute value of a solution to the ACGLE $|A|$ and (b) its phase angle $\text{angle}(A)$. (c) The solution Φ of the phase equation (2.55) using the same parameters at time $t = 35$. Φ from the codim. two phase equation displays the same behavior as the phase of the ACGLE. The phase equation solution Φ can be used to approximate a solution to the ACGLE by using $W(\Phi)$ and Φ in $A = (1 + W(\Phi))e^{i\Phi}$

and defect turbulence. There are interesting intermittent transition solutions between the two types of chaos which are reminiscent of vortex glass.

The $(\alpha_1, \alpha_2, \beta)$ parameter space leads to a three-dimensional phase space for which we create a so-called phase cube. To attempt to automatically distinguish between solutions types we use the average energy (L^2 -norm) of A and ∇A which taken together give the Sobolev energy. The phase cube is displayed as α_1 - α_2 slices with constant β . The range of α_1 and α_2 is $[-3, 3]$ with a computational meshsize of 0.2, so that each slice comprises $31^2 = 961$ individual simulations. All of which have been run to a time $t = 600$. The energy images are of course symmetric about the isotropic diagonal.

Choice of Initial Condition

Something should be said about the choice of random initial conditions for the numerical simulations. An initial solution (2.32) at $t = 0$ for the longwave $\mathbf{k} = 0$ case gives $A(x, y, 0) = \sqrt{\mu}$. The ACGLE (2.31) usually has the control parameter μ scaled out so that the μA term is replaced with $\pm A$. In this case $A(x, y, 0) = 1$, and random noise around the solution $A = 1$ is a suitable numerical initial condition. However, if we leave in the μ dependence of (2.31) we see that very near onset we have $\mu \approx 0$, so noise around 0 is then an appropriate initial condition.

An IC of a perturbed $A = 0$ solution can mean that we are near the $\mu = 0$ neutral stability boundary, as just mentioned. But, having $\mathbf{k} = 0$ and $\mu = 0$ is not the only way to have $R_0^2 = 0$ in condition (2.32b). This will also happen for wavevectors that approach the circle of radius μ in k_x - k_y wavevector space.

The choice of which random IC is important, not only for its interpretation, but because each one also gives different solution types. As we see from our simulations, the cellular frozen state solutions are seen only when the noise-around-zero initial condition is chosen, and phase chaos only when the noise-around-one condition is chosen.

Simulation Results

The average energies for A and ∇A for both the noise-around-one, and noise-around-zero initial conditions are shown in Figures 2.24, 2.25, 2.26, and 2.27. The two initial conditions result in a different average energy patterns. The noise-around-one case requires β to be sufficiently far from zero for the energies to vary significantly. As $|\beta|$ is increased, there is a high-energy plateau in the shape of a square which is nearly, but not exactly, bounded by the lines $\alpha_1 = -1/\beta$ and $\alpha_2 = -1/\beta$ which are the coefficients of linear stability (2.44) for the longwave case. The noise-around-zero case has high energy variability across all β values. At $\beta = 0$ there is a hyperbolic high-energy plateau and two low-energy valleys. As $|\beta|$ increases, the high-energy region shifts towards a single corner.

The average energies of ∇A are not significant compared to those for A and thus do not heavily contribute to the combined Sobolev energy. Further, there does not appear to be much information gained from looking at the ∇A energy, except in small areas for the noise-around-zero case along the slope of the high-energy plateau. which are not visible in looking at the A energies. Perhaps also in the noise-around-one case right next to the square-shaped, high-energy plateau. This is most visible in the lower right $\beta = 3$ cases.

A closer look at how the energy relates to solutions is seen in Figures 2.28 and 2.29. In these figures, parameters are varied along the isotropic diagonal and along an α_2 line for fixed α_1 . The noise-around-one initial condition sees phase and defect chaos solutions of both their isotropic and anisotropic varieties. The noise-around-zero initial condition sees the frozen cellular state transition into isolated vortices as the shock walls vanish along the isotropic diagonal. It also sees solutions where both spiral defects and phase chaos coexist, a behavior not seen in the isotropic CGLE. In these solutions phase chaotic ripples are aligned along the BFN stable direction. The stability in this direction inhibits the formation of the cellular shock structure and the spiral defects are convective in nature. As the spirals convect around oppositely rotating spirals interact and annihilate leaving only anisotropic phase chaos. This is demonstrated in Figure 2.30.

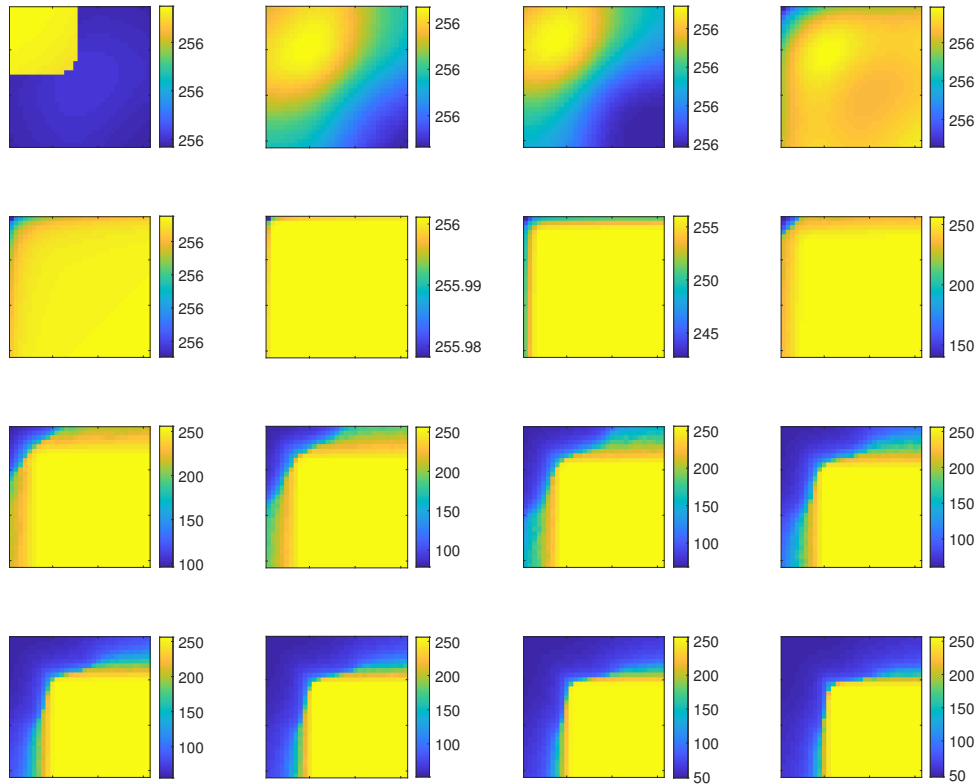


Figure 2.24: The average energy of A using the noise-around-one initial condition. The top left has $\beta = 0$ and the bottom right has $\beta = 3$. For the first 6 values of β the average energy is near constant, while structure emerges as β is increased further.

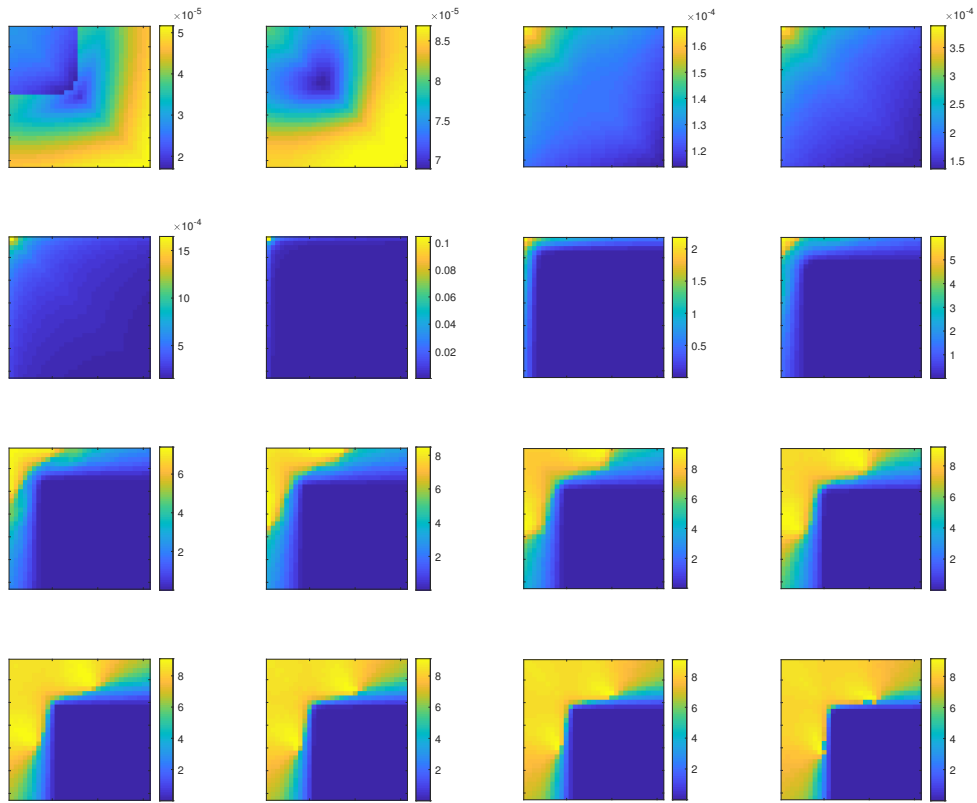


Figure 2.25: The average energy of ∇A using the noise-around-one initial condition. The top left has $\beta = 0$ and the bottom right has $\beta = 3$. The average energy of the gradient does not give much more information than looking at the average energy of A , but there do appear some small regions where both directions are BFN unstable that stand out in the ∇A measurements compared with the A measurements.

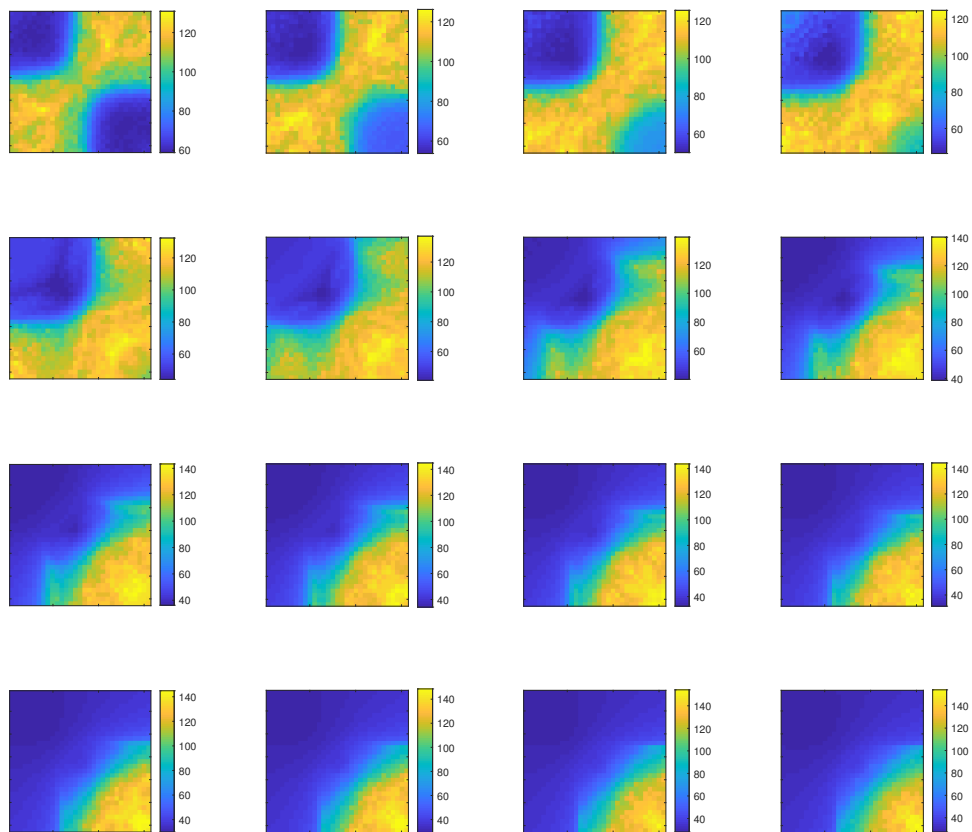


Figure 2.26: The average energy of A using the noise-around-one initial condition. The top left has $\beta = 0$ and the bottom right has $\beta = 3$. The structure of the average energy values is very different here compared to the values from the noise-around-one initial condition.

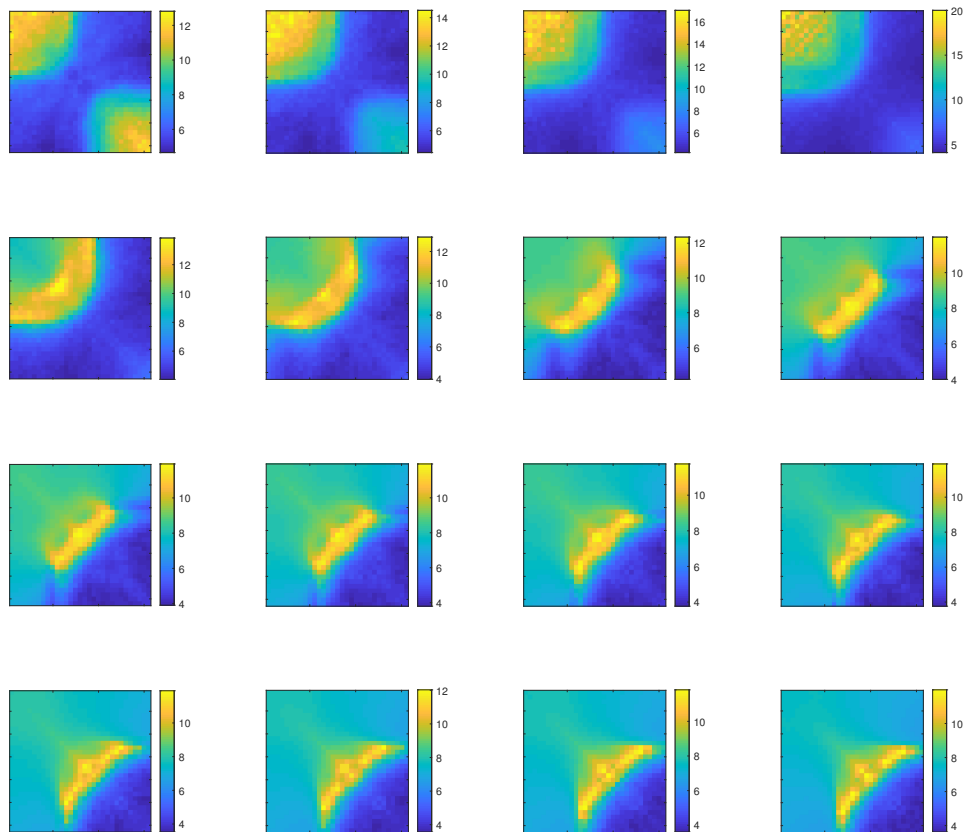


Figure 2.27: The average energy of ∇A using the noise-around-one initial condition. The top left has $\beta = 0$ and the bottom right has $\beta = 3$. The average energy measurements for ∇A are similar to those for A but have values that stand out on the slope of the high-energy plateau of A .

Verification of the longwave stability boundary with noise-around-one initial conditions is done in Figure 2.31. The neutral stability lines $\alpha_i = -1/\beta$ are plotted in red and divided the space into four quadrants. The top-left quadrant is doubly BFN unstable, the top-right and bottom-left quadrants have one stable direction and one unstable direction. The bottom-right quadrant is doubly BFN stable. Simulations were performed for the marked parameters just outside and just inside the boundary. The solution with parameters that correspond to a stable x -direction and unstable y -direction yield phase chaos. The solution with both stable parameters gives a constant solution. The variance of color is due to the narrow color axis. The energies against the number of simulated timesteps is also shown. The phase chaos solution loses energy as the chaotic behavior develops.

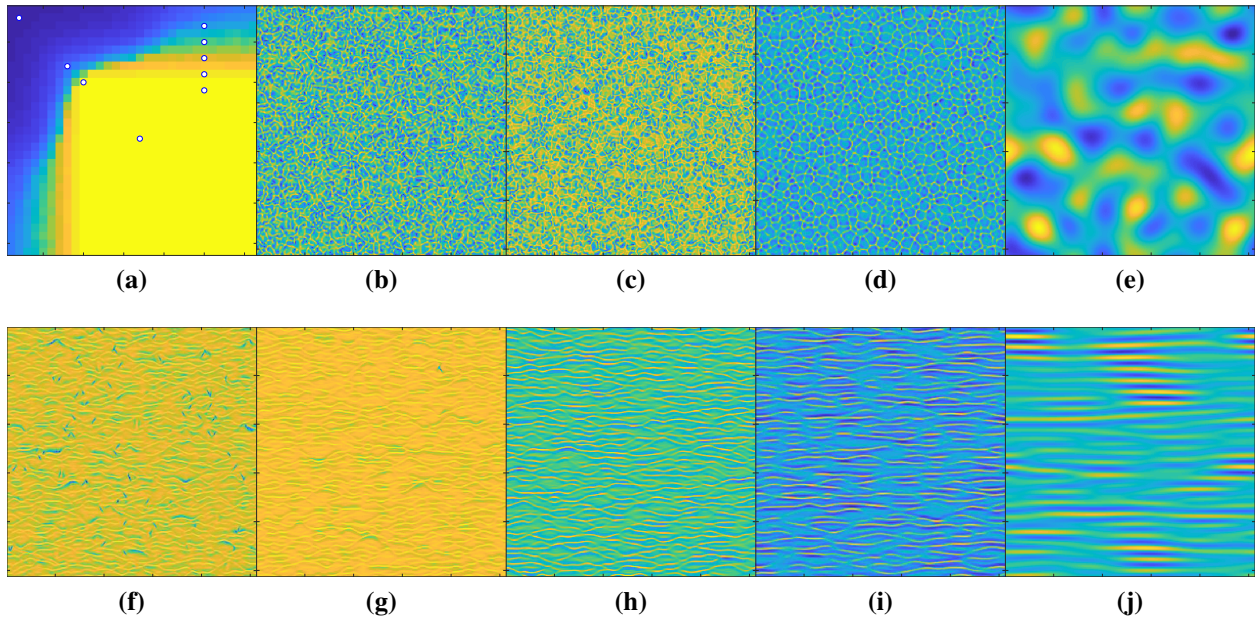


Figure 2.28: Solutions for the $\beta = 1.1$ slice of the phase cube with noise-around-one initial conditions. The average energy is shown in (a) along with markings for the locations for the parameter values used to create the other solutions. The rest of the first row (b-e) corresponds to the dots along the isotropic diagonal starting from the top left. We see that deep into the unstable upper-left corner, solutions are phase chaotic. Near the stability boundary, we observe phase chaos. In (e) waves are stable and the solution is constant. The color axis on (e) is very small. The bottom row of solutions (f-j) correspond to the markings in anisotropic parameter space for a fixed, stable α_1 value. The topmost marking furthest from the stability boundary corresponds to the solution in (f). The same defect chaos to phase chaos change in solutions is seen, but now since α_1 leads to stability in the x -direction we see characteristically anisotropic behavior. The decrease in pattern wavelength between (i) and (j) is due to crossing the stability boundary.

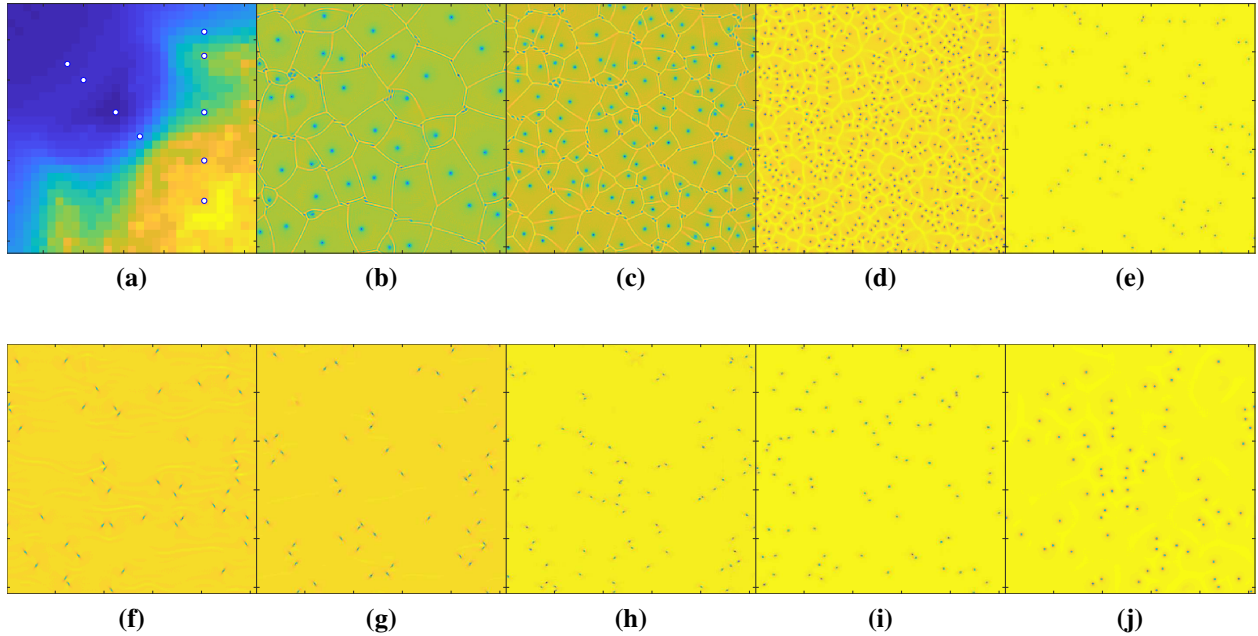


Figure 2.29: Solutions for the $\beta = 0.6$ slice of the phase cube with noise-around-zero initial conditions. The average energy is shown in (a) along with markings denoting the parameters used for the solutions (b-j). The rest of the first row (b-e) are the first four solutions along the isotropic axis. The second row (f-j) are the vertical solutions with constant α_1 and are anisotropic. The first row sees the stable frozen states of spiral defects bounded by shock walls transition into convecting spiral defects with no walls. The bottom row shows the effect of the anisotropy on the angle of the spiral cores. It also shows, for example in (f) that phase chaos along the stable direction coexists with the spiral defects. The phase chaos is difficult to make out at this colorscale, but looks like Figure 2.28(i).

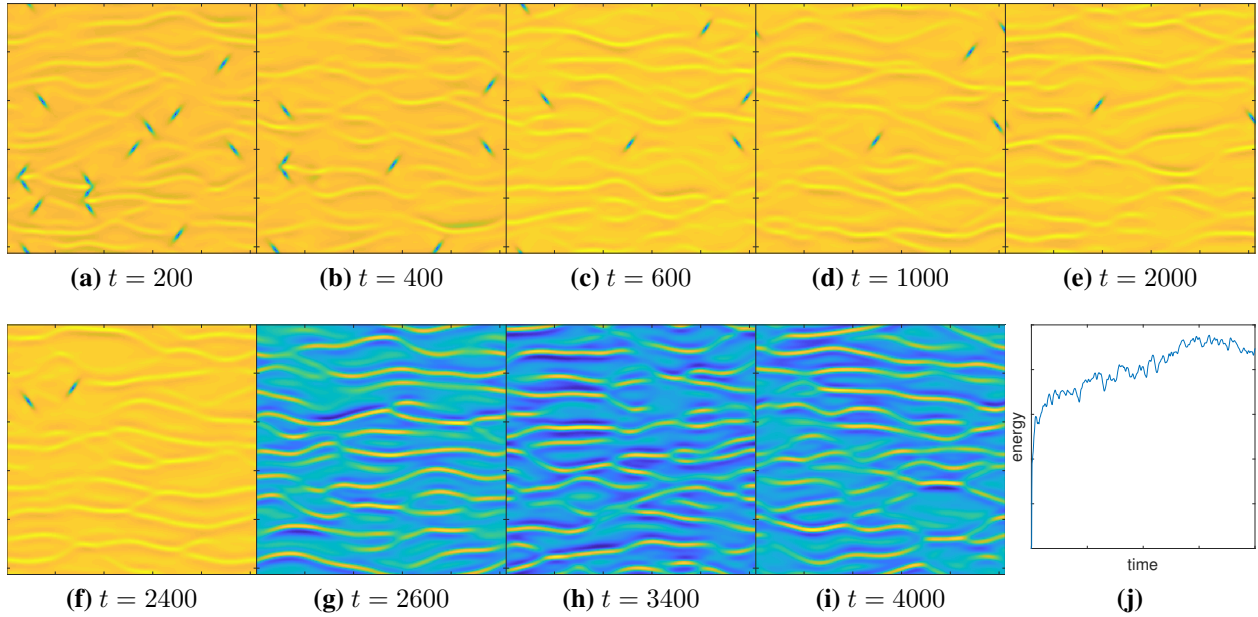


Figure 2.30: Time series of a solution for parameters similar to Figure 2.29(f) for significantly longer simulation time. Spiral defects convect and annihilate leaving only phase chaos. Average energy vs. time is shown in (j).

2.3 Summary and Conclusions

In this chapter we examined the effects of anisotropy on the complex Ginzburg-Landau equation. The addition of anisotropy allows for the study of oscillatory bifurcations in nonhomogeneous medium. We performed a linear stability analysis and derived dynamic equations for amplitude and phase perturbations of a traveling wave solution. The amplitude perturbations decay exponentially and are slaved to the phase. The phase equation solution Φ can then be used to reconstruct the amplitude perturbation $W(\Phi)$ and thus solutions of the ACGLE. One benefit of this lies in the extra slow time scaling used to derive Φ . The slow time $T = \delta^4 t$ allows for the very long time behavior of traveling wave solutions of the ACGLE to be studied much faster via the phase dynamics.

The anisotropy leads to 4 stability quadrants: (I) doubly stable; (II) stable-unstable; (III) unstable-stable; and (IV) double unstable. The behavior of these quadrants is determined with the full phase equation and solutions can be directly compared to ACGLE solutions due to retaining the linear and nonlinear dispersion coefficients α_1 , α_2 , and β . The general behavior of solutions in the I \rightarrow II or I \rightarrow III transitions can be studied via the codimension one phase equation.

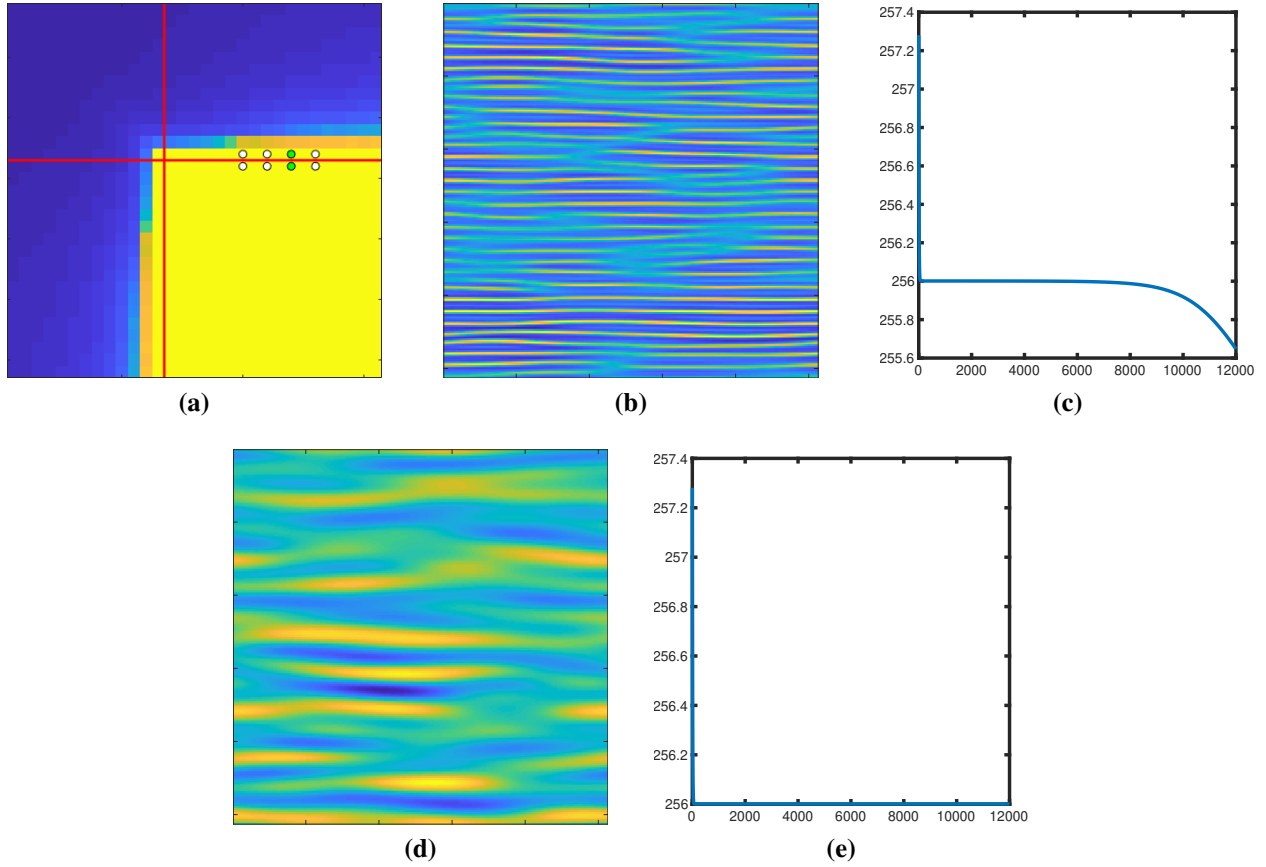


Figure 2.31: Verification of the stability boundary for the noise-around-one initial condition with $\beta = 2$. The stability boundaries $\alpha_i = -1/\beta$ are showing in red in (a). The phase chaos solution (b) corresponds to the green dot just outside (above) the doubly stable region. Its energy is plotted against computation timesteps in (c). Just inside the doubly stable region produces the solution (d) with energy (e). This stable solution quickly approaches, and stays at a constant energy and the magnitude is essentially constant, although the anisotropy is apparent at this narrow colorscale.

The codimension two equation allows for study of the I→IV transition. The codimension one and two phase equations have the unstable linear dispersion α_i scaled out and replaced with a new control parameter κ . Analysis of the three forms of the phase equation demonstrates that cancellation modes, where the nonlinearities in each direction cancel, are not possible.

The 3-dimensional phase diagram was made for parameter values near 0. The phase diagram for the ACGLE reveals that choice of random initial condition is important and determines the behavior of solutions. The the longwave, noise-around-one initial condition, phase and defect chaos occur. These chaotic states are affect by the anisotropies by forming phase ripples along the stable direction. For the noise-around-zero initial condition, frozen states of spiral defects transition into phase chaos due to the anisotropy. Stability in both directions leads to the breakdown of the shockwall boundaries and spiral-spiral annihilation with an asymptotically constant solution. The shock wall breaks down if only one direction is stable and the asymptotic states is instead phase chaos.

Verification of the linear stability boundary was tested and verified numerically. The stability boundary can roughly be determined from the average energy of solutions. Generally, regions where A has low energy are unstable in at least one direction, and the doubly stable region consists of a high-energy plateau. The sides of this plateau encroach into the unstable regions leading to a small area of high energy in the areas with at least one unstable direction.

Bibliography

- [1] I. S. ARANSON AND L. KRAMER, *The world of the complex ginzburg-landau equation*, Reviews of Modern Physics, 74 (2002), p. 99.
- [2] N. BAJCINCA, S. HOFMANN, D. BIELIEVTSOV, AND K. SUNDMACHER, *Approximate ode models for population balance systems*, Computers & Chemical Engineering, 74 (2015), pp. 158–168.
- [3] J. M. BALL, J. CARR, AND O. PENROSE, *The becker-döring cluster equations: basic properties and asymptotic behaviour of solutions*, Communications in mathematical physics, 104 (1986), pp. 657–692.
- [4] R. BECKER AND W. DÖRING, *Kinetische behandlung der keimbildung in übersättigten dämpfen*, Annalen der Physik, 416 (1935), pp. 719–752.
- [5] T. BOHR AND E. HUBER, GREG AND OTT, *The structure of spiral domain patterns*, EPL (Europhysics Letters), 33 (1996), p. 589.
- [6] T. BOHR, G. HUBER, AND E. OTT, *The structure of spiral-domain patterns and shocks in the 2d complex ginzburg-landau equation*, Physica D: Nonlinear Phenomena, 106 (1997), pp. 95–112.
- [7] R. BROWN, A. FABRIKANT, AND M. RABINOVICH, *Evolution of patterns in the anisotropic complex ginzburg-landau equation: Modulational instability*, Physical Review E, 47 (1993), p. 4141.
- [8] L. BRUSCH, A. TORCINI, M. VAN HECKE, M. G. ZIMMERMANN, AND M. BÄR, *Modulated amplitude waves and defect formation in the one-dimensional complex ginzburg-landau equation*, Physica D: Nonlinear Phenomena, 160 (2001), pp. 127–148.

- [9] L. BRUSCH, M. G. ZIMMERMANN, M. VAN HECKE, M. BÄR, AND A. TORCINI, *Modulated amplitude waves and the transition from phase to defect chaos*, Physical review letters, 85 (2000), p. 86.
- [10] S. CHANDRASEKHAR, *Stochastic problems in physics and astronomy*, Reviews of modern physics, 15 (1943), p. 1.
- [11] H. CHATÉ AND P. MANNEVILLE, *Phase diagram of the two-dimensional complex ginzburg-landau equation*, Physica A: Statistical Mechanics and its Applications, 224 (1996), pp. 348–368.
- [12] S. M. COX AND P. C. MATTHEWS, *Exponential time differencing for stiff systems*, Journal of Computational Physics, 176 (2002), pp. 430–455.
- [13] M. CROSS AND H. GREENSIDE, *Pattern formation and dynamics in nonequilibrium systems*, Cambridge University Press, 2009.
- [14] M. C. CROSS AND P. C. HOHENBERG, *Pattern formation outside of equilibrium*, Reviews of modern physics, 65 (1993), p. 851.
- [15] G. DANGELMAYR AND I. OPREA, *Modulational stability of travelling waves in 2d anisotropic systems*, Journal of Nonlinear Science, 18 (2008), pp. 1–56.
- [16] T. M. DAVIS, T. O. DREWS, H. RAMANAN, C. HE, J. DONG, H. SCHNABLEGGER, M. A. KATSOULAKIS, E. KOKKOLI, A. V. MCCORMICK, R. L. PENN, ET AL., *Mechanistic principles of nanoparticle evolution to zeolite crystals*, Nature materials, 5 (2006), p. 400.
- [17] A. DOELMAN, B. SANDSTEDTE, A. SCHEEL, AND G. SCHNEIDER, *The dynamics of modulated wave trains*, Mem. Amer. Math. Soc., 199 (2009).
- [18] T. O. DREWS, M. A. KATSOULAKIS, AND M. TSAPATSI, *A mathematical model for crystal growth by aggregation of precursor metastable nanoparticles*, The Journal of Physical Chemistry B, 109 (2005), pp. 23879–23887.

- [19] R. FALLER AND L. KRAMER, *Phase chaos in the anisotropic complex ginzburg-landau equation*, Physical Review E, 57 (1998), p. R6249.
- [20] A. FALOLA, A. BORISSOVA, AND X. Z. WANG, *Extended method of moment for general population balance models including size dependent growth rate, aggregation and breakage kernels*, Computers & Chemical Engineering, 56 (2013), pp. 1–11.
- [21] R. J. FIELD AND R. M. NOYES, *Oscillations in chemical systems. 18. mechanisms of chemical oscillators: Conceptual bases*, Accounts of Chemical Research, 10 (1977), pp. 214–221.
- [22] F. GELBARD AND J. H. SEINFELD, *The general dynamic equation for aerosols. theory and application to aerosol formation and growth*, Journal of Colloid and Interface Science, 68 (1979), pp. 363–382.
- [23] T. HAAS, B. DE RIJK, AND G. SCHNEIDER, *Modulation equations near the eckhaus boundary: the kdv equation*, arXiv preprint arXiv:1808.06912, (2018).
- [24] D. R. HANDWERK, P. D. SHIPMAN, C. B. WHITEHEAD, S. ÖZKAR, AND R. G. FINKE, *Mechanism-enabled population balance modeling of particle formation en route to particle average size and size distribution understanding and control*, Journal of the American Chemical Society, (2019).
- [25] ———, *Particle size distributions via mechanism-enabled population balance modeling*, (2019).
- [26] S. T. HE, Y. L. LIU, AND H. MAEDA, *Controlled synthesis of colloidal silver nanoparticles in capillary micro-flow reactor*, Journal of Nanoparticle Research, 10 (2008), pp. 209–215.
- [27] P. HOHENBERG AND A. KREKHOV, *An introduction to the ginzburg–landau theory of phase transitions and nonequilibrium patterns*, Physics Reports, 572 (2015), pp. 1–42.
- [28] R. B. HOYLE, *Pattern formation*, Cambridge University Press, Cambridge, 2006. An introduction to methods.

- [29] H. M. HULBURT AND S. KATZ, *Some problems in particle technology: A statistical mechanical formulation*, Chemical Engineering Science, 19 (1964), pp. 555–574.
- [30] A.-K. KASSAM AND L. N. TREFETHEN, *Fourth-order time-stepping for stiff pdes*, SIAM Journal on Scientific Computing, 26 (2005), pp. 1214–1233.
- [31] P. D. KENT, J. E. MONDLOCH, AND R. G. FINKE, *A four-step mechanism for the formation of supported-nanoparticle heterogenous catalysts in contact with solution: The conversion of $ir(1, 5\text{-cod})\text{-}cl/\gamma\text{-}al_2o_3$ to $ir(0) 170/\gamma\text{-}al_2o_3$* , Journal of the American Chemical Society, 136 (2014), pp. 1930–1941.
- [32] Y. KURAMOTO, *Phase dynamics of weakly unstable periodic structures*, Progress of theoretical physics, 71 (1984), pp. 1182–1196.
- [33] ———, *Chemical oscillations, waves, and turbulence*, Courier Corporation, 2003.
- [34] Y. KURAMOTO AND T. TSUZUKI, *Persistent propagation of concentration waves in dissipative media far from thermal equilibrium*, Progress of theoretical physics, 55 (1976), pp. 356–369.
- [35] V. K. LAMER AND R. H. DINEGAR, *Theory, production and mechanism of formation of monodispersed hydrosols*, Journal of the American Chemical Society, 72 (1950), pp. 4847–4854.
- [36] Y. LAN, N. GARNIER, AND P. CVITANOVIĆ, *Stationary modulated-amplitude waves in the 1d complex ginzburg–landau equation*, Physica D: Nonlinear Phenomena, 188 (2004), pp. 193–212.
- [37] J. LEGA, *Traveling hole solutions of the complex ginzburg–landau equation: a review*, Physica D: Nonlinear Phenomena, 152 (2001), pp. 269–287.
- [38] ———, *Phase diffusion and weak turbulence*, in Dynamics and Bifurcation of Patterns in Dissipative Systems, World Scientific, 2004, pp. 143–157.

- [39] R. J. LEVEQUE, *Finite volume methods for hyperbolic problems*, vol. 31, Cambridge university press, 2002.
- [40] Y. LIAO, R. OERTEL, S. KRIEBITZSCH, F. SCHLEGEL, AND D. LUCAS, *A discrete population balance equation for binary breakage*, *International Journal for Numerical Methods in Fluids*, 87 (2018), pp. 202–215.
- [41] Y. LIN AND R. G. FINKE, *A more general approach to distinguishing "homogeneous" from "heterogeneous" catalysis: Discovery of polyoxoanion- and Bu_4N^+ -stabilized, isolable and redissolvable, high-reactivity ir. apprx. 190-450 nanocluster catalysts*, *Inorganic Chemistry*, 33 (1994), pp. 4891–4910.
- [42] —, *Novel polyoxoanion- and $\{Bu_4N^+\}$ -stabilized, isolable, and redissolvable, 20-30-ang. Ir³⁰⁰⁻⁹⁰⁰ nanoclusters: The kinetically controlled synthesis, characterization, and mechanism of formation of organic solvent-soluble, reproducible size, and reproducible catalytic activity metal nanoclusters*, *Journal of the American Chemical Society*, 116 (1994), pp. 8335–8353.
- [43] I. MELBOURNE AND G. SCHNEIDER, *Phase dynamics in the real ginzburg-landau equation*, *Mathematische Nachrichten*, 263 (2004), pp. 171–180.
- [44] G. MENON AND R. L. PEGO, *Approach to self-similarity in smoluchowski's coagulation equations*, *Communications on Pure and Applied Mathematics: A Journal Issued by the Courant Institute of Mathematical Sciences*, 57 (2004), pp. 1197–1232.
- [45] —, *Dynamical scaling in smoluchowski's coagulation equations: uniform convergence*, *SIAM review*, 48 (2006), pp. 745–768.
- [46] J. MURRAY, *Mathematical Biology*, Springer-Verlag New York, 2002.
- [47] A. C. NEWELL AND J. A. WHITEHEAD, *Finite bandwidth, finite amplitude convection*, *Journal of Fluid Mechanics*, 38 (1969), pp. 279–303.

- [48] R. M. NOYES AND R. J. FIELD, *Oscillations in chemical systems. 19. mechanisms of chemical oscillators: experimental examples*, Accounts of Chemical Research, 10 (1977), pp. 273–280.
- [49] S. ÖZKAR AND R. G. FINKE, *Nanoparticle nucleation is termolecular in metal and involves hydrogen: Evidence for a kinetically effective nucleus of three $\{Ir_3H_{2x} \cdot P_2W_{15}Nb_3O_{62}\}^{6-}$ in $Ir(0)_n$ nanoparticle formation from $[(1, 5 - COD)Ir^I \cdot P_2W_{15}Nb_3O_{62}]^{8-}$ plus dihydrogen*, Journal of the American Chemical Society, 139 (2017), pp. 5444–5457.
- [50] S. R. K. PERALA AND S. KUMAR, *On the two-step mechanism for synthesis of transition-metal nanoparticles*, Langmuir, 30 (2014), pp. 12703–12711.
- [51] J. POLTE, *Fundamental growth principles of colloidal metal nanoparticles—a new perspective*, CrystEngComm, 17 (2015), pp. 6809–6830.
- [52] D. RAMKRISHNA, *Population balances: Theory and applications to particulate systems in engineering*, Elsevier, 2000.
- [53] D. RAMKRISHNA AND A. W. MAHONEY, *Population balance modeling. promise for the future*, Chemical Engineering Science, 57 (2002), pp. 595–606.
- [54] D. RAMKRISHNA AND M. R. SINGH, *Population balance modeling: current status and future prospects*, Annual Review of Chemical and Biomolecular Engineering, 5 (2014), pp. 123–146.
- [55] A. RANDOLPH, *A population balance for countable entities*, The canadian journal of chemical engineering, 42 (1964), pp. 280–281.
- [56] M. ROST AND J. KRUG, *Anisotropic kuramoto-sivashinsky equation for surface growth and erosion*, Physical review letters, 75 (1995), p. 3894.

- [57] A. SCHMIDT AND V. SMIRNOV, *Concept of “magic” number clusters as a new approach to the interpretation of unusual kinetics of the heck reaction with aryl bromides*, Topics in catalysis, 32 (2005), pp. 71–75.
- [58] L. A. SEGEL, *Distant side-walls cause slow amplitude modulation of cellular convection*, Journal of Fluid Mechanics, 38 (1969), pp. 203–224.
- [59] J. A. SHERRATT, M. J. SMITH, AND J. D. RADEMACHER, *Patterns of sources and sinks in the complex ginzburg–landau equation with zero linear dispersion*, SIAM Journal on Applied Dynamical Systems, 9 (2010), pp. 883–918.
- [60] G. SIVASHINSKY, *Nonlinear analysis of hydrodynamic instability in laminar flames-I. derivation of basic equations*, Acta Astronautica, 4 (1977), pp. 1177–1206.
- [61] M. V. SMOLUCHOWSKI, *Versuch einer mathematischen theorie der koagulationskinetik kolloider lösungen*, Zeitschrift für physikalische Chemie, 92 (1918), pp. 129–168.
- [62] J. SOLSVIK AND H. A. JAKOBSEN, *The foundation of the population balance equation: a review*, Journal of Dispersion Science and Technology, 36 (2015), pp. 510–520.
- [63] F. SPORLEDER, Z. BORKA, J. SOLSVIK, AND H. A. JAKOBSEN, *On the population balance equation*, Reviews in Chemical Engineering, (2012).
- [64] T. SUGIMOTO, *The theory of the nucleation of monodisperse particles in open systems and its application to agbr systems*, Journal of colloid and interface science, 150 (1992), pp. 208–225.
- [65] R. SZABÓ AND G. LENTE, *Full analytical solution of a nucleation-growth type kinetic model of nanoparticle formation*, Journal of Mathematical Chemistry, (2018), pp. 1–16.
- [66] N. T. THANH, N. MACLEAN, AND S. MAHIDDINE, *Mechanisms of nucleation and growth of nanoparticles in solution*, Chemical reviews, 114 (2014), pp. 7610–7630.

- [67] G. VAN BAALEN, *Phase turbulence in the complex ginzburg-landau equation via kuramoto–sivashinsky phase dynamics*, Communications in mathematical physics, 247 (2004), pp. 613–654.
- [68] M. VAN HECKE, *Building blocks of spatiotemporal intermittency*, Physical review letters, 80 (1998), p. 1896.
- [69] W. VAN SAARLOOS AND P. HOHENBERG, *Fronts, pulses, sources and sinks in generalized complex ginzburg-landau equations*, Physica D: Nonlinear Phenomena, 56 (1992), pp. 303–367.
- [70] J. A. WATTIS, *An introduction to mathematical models of coagulation–fragmentation processes: a discrete deterministic mean-field approach*, Physica D: Nonlinear Phenomena, 222 (2006), pp. 1–20.
- [71] M. A. WATZKY AND R. G. FINKE, *Transition metal nanocluster formation kinetic and mechanistic studies. a new mechanism when hydrogen is the reductant: slow, continuous nucleation and fast autocatalytic surface growth*, Journal of the American Chemical Society, 119 (1997), pp. 10382–10400.
- [72] W. H. WHITE, *A global existence theorem for smoluchowski’s coagulation equations*, Proceedings of the American Mathematical Society, (1980), pp. 273–276.
- [73] C. B. WHITEHEAD, S. ÖZKAR, AND R. G. FINKE, *Lamer’s 1950 model for particle formation of instantaneous nucleation and diffusion-controlled growth: A historical look at the model’s origins, assumptions, equations, and underlying sulfur sol formation kinetics data*, Chemistry of Materials, (2019).
- [74] T.-H. YANG, S. ZHOU, K. D. GILROY, L. FIGUEROA-COSME, Y.-H. LEE, J.-M. WU, AND Y. XIA, *Autocatalytic surface reduction and its role in controlling seed-mediated growth of colloidal metal nanocrystals*, Proceedings of the National Academy of Sciences, 114 (2017), pp. 13619–13624.

- [75] X. YIN, M. SHI, J. WU, Y.-T. PAN, D. L. GRAY, J. A. BERTKE, AND H. YANG, *Quantitative analysis of different formation modes of platinum nanocrystals controlled by ligand chemistry*, Nano letters, 17 (2017), pp. 6146–6150.